國 立 交 通 大 學

電子工程學系電子研究所

碩 士 論 文

具有適當密度與元件結構之奈米碳管之場發射特性最佳化

Optimization for the Field Emission Properties of

Carbon Nanotubes with Proper Densities and

Device Structures

研 究 生：許 鈞 凱

指導教授：鄭 晃 忠 博士

中華民國 九十五 年 七 月

具有適當密度與元件結構之奈米碳管之場發射特性最佳化

Optimization for the Field Emission Properties of Carbon Nanotubes with Proper Densities and Device Structures

研 究 生：許鈞凱   Student: Jiun-Kai Shiu

指導教授：鄭晃忠 博士   Advisor: Dr. Huang-Chung Cheng

國 立 交 通 大 學

電子工程學系　　電子研究所碩士班

碩士論文

A Thesis
Submitted to Department of Electronics Engineering & Institute of Electronics
College of Electrical and Computer Engineering
National Chiao Tung University
In Partial Fulfillment of the Requirements
for the Degree of Master
in
Electronics Engineering
2006
Hsinchu, Taiwan, Republic of China

中華民國 九十五年七月

具有適當密度與元件結構之奈米碳管之場發射特性最佳化

研究生：許鈞凱　　　　　指導教授：鄭晃忠 博士

國立交通大學電子工程學系　　電子研究所碩士班

摘　要

利用熱化學氣相沉積系統成長出來的奈米碳管的密度依舊太高而導致因遮蔽效應而造成場發射電流密度下降和起始電場上升。在此論文中，我們提出了三種新穎的密度控制方法去控制奈米碳管的密度進而改善場發射特性，其中包括了兩種薄的鈦覆蓋層的製程和一個鐵和鈦共鍍的製程。對於沒有前處理而蓋薄的鈦覆蓋層的方法，其場發射特性不好。對於前處理完後蓋薄的鈦覆蓋層的方法，當奈米碳管的密度由 2.8×10^8 cm^{-2}下降到 2.8×10^7 cm^{-2}時，在 6 V/μm 的電場下其場發射電流密度從 11.12 mA/cm^{2}增加到 97.6 mA/cm^2，起始電場從 3.786 V/μm下降到 2.5 V/μm。然而，從發光的圖像來看，其均勻度依舊沒有被改善。對於鐵和鈦共鍍的方法，由於在濺鍍的過程中鐵和鈦的原子是均勻分佈在其中，所以可以得到一個比較均勻的催化金屬膜。由此可知，共鍍的技巧將會改善奈米碳管的均勻度並期待在未來大尺寸且高解析度奈米碳管場發射顯示器的誕生。除此之外，我們提出了兩種機制來解釋這

三種密度控制的現象。

　　為了符合場發射顯示器低電壓操作的目的,我們利用一控制閘極來製造奈米碳管之發射三極元件。然而,傳統的三極結構（二氧化矽-多晶矽）有一個很嚴重的問題,那就是低發射效率,大概是 1.23 % 左右。因此我們在傳統的三極結構中加入了一個氮化矽絕緣層來克服這個問題。從模擬來看,當加入了氮化矽絕緣層之後,閘極附近的電位線有變疏的現象,而且電位線的分佈也因此被改變。另一方面,氮化矽絕緣層將會阻擋部分的電子發射到閘極端因此使閘極的漏電流下降。綜合上述的原因,這將會使得更多的電子穿越過閘極的區域而到達陽極端,因此場發射效率將會被提升。如果氮化矽絕緣層是加在多晶矽的上方的話,其發射效率將會增加到 8.56 %,而且也因為維持了閘極的控制力,故使得陽極的場發射電流密度高達 5.44 mA/cm^2.

Optimization for the Field Emission Properties of Carbon Nanotubes with Proper Densities and Device Structures

Student : Jiun-Kai Shiu   Advisor : Dr. Huang-Chung Cheng

Department of Electronic Engineering &

Institute of Electronics

National Chiao Tung University

Abstract

The density of CNTs synthesized by thermal CVD was still too high to reduce the field emission current density and ascend the turn-on field due to the screening effects. In this thesis, three novel methods including two thin Ti capping layer processes and a co-deposition of Ti and Fe process were introduced to improve the field emission properties via controlling the density of CNTs. For the thin Ti capping layer without pre-treatment, the field emission properties were poor. For the thin Ti capping layer with pre-treatment, the field emission current density improved from 11.12 mA/cm^2 to 97.6 mA/cm^2 at the electric field of 6 V/μm and the turn-on field decreased from 3.786 V/μm to 2.5 V/μm when the density of CNTs diminished from 2.8x10^8 emitter/cm^2 to 2.8x10^7 emitter/cm^2. However, the uniformity was not still improved from the luminescent images. For the co-deposition of Fe and Ti, the atoms of Fe and Ti were uniform

distribution during the sputtering, so it could obtain a more uniform catalytic metal layer. This showed the co-deposition technique could improve the uniformity of CNTs and expect that a large size field emission display with higher resolution would be fabricated in the future. Besides, two mechanisms were put forward to expound these phenomena of three density control methods.

The CNTs triode structures with an extraction gate were proposed to achieve the low voltage modulation. However, the traditional triode structure (oxide-poly) had a serious problem of low efficiency (1.23 %). In order to overcome this problem, the traditional triode structure adding a nitride insulting layer was introduced. From the simulations, the electrostatic potential near the gate electrode was getting sparse and the distribution of electrostatic potential was also changed after adding a nitride insulting layer. On the other hand, the nitride insulting layer would block some electrons emitting to the gate electrode hence cause the reduction of gate leakage current. Sum up these reasons, it would make more electrons to pass through the gate holes and collect by the anode hence cause the increase of efficiency. If the nitride insulting layer was acceding above the poly-Si, the efficiency was added to 8.56 % and the emission anode current density was about 5.44 mA/cm^2 which might result from the keeping of gate controllability.

誌 謝

Contents

Chapter 2 By Modification of Ti to Control the Density of CNTs and Improve the Field Emission Properties

Chapter 3 By Modification of Triode Structure to Improve the Efficiency of Field Emission Properties of CNTs

Chapter 4 Conclusions and Future Prospects

Table Lists

Chapter 1

Chapter 2

Chapter 3

Figure Captions

Chapter 1

Figure 1-1　The SEM micrograph of (a) Spindt type triodes array, (b) Spindt type field emission triode

Figure 1-2　The schematic diagram of (a) conventional CRT, (b) FED.

Figure 1-3　Energy diagrams of vacuum-metal boundary: (a) without external electric field; (b) with an external electric field.

Figure 1-4　The FED products based on Spindt type field emitters, (a) motorola 5.6" color FED, (b) Pixtech 5.6" color FED, (c) Futaba 7" color FED and (d) Sony/Candescent 13.2" color FED.

Figure 1-5　(a) Si tip formed by isotropic etching and (b) Si tip field emission triodes array formed by CMP

Figure 1-6　(a) SEM image of SCE cathode array (b) structure of SED (c) a 36-inch prototype of surface conduction electron emitter display

Figure 1-7　High-resolution transmission electron microscopy images of (a) single-walled nanotubes (SWNTs) and (b) multiwalled nanotubes (MWNTs). Every layer in the image (fringe) corresponds to the edges of each cylinder in the nanotube assembly.

Figure 1-8　Molecular models of single-walled nanotubes with different helicities: (a) zig-zag arrangement; (b) armchair configuration; (c) and (d) two different helicities.

Figure 1-9　(a) SEM image of CNT cathode from Samsung's FED, (b) a 4.5-inch FED from Samsung, the emitting image of fully sealed SWNT-FED at color mode with red, green, and blue phosphor columns, and (c) a prototype of 5" CNT flat panel display by Samsung

Chapter 2

% in the co-deposition of Fe and Ti were deposited on the 50-nm-thick Ti buffer layer at applied electric field 5, 6, and 7 V/μm, respectively. The distance of spacer was 100 μm and these samples were square cells with length of 1 cm.

Chapter 1

Introduction

1.1 Overview of Vacuum Microelectronics

1.1.1 History

Since the invention of solid state transistors in the late 1940s, vacuum tubes have been gradually replaced by those tiny volume, low cost, better reliability, and more power efficient solid state devices. With great improvements on semiconductor manufacturing technology for the past decades, the so called vacuum microelectronic devices using the professional micro fabrication technology have been successfully fabricated and gave a new life to vacuum electronics. "Vacuum state" devices have a number of remarkable advantages with respect to the present "solid state" devices, including fast carrier drift velocity, radiation hardness, and temperature insensitivity. For example, the saturation drift velocity is limited to less than 3×10^7 cm/s in all semiconductor due to scattering mechanism whereas the saturation drift velocity in vacuum is limited theoretically to 3×10^{10} cm/s and practically to about $6\text{-}9\times10^8$ cm/s [1.1]. Moreover, because there is no medium to be damaged, either temporarily or permanently radiation effect should be negligible in vacuum devices. Additionally, there is no medium for electrons fly in the vacuum, so there is no lattice scattering or bulk carrier generation/recombination. Therefore, the vacuum microelectronic devices can suffer to 500℃ or above as long as the structures of the vacuum devices do not destroyed [1.2]. Table 1-1 shows the comparison between vacuum microelectronic and semiconductor devices.

Recent development in vacuum microelectronics started in 1928, when R. H. Fowler and L. W. Nordheim published the first theory of electron field emission from metals using quantum mechanics [1.3]. This theory is contrary to thermionic emission, which metals have to be heated so that some of the electrons in metal gain enough thermal energy to overcome

the metal/vacuum barrier; according to the Fowler-Nordheim theory, an applied electric field of approximately 10^3 V/μm is needed for electrons to tunnel through the sufficiently narrow barrier [1.3]. To reach this high field at reasonable applied voltage, it is customary to machine the field emitters into protruding objects to take advantage of field enhancement. It was not until 1968 when C. A. Spindt camp up with a fabrication method to create very small dimension metal cones that vacuum microelectronic triodes became possible [1.2]. Figure 1-1 is a schematic diagram of the triode fabricated by Spindt. From the late 1960s to the year 1990, Ivor Brodie, Henry F. Gray, and C. A. Spindt made many contributions to this field. Also, most of research was focused on the devices similar to the Spindt cathode during the past three decades.

In 1991, a group of research of the French company LETI CHEN reported a microtip display at the fourth International Vacuum Microelectronics Conference [1.4]. Their display was the first announcement of a practical vacuum microelectronic device. From then on, a great amount of researchers all over the world devoted themselves to this interesting, challenging, and inventive field. Part of the work focused on fabricating very small radius silicon tip by utilizing modern VLSI technology [1.5-1.6]. Some of them increased the emission current by coating different metals, such as W, Mo, Ta, Pt etc., even diamond on field emission arrays [1.7-1.9]. Different device schemes also have been proposed to enhance the emission current density, stability, and reliability.

1.1.2 Applications of Vacuum Microelectronic Devices

Among wide range applications of the vacuum microelectronics, the first commercial product could be the field emission flat-panel display [1.10-1.14]. The field emission fluorescent display is basically a thin cathode ray tube (CRT), which was first proposed by SRI International and later demonstrated by LETI [1.4].

Various kinds of flat-panel displays, such as liquid crystal display (LCD),

electroluminescent display (EL), vacuum fluorescent display (VFD), plasma display panel (PDP), and light emitting display (LED), are developed for the better characteristics of small volume, light weight, and low power consumption. LCDs have become the most popular flat panel displays, however, LCDs have some drawbacks, such as poor viewing angle, temperature sensitivity and low brightness. As a result, some opportunities still exist and waiting for the solutions from other flat panel displays such as FED.

1.1.3 Field Emission Displays

FED features all the pros of the CRTs in image quality and is flat and small volume. The schematic comparisons are revealed in Figure 1-2. The operation of CRTs involves deflection of the beam in such a way that the electron spot scans the screen line-by-line. In FEDs, multiple electron beams are generated from the field emission cathode and no scanning of beams is required. The cathode is a part of the panel substrate consists of an X-Y electrically addressable matrix of field emission arrays (FEAs). Each FEA is located at the intersection of a row and a column conductor, with the row conductor serving as the gate electrode and the column conductor as the emitter base. The locations where the rows and columns intersect define a pixel. The pixel area and number of tips are determined by the desired resolution and luminance of the display. Typically, each pixel contains an FEA of 4-5000 tips. The emission current required for a pixel varies from 0.1 to 10 μA, depending on the factors such as the luminance of the display, phosphor efficiency and the anode voltage. Compared to the active matrix LCDs, FEDs generate three times the brightness with wilder viewing angle at the same power level. Full color FEDs have been developed by various research groups from different aspects such as PixTech, Futaba, Fujitsu, Samsung, are presently engaged in commercially exploiting FED.

1.1.4 Theory Background

Electron field emission is a quantum mechanical tunneling phenomenon of electrons extracted from the conductive solid surface, such as a metal or a semiconductor, where the surface electric field is extremely high. If a sufficient electric field is applied on the emitter surface, electrons will be emitted through the surface potential barrier into vacuum, even under a very low temperature. In contrast, thermionic emission is the hot electron emission under high temperature and low electric field. Figure 1-3(a) demonstrates the band diagram of a metal-vacuum system.

Here W_0 is the energy difference between an electron at rest outside the metal and an electron at rest inside the metal, whereas W_f is the energy difference between the Fermi level and the bottom of the conduction band. The work function ϕ is defined as $\phi = W_0 - W_f$. If an external bias is applied, vacuum energy level is reduced and the potential barrier at the surface becomes thinner as shown in Figure 1-3(b). Then, an electron having energy "W" has a finite probability of passing through the surface barrier. Fowler and Nordheim derive the famous F-N equation (1.1) as follow [1.3]:

$$J = \frac{aE^2}{\phi t^2(y)}\exp[-b\phi^{\frac{3}{2}}v(y)/E],\tag{1-1}$$

where J is the current density (A/cm^2). E is the applied electric field (V/cm), ϕ is the work function (in eV), a = 1.56×10^{-6}, b = -6.831×10^{-7}, y = $3.79\times10^{-4}\times10^{-4}E^{1/2}/\phi$, $t^2(y)\sim1.1$ and v(y) can be approximated as [1.15]

$$v(y) = \cos(0.5\pi y),\tag{1-2}$$

or

$$v(y) = 0.95 - y^2.\tag{1-3}$$

Typically, the field emission current I is measured as a function of the applied voltage V. Substituting relationships of J = I/α and E = βV into Eq.(1-1), where α is the emitting area and β is the local field enhancement factor at the emitting surface, the following equation can

be obtained

$$I = \frac{A\alpha\beta^2 V^2}{\phi t^2(y)} \exp[-bv(y)\frac{\phi^{\frac{3}{2}}}{\beta V}].$$ (1-4)

Then taking the log. form of Eq. (1-4) and v(y) ~ 1

$$\log(\frac{I}{V^2}) = \log[1.54 \times 10^{-6} \frac{\alpha\beta^2}{\phi t^2(y)}] - 2.97 \times 10^7 (\frac{\phi^{\frac{3}{2}} v(y)}{\beta V}),$$ (1-5)

from Eq. (1-5), the slope of a Fowler-Nordheim (F-N) plot is given by

$$S \equiv slope_{FN} = -2.97 \times 10^7 (\frac{\phi^{\frac{3}{2}}}{\beta}),$$ (1-6)

The parameter β can be evaluated from the slope S of the measured F-N plot if the work function ϕ was known

$$\beta = -2.97 \times 10^7 (\frac{\phi^{\frac{3}{2}}}{S}) \ (cm^{-1}),$$ (1-7)

The emission area α can be subsequently extracted from a rearrangement of Eq. (1-5)

$$\alpha = (\frac{I}{V^2}) \frac{\phi}{1.4 \times 10^{-6} \beta^2} \exp(\frac{-9.89}{\sqrt{\phi}}) \exp(\frac{6.53 \times 10^7 \phi^{\frac{3}{2}}}{\beta V}) \ (cm^2).$$ (1-8)

For example, the electric field at the surface of a spherical emitter of radius r concentric with a spherical anode (or gate) of radius r+d can be represented analytically by

$$E = \frac{V}{r}(\frac{r+d}{d}),$$ (1-9)

Though a realistic electric field in the emitter tip is more complicated than above equation, we can multiple Eq.(1-9) by a geometric factor $\beta^{\text{`}}$ to approximate the real condition.

$$E_{tip} \equiv \text{function of (r,d)} = \beta^{\text{`}} \frac{V}{r}(\frac{r+d}{d}),$$ (1-10)

where r is the tip radius of emitter tip, d is the emitter-anode(gate) distance and $\beta^{\text{`}}$ is a geometric correction factor [1.16].

For a very sharp conical tip emitter, where d >> r, E$_{tip}$ approaches to $\beta^{\text{`}}$(V/r). And for

r>>d, E_{tip} approaches to $\beta`(V/d)$ which is the solution for a parallel-plate capacitor and for a diode operation in a small anode-to-cathode spacing.

As the gated FEA with very sharp tip radius, Eq. (1-10) can be approximated as:

$$E_{tip} = \beta`(V/r). \tag{1-11}$$

Combining E = βV and Eq. (1-11), we can obtain the relationship:

$$E_{tip} = \beta V = \beta`(V/r), \text{ and } \beta` = \beta r. \tag{1-12}$$

The tip radius r is usually in the range from a few nm to 50 nm, corresponding to the parameter $\beta`$ ranging from 10^{-1} to 10^{-2}.

Besides, transconductance g_m of a field emission device is defined as the change in anode current due to a change in gate voltage [1.1].

$$g_m = \frac{\partial I_C}{\partial V_g}|_{Vc}, \tag{1-13}$$

Transconductance of a FED is a figure of merit that gives as an indication of the amount of current charge that can be accomplish by a given change in grid voltage. The transconductance can be increase by using multiple tips or by decreasing the gate-to-cathode spacing for a given anode-to-cathode spacing.

According to the above mention equations (especially Eq.1-5), the following approaches may therefore be taken to reduce the operating voltage of the field emission devices:

1) Find techniques to reproducibly sharpen the tips to the atomic level (increase β).

2) Lower the work function of the tip (ϕ).

3) Narrow the cone angle (increase β).

4) Reduce the gate-opening diameter (increase β).

1.2 Cathode Structures and Materials for Field Emission Displays

FED is one of the most promising emissive type flat-panel displays, which can overcome

the drawbacks of TFT-LCD, such as poor viewing angle, temperature sensitivity and low brightness. However, some difficult technological subjects should be considered such as microfabrication of cathodes, assembly technology with accuracy of micrometer level, vacuum technology to keep stable field emission in small space of flat panels and high efficiency phosphor materials. This section introduces some novel cathode structures and synthesizes these novel emitter materials for FED operations.

1.2.1 Spindt-type Field Emitters

The "Spindt" cathode was first proposed by C. A. Spindt in 1968 [1.17]. Figure 1-1 demonstrated the scanning electron microscope (SEM) image of a spindt type field emission triode [1.18], which was invented by Spindt of SRI and improved for the electron source of high-speed switching devices or microwave devices [1.2]. Meyer of LETI presented the capability of using Spindt-type emitters for a display in 1970s [1.19] and stabilized the field emission from Spindt-type emitters by introducing a resistive layer as the feedback resistance.

This proposal triggered the development of field emitters as an electron source of displays by researchers and electronics makers in 1990. The merits of the Spindt type field emitters are summarized as following: (1) High emission current efficiency, more than 98% anode current to cathode current can be achieved for the symmetric structure of Spindt tip and the gate hole, the lateral electric field to the metal tip can be cancelled out. (2) The fabrication is self-aligned, easy process; uniform field emission arrays can be fabricated easily. Some research groups have successfully fabricated commercial FED products based on Spindt type field emitters such as motorola, Pixtech, Futaba and Sony/Candesent.[1.20], the products of above mentioned companies are shown in Figures 1-4.

However, there are some existing drawbacks of Spindt type field emitters when fabricating Spindt type FED such as (1) High gate driving voltage required; for a Spindt type field emission triode with 4 μm gate aperture, the driving voltage is typically more than 60 V,

which results in the high cost of the driving circuits. To reduce the gate driving voltage, frontier lithography technologies such as E beam lithography must be applied to reduce the gate aperture to the sub-micron level. (2) The emission property degrades for the chemically instable of the metal tips. (3) Huge, expensive high vacuum deposition system required during fabricating large area Spindt type FED.

1.2.2 Si Tip Field Emitters

An alternative approach to fabricate tip type field emitters is to fabricate the Si tip field emitters based on the semiconductor fabricating process. Figures 1-5 depict the SEM micrographs of Si tips array, Si tip field emission triodes array formed by chemical mechanical polishing (CMP) [1.21] and double gate of Si field emitter arrays [1.22]. Symmetric device structure and similar advantages with Spindt type field emitters can be obtained. However, high temperature oxidation sharpening process prohibits Si tip from large area fabrication.
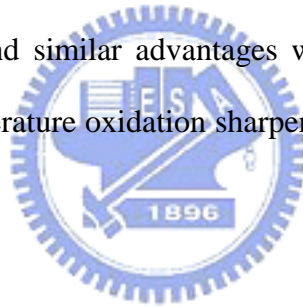
1.2.3 Carbon and Nano-sized Emitters

Carbon nanotubes have attracted a great deal of interest owing to their advantageous properties, such as high aspect ratios, small tip radius of curvature, high Young's modulus, capability for the storage of a large amount of hydrogen, and structural diversities that make it possible for band gap engineering. These useful properties of carbon nanotubes (CNTs) make themselves good candidates for various applications, for instance, wires for nanosized electronic devices, super strong cables, AFM tips, charge-storage devices in battery, and field emission display.

1.2.4 Surface Conduction Electron Emitter (SCE)

The SED, based on a new type of flat-panel display technology, was created Canon and

Toshiba. Like conventional CRTs, SEDs utilize the collision of electrons with a phosphor-coated screen to emit light. The key technology to the electron emitters begins with the creation of an extremely narrow slits (~ several nanometers) between two electric poles in thin film of PdO (Palladium Oxide). Electrons are emitted from one side of the slit when approximately 10 V of electricity are applied. Some of these electrons are scattered at the other side of the silt and accelerated by the voltage (approximately 10 kV) applied between the glass substrates; causing light to be emitted when they collide with the phosphor-coated glass plate. The PdO film is coated by inject printing or screen-printing technology and this is a low cost process. The major problem of SED is that the efficiency is still low and the power consumption will be very high. Figure 1-6 shows the SEM image of SCE cathode array, structure and a 36-inch display of SED [1.23-1.24].

1.3 Field Emission Properties of Carbon Nanotubes

1.3.1 Structure and Properties of Carbon Nanotubes

Recently, carbon nanotubes have attracted a lot of attention owing to their unique properties and potential for various applications. The discovery of nanotubes happened in 1991 when Sumio Iijima of NEC Corporation found these tiny needles, consisting of concentric graphite tubes, on the electrodes used to prepare fullerenes [1.25]. Nanotubes can be divided into two categories. The first is called multiwalled carbon nanotubes (MWNTs). MWNTs are close to hollow graphite fibers [1.26], except that they have a much higher degree of structural perfection. They are made of sheets of carbon atoms with a cylindrical shape and generally consist of co-axially arranged 2 to 20 cylinders「Figure 1-7(b)」. The interlayer spacing in MWNT ($d_{(002)}$ = 0.34 nm) is slightly larger than that in single crystal graphite ($d_{(002)}$ = 0.335 nm) [1.27]. This is attributed to a combination of tubule curvature and van der Waals force interactions between successive garphene layers. The second type of the

9

nanotube is made up of just a single layer of carbon atoms. These nanotubes are called the single-walled nanotubes (SWNTs) and possess good uniformity in diameter about 1.2 nm 「Figure 1-7(a)」. They are close to fullerenes in size and have a single-layer cylinder extending from end to end [1.28-1.29].

These unique structural properties are ascribed to the building material of nanotube---carbon. Carbon is the elemental equivalent of the perfect neighbor, friendly, and easygoing. Under intense pressure, carbon atoms form co-valence bonds with four neighbor atoms, creating the pyramidal arrangement of diamond. However, the activation energy of diamond is very high and carbon usually links up with just three neighbors, creating the hexagonal rings of graphite network. The arrangement of graphite has a host of unpaired electrons, which essentially float above or below the plane of carbon rings. In this arrangement, the electrons have more freedom to move around the graphite surface, which makes the material a good electrical conductor.

Carbon nanotubes consist of concentric hexagon-rich cylinders, made up of sp^2 hybridized carbon, as in graphite, and terminated by end-caps arising from the presence of 12 pentagons (six per end). It is possible to construct a cylinder by rolling up a hexagonal graphene sheet in different ways. Two of these are "non-helical" in the sense that the graphite lattices at the top and bottom of the tube are parallel. These arrangements are named "armchair" and "zig-zag". In the armchair structure, two C-C bonds on opposite sites of each hexagon are perpendicular to the tube axis, whereas in the zig-zag arrangement, these bonds are parallel to the tube axis 「Figure 1-8 (a)(b)」. In all other conformation, the C-C bonds lie at an angle to the tube axis and a helical structure is obtained 「Figure 1-8 (c)(d)」.

Theoretical calculations have predicted that all the armchair tubes are metallic whereas the zig-zag and helical tubes are either metallic or semiconducting [1.30-1.31]. The electronic conduction process in nanotubes is unique since in the radial direction, the electrons are confined in the singular plane of the graphene sheet. The conduction occurs in the armchair

(metallic) tubes through gapless modes as the valence and conduction bands cross each other at the Fermi energy. In most helical tubes, which contain large numbers of atoms in their unit cell, the one-dimensional band structure shows an opening of the gap at the Fermi energy, and this leads to semiconducting properties. This unique electronic behavior only occurs for small nanotubes. As the diameter of the tubes increases, the band gap (which varies inversely with the tube diameter) tends to zero, yielding a zero-gap semiconductor that is electronically equivalent to the planar graphene sheet. In a MWNT, the outer planar graphene-like tubes superimpose the electronic structure of the inner tubes. This has been proved by several experiments [1.32-1.33] where the band structure obtained from individual MWNT resembles that of graphite. Experiments have indicated that the pentagonal defects present at the tips can induce metallic character by introducing sharp resonance in the local density of states near the Fermi energy [1.33]. Similar metallization of nanotubes is also found to occur through the substitutional doping of the nanotube lattice with impurities such as boron and nitrogen [1.34].

1.3.2 Potential Applications of Carbon Nanotubes

Since the discovery of CNTs in 1991, they have been attracting much attention for their unique physical and chemical properties, such as high aspect ratio, low work function (5 ev), small tip radius of curvature, high chemical stability, high mechanical strength, high conductivity, and electron emission properties [1.35-1.36]. Therefore, one of the most potential application of carbon nanotubes is as the field emission material in vacuum microelectronics, such as flat-panel field-emission displays (FEDs), nanoprobes of atomic force microscopes (AFMs), microsensors, scanning tunneling microscopes (STMs) and microsized intense electron sources.

According to Fowler-Nodiem theory, the electric field at the apex of a needle-shaped tip is enhanced by a factor $\beta = h/r$, where h is the height of the tip and r is the radius of curvature

of the tip apex. The carbon nanotube is a stable form of carbon and can be synthesized by several techniques. They are typically made as threads about 10-100 nm in diameter with a high aspect ratio (>1000). These geometric properties, coupled with their high mechanical strength and chemical stability, make carbon nanotubes attractive as electron field emitters. Several groups have recently reported good electron field emission from nanotubes [1.37-1.39].

In 1999, Samsung pronounced a 4.5-inch carbon nanotube based field emission display (Figure 1-9(b)). They mixed a conglomeration of single-walled CNTs into a paste with a nitrocellulose binder and squeezed the concoction through a 20-μm mesh onto a series of metal strips mounted on a glass plate (Figure 1-9(a)). As the CNTs emerged from the mesh, they were forced into a vertical position. The metal strips with the CNTs sticking out of them served as the back of the display. The front of the display was a glass plate containing red, green, and blue phosphors and strips of a transparent indium-tin-oxide anode running from side to side. The glass plates were separated by spacers with the thickness of 200 μm. Once assembled, the edges were sealed and air was pumped out of the display.

Samsung's 5-inch carbon nanotube based field emission display (Figure 1-9(c)) could be the precursor of a new generation of more energy efficient, high performance flat panel displays for portable computers [1.40]. The CNTs appear to be durable enough to provide the 10000-h lifetime considered being a minimum for an electronic product. The panel consumes just half the power of an LCD to generate an equivalent level of screen brightness. They could also be cheaper than LCDs or other types of field emission displays being developed. Until now, at last five major Japanese electronic manufactures are working on this technology.

1.4 Thesis Organization

In chapter 1, the overview of vacuum microelectronics, basic principles of field emission

theory and applications of carbon nanotubes are described.

In chapter 2, we reveal the synthesis of the carbon nanotubes and improve field emission characteristics of carbon nanotubes by a thin Ti capping layer or co-deposition process. These simple methods to produce the patterned carbon nanotubes using thermal CVD are introduced. Then, the capping layer process and co-deposition process are introduced to reduce the turn-on field and improve the emission current density. Moreover, the issues of reliability and uniformity of carbon nanotubes are discussed in this chapter.

In chapter 3, the triode structures acceded a nitride insulating layer are fabricated to reduce the gate leakage and improve the field emission efficiency. Because only a small fraction of electrons can pass through the gate holes and collected by the anode, we introduce these triode structures to change the distribution of electric field to draw more electrons toward the anode.

Finally, the conclusions and recommendations for future researches are provided in chapter 4.

Chapter 2

By Modification of Ti to Control the Density of CNTs and Improve the Field Emission Properties

2.1 Motivation

As the field emission displays are going to be commercialized, it is very important to find a suitable cold cathode with low operating voltage and high emission current. According to the theory of field emission, Fowler-Nordheim tunneling, low work function (ϕ), high field enhancement factor (β), and large emission area (α) are desirable for a high field emission current density.

For the techniques of silicon tips, several methods have been used to obtain a large enhancement factor β via sharpening the silicon tips, such as large oblique-angle thermal evaporation or sputtering to fabricate sharp metal cones, high temperature oxidation to sharpen silicon tips, or anisotropic etching of silicon using KOH to produce sharp tip molds. However, these methods to fabricate sharp tips need extra fabrication process with complexity. The novel material, CNTs, therefore, is proposed to be one of the most promising materials as the cathodes in field emission displays.

The high density of CNTs can provide a great deal of field emission sites which can raise the emission current density (due to the increase of the emission area, α) but the density of CNTs will affect the field enhancement factor (β) which is also strongly relative to the emission properties of CNTs. For CNTs with high density, the screening effects reduce the field enhancement factor (β), therefore, suppress the field emission current density [2.1-2.3], as shown in Figure 2-1. Obviously, it is important to obtain an optimized density of CNTs to improve the field emission properties, such as turn-on field, threshold field, and emission current density. Well control of density and surface morphology of CNTs is thus required for

applications in the near future. To effectively control the density of CNTs, three novel methods including two thin Ti capping layer processes and a co-deposition of Ti and Fe process are introduced to improve the emission properties via controlling the density of CNTs in this chapter.

2.2 Introduction

Carbon nanotubes (CNTs) have attracted great deal of attention because of its outstanding physical properties and potential applications since its first observation by Iijima in 1991 [2.4]. Due to several unique properties, such as high aspect ratio, low work function (5 ev), small tip radius of curvature, high chemical stability, high mechanical strength, high conductivity, and electron emission properties [2.5-2.6], it has been considered as one of the most potential materials for field emission displays. Besides, CNTs is also a very wonderful materials in many applications, such as flat-panel field-emission displays (FEDs), nanoprobes of atomic force microscopes (AFMs), microsensors, scanning tunneling microscopes (STMs) and microsized intense electron sources. Nowadays, several methods have been developed to synthesize CNTs, such as arc discharge [2.7-2.8], laser ablation [2.9], screen-printing [2.10-2.12], plasma-enhanced CVD [2.13], electron cyclotron resonance CVD [2.14], microwave plasma-enhanced CVD [2.15], and thermal CVD [2.16-2.17]. Generally speaking, arc-produced CNTs, laser-produced CNTs, and screen-printing techniques are used to fabricate low-cost CNT field-emission in diode structure for field-emission displays. However, the drawbacks are that the specific purification processes for arc-produced and laser-produced CNTs are required, and the uniformity of screen-printed CNT field-emitter arrays is not applicable in filed emission displays. The selective growth of CNTs by chemical vapor deposition (CVD) processes without extra purification or screen-printing process, therefore, sufficient for fabricating field-emission devices with better uniformity. Besides, via the CVD

process, the CNTs can be grown with great vertical align which can also increase the effective local electric field when a voltage is applied. For these reasons, the thermal CVD, a simple, low cost, and well-developed method, is preferred to synthesize the CNTs in this thesis.

However, some critical issues such as screening effects, reliability, high driving voltage, uniformity, and vacuum package have not been solved for the application of field emission displays. The effect of screening electric field by the dense arrangement of CNTs has been reported by several groups [2.1-2.3]. If the CNTs are too closely spaced, the electric field will be screened out. Groning *et al.* reported the field enhancement factor β of the tips decreases rapidly when the inter-tip spacing is smaller than twice the length of the tips. They also found that the maximum current density is obtained when the spacing between the tips is about two times their relative height by simulations, as shown in Figure 2-1. For larger spacing the current density decreases due to the decreasing the field emission sites, with a nearly constant emission current per tip as the field enhancement factor remains constant. For smaller spacing the current density decreases rapidly due to the decreasing β factor and this effect cannot be compensated for by increasing the field emission sites from tips. This shows that when the spacing between the emitting structures on a surface becomes comparable to its length, problems of shielding do occur and will limit the emission current density.

Therefore, the turn-on field of the high-density-CNTs is still high because of the screening effects, as shown in Figure 2-2. To obtain better field emission properties, the density of CNTs should be optimized. However, the density of CNTs synthesized by thermal CVD is too high and the screening effects are very serious. Many researches have reported different methods to suppress this phenomenon, such as plasma treatment [2.18-2.21], wet etching method [2.22], screen-printing method used pastes with different CNT contents [2.23-2.24], E-beam lithography [2.25-2.26], anodic aluminum oxide (AAO) nanoporous templates [2.27-2.28], excimer laser irradiation [2.29], and etc.. Most of the methods will increase the complexity in processes of fabrication or cause a defective affection on the CNTs.

In this chapter, three novel processes including two kinds of thin Ti capping layer and a co-deposition of Ti and Fe process are proposed to modify the density of CNTs grown by thermal CVD. With different thicknesses of the Ti capping layer on hydrogen pretreated catalytic nanoparticles or different weight percentages of Ti co-deposited with catalyst, Fe, the density of CNTs can be controlled simply without the need of extra high cost or high complex processes. By controlling the density of CNTs, these methods can reduce the turn-on field and threshold field, and improve the field emission current density due to the suppressing of the screening effects. Furthermore, reliability is also a very important issue for field emission displays if it is going to be commercialized. The main factors to affect the lifetime of a CNTs-based emitter are the adhesion and the contact resistance between the CNTs and the substrate. With the novel methods proposed in this chapter, the adhesion can be increased to obtain a higher electric breakdown field and the contact resistance can also be suppressed to avoid the Joule heating when the devices are operated in a high current density condition [2.30-2.31].

2.3 Experiments

In this chapter, three novel methods including a thin Ti capping layer without pre-treatment, a thin Ti capping layer with pre-treatment, and co-deposited Fe with Ti, had been put forward to control the density of CNTs. Thereinafter, discussed about these three kinds of methods separately.

2.3.1 A Thin Ti Capping Layer without Pre-treatment

2.3.1.1 Experimental Procedures

The fabrication procedures of patterned CNT emitters were shown schematically in Figures 2-3(a) ~ 2-3(e). As shown in Figure 2-3(a), about 1-μm-thick photoresist was

spin-coated on an n-type silicon wafer (100) with low resistance and square cells with lengths of 10 μm, 100 μm, and 1000 μm were defined by photolithography. Then a Ti layer with 50-nm in thickness was deposited by the E-beam evaporation system as a buffer layer and a Fe layer with 5-nm in thickness was deposited subsequently as catalytic metal in the same system, as shown in Figure 2-3(b). The Fe/Ti (5 nm/50 nm) patterns were formed after the photoresist was removed by lift-off method as depicted in Figure 2-3(c). With different thicknesses (0, 0.5, 1, 2, and 4 nm) of a thin Ti capping layer was deposited in the sputtering system shown in Figure 2-3(d). Finally, CNTs were grown selectively by thermal CVD system to investigate the growth phenomenon and the field emission properties of CNTs that was shown in Figure 2-3(e). The samples with different Ti capping layers were loaded into the thermal CVD chamber (Figure 2-4(a) and (b)) to grow CNTs in atmospheric pressure at 700 ℃ with C_2H_4 (5 sccm) for 10 min as depicted in Figure 2-4(c).

Scanning electron microscopy (SEM) was performed to discover the density and the morphology of CNTs. A high-vacuum measurement environment with a base pressure of 5×10^{-6} Torr was set up to characterize the field emission properties of CNTs (Figure 2-5). Cathode contact was made directly on the wafer. A glass plate coated with indium-tin-oxide (ITO) was positioned 120 μm to 160 μm above the sample surface as an anode. All cables were shielded except for the ground return path to the power source. The emission current densities of CNTs were measured as a function of applied electric field, using Keithley 237 high voltage units as DC source and Keithley 238 high current units as ground source. The measurement instruments were auto-controlled by the computer with IEEE 488 interface.

2.3.1.2 Results and Discussion

The corresponding thicknesses of the thin Ti capping layer were 0 nm, 0.5 nm, 1 nm, 2 nm, and 4 nm in SEM images from a 45° viewing angle as shown in Figures 2-6 (a), (b), (c), (d), and (e), respectively. From the SEM observation, the density of CNTs decreased if the

thickness of the thin Ti capping layer increased. As a speculation, the thin Ti capping layer could hinder the growth of CNTs as a diffusion barrier. With thicker Ti capping layer, the probability of carbon radicals to diffuse into the catalyst would be reduced therefore reduced the growth of CNTs. To estimate the density of CNTs, the SEM images were taken from top view and were shown in Figures 2-7 (a) ~ (e). To calculate the quantity conveniently, the pictures were divided into one fourth and then estimated the number of CNTs. Afterwards, the number which was multiplied by four was approximate density value. The approximate densities of CNTs could be counted and listed in Table 2-1(a). For the case of 0-nm-thick Ti capping layer, the density of CNTs was about 8.8×10^8 emitter/cm^2. With the increase of thickness of Ti capping layer, the density of CNTs was getting low. When the thickness of the thin Ti capping layer was increased to 4 nm, the density of CNTs had already dropped to 3×10^6 emitter/cm^2.

The field emission properties of CNTs with different thicknesses of the thin Ti capping layer were shown in Figure 2-8(a) which showed the relationship between emission current density and electric field (J-E). The corresponding Fowler-Nordheim plots for CNTs were depicted in Figure 2-8(b) and the linearity slope of the plots confirmed the field emission phenomena. From Table 2-1, the turn-on field defined at 10 μA/cm^2 of CNTs decreased from 4.071 V/μm to 3.545 V/μm with the thickness of Ti capping layer was increased from 0 nm to 2 nm. From the SEM images, the density of CNTs also dropped from 8.8×10^8 to 8×10^6 emitter/cm^2. This phenomenon may results from the suppression of the screening effects which can increase the field enhancement factor (β) hence reduce the turn-on field. However, the turn-on field did not always decrease with the increase in the thickness of the thin Ti capping layer. When the thickness of the thin Ti capping layer was added to 4 nm, the turn-on field would rise to 4 V/μm resulting from the decrease in the length of CNTs which would cause the reduction of aspect ratio and make the decline in the field enhancement factor (β).

The field emission current density was improved from 1.568 mA/cm^2 to 10.2 mA/cm^2 at

electric field of 6 V/μm when the thickness of the thin Ti capping layer was from 0 nm to 2 nm, respectively. With a 4-nm Ti capping layer, the field emission current density dropped greatly as compared to the 2-nm one. It might result from the great reduction of emitting sites which could reduce the field emission current density effectively. With changing the thicknesses of the thin Ti capping layer from 0 nm to 4 nm, the field emission current density of CNTs was achieved to threshold field, which was defined at 10 mA/cm^2, as the thickness of the thin Ti capping layer was 2 nm. Table 2-1(b) showed the summarized field emission properties of CNTs grown with different thicknesses of the thin Ti capping layer. The simulations of literature [2.23] predict that an inter-tube distance of about 2 times the height of CNTs optimizes the emitted current per unit area. In this experiment, the length of CNTs was probably 1 μm and this would correspond to an ideal density of 2.5×10^7 emitter/cm^2 by simulation. However, the optimum thin Ti capping layer thickness, 2 nm, was found out in this experiment and the density of CNTs of this sample was about 8×10^6 emitter/cm^2 which was similar to paper survey [2.23].
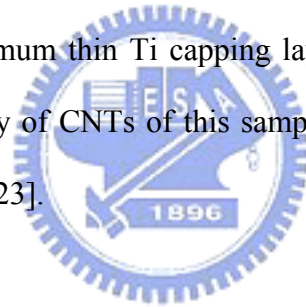
2.3.1.3 Summary

The density of CNTs could be controlled with different thicknesses of the thin Ti capping layer without pre-treatment and reduced the turn-on field and improved the field emission current density due to the suppression of screening effects. Low density could reduce the turn-on field, however, the number of the emitting sites would also be reduced hence cause the reduction in field emission current density. So it needed an optimized the thickness of the Ti capping layer to gain a reasonable field emission current density. In this experiment, the optimum thickness of thin Ti capping layer was found out to be 2 nm and the density of CNTs was altered from 8.8×10^8 emitter/cm^2 to 8×10^6 emitter/cm^2. The field emission current density was improved from 1.568 mA/cm^2 to 10.2 mA/cm^2 at the electric field of 6 V/μm and the turn-on field was decreased from 4.071 V/μm to 3.545 V/μm with the thickness of the Ti

capping layer increased from 0 nm to 2 nm. As a consequence, the experimental results revealed that the improvement of the field emission properties could be achieved by optimizing the density of CNTs with proper thin Ti capping layer thickness.

2.3.2 A Thin Ti Capping Layer with Pre-treatment

2.3.2.1 Experimental Procedures

The fabrication procedures of patterned CNT emitters were shown schematically in Figures 2-9(a) ~ 2-9(f). As shown in Figure 2-9(a), about 1-μm-thick photoresist was spin-coated on an n-type silicon wafer (100) with low resistance and square cells with lengths of 10 μm, 100 μm, and 1000 μm were defined by photolithography. Then a Ti layer with 50-nm in thickness was deposited by the E-beam evaporation system as a buffer layer and a Fe layer with 5-nm in thickness was deposited subsequently as catalytic metal in the same system, as shown in Figure 2-9(b). The Fe/Ti (5 nm/50 nm) patterns were formed after the photoresist was removed by lift-off method as depicted in Figure 2-9(c). Afterward the sample was pre-treated in the thermal CVD chamber in atmospheric pressure at 700 ℃ with H_2 (500 sccm) and CH_4 (200 sccm) for 5 min to form catalytic Fe nanoparticles as depicted in Figure 2-9(d). With different thicknesses (0, 1, 2, 4, 10, and 20 nm) of a thin Ti capping layer was deposited in the sputtering system shown in Figure 2-9(e). Finally, CNTs were grown selectively by thermal CVD system to investigate the growth phenomenon and the field emission properties of CNTs that was shown in Figure 2-9(f). The samples with different Ti capping layers were loaded into the thermal CVD chamber (Figure 2-4(a) and (b)) to grow CNTs in atmospheric pressure at 700 ℃ with C_2H_4 (5 sccm) for 10 min as depicted in Figure 2-4(c).

Scanning electron microscopy (SEM) was performed to discover the density and the morphology of CNTs. The wall structure and crystallinity of CNTs were determined by

high-resolution transmission electron microscopy (HRTEM) and the components of nanoparticles were analyzed by energy dispersive spectroscopy (EDS). A high-vacuum measurement environment with a base pressure of 5×10^{-6} Torr was set up to characterize the field emission properties of CNTs (Figure 2-5). Cathode contact was made directly on the wafer. A glass plate coated with indium-tin-oxide (ITO) was positioned 120 μm to 160 μm above the sample surface as an anode. All cables were shielded except for the ground return path to the power source. The emission current densities of CNTs were measured as a function of applied electric field, using Keithley 237 high voltage units as DC source and Keithley 238 high current units as ground source. The measurement instruments were auto-controlled by the computer with IEEE 488 interface.

2.3.2.2 Results and Discussion

The SEM images of pre-treated Fe catalytic nanoparticles with different thicknesses of the thin Ti capping layer were shown in Figure 2-10. The thin Ti capping layer with 0 nm, 1 nm, 2 nm, 4 nm, 10 nm, 20 nm were corresponded to Figures 2-10(a), (b), (c), (d), (e), and (f), respectively. Figure 2-10(a) showed that the diameters of catalytic nanoparticles after pre-treatment were distributed randomly. With a 1-nm-thick Ti capping layer deposited after pre-treatment, some catalytic nanoparticles with small diameters were buried under the thin Ti capping layer, as shown in Figure 2-10(b). Form Figure 2-10(c), when the thickness of thin Ti capping layer was added to 2 nm, this phenomenon was come out to be more obvious due to more catalytic nanoparticles were buried under the increased Ti capping layer. Therefore, only some of catalytic nanoparticles with large diameters were remained as depicted in Figure 2-10(d). As the thickness of the Ti capping layer was increased to 10 nm or 20 nm, the samples in SEM images had only rough surfaces but obvious nanoparticles as displayed in Figures 2-10(e) and (f). Afterward, the samples with different thicknesses of Ti capping layers were loaded into the thermal CVD chamber to grow CNTs. The SEM images in Figure 2-11

showed the morphologies of subsequently grown CNTs. The corresponding thicknesses of the thin Ti capping layer were 0 nm, 1 nm, 2 nm, 4 nm, 10 nm, and 20 nm in SEM images from a 45° viewing angle as shown in Figures 2-11 (a), (b), (c), (d), (e), and (f), respectively. From the SEM observation, the density of CNTs decreased if the thickness of the thin Ti capping layer increased. It could be found that the thin Ti capping layer could hinder the growth of CNTs and the thickness of the thin Ti capping layer could be modified to control the density of CNTs. To estimate for the density of CNTs, the SEM images from the top view were taken in Figures 2-12 (a) ~ (f) corresponded to Figures 2-11 (a) ~ (f). To calculate the quantity conveniently, the pictures were divided into one fourth and then estimated the number of CNTs. Afterwards, the number which was multiplied by four was approximate density value. The approximate densities of CNTs were counted and listed in Table 2-2(a). For the sample without the Ti capping layer, the density of CNTs was about 2.8×10^8 emitter/cm^2. When the thickness of the thin Ti capping layer was increased to 20 nm, the density of CNTs had already dropped to much less than 1×10^6 emitter/cm^2.

In order to investigate the microstructure of CNTs, the high resolution transmission microscope (HRTEM) images were taken in Figure 2-13. The HRTEM images of CNTs with low magnification were shown in Figures 2-13(a) and (b). A nanoparticle was enclosed in the CNTs as shown in Figure 2-13(a). From the HRTEM images with high magnification in Figures 2-13(c) and (d), the layer-by-layer structure of graphite could be clearly observed. It could also demonstrate that the CNT in this TEM image was a multi-wall structure. Moreover, the composition of the catalytic nanoparticle was analyzed by energy dispersive spectrum (EDS) via the TEM instrument. The EDS spectrum in Figure 2-14 showed that only Fe, C, and Cu existed in the results of the EDS analysis. The peaks of Cu were from the Cu mesh which was used to hold CNTs in the TEM system. The peak of C was from the CNT and the peaks of Fe were from the catalytic nanoparticle enclosed in the CNT. No signal of Ti was detected which indicated that the Fe would not form the alloy with Ti in this process. From

the images of HRTEM and the analysis of EDS, Fe played a critical role in the growth of CNTs and Ti seemed not involve in the formation of CNTs by Ti-Fe alloy.

The field emission properties of CNTs with different thicknesses of the thin Ti capping layer were shown in Figure 2-15(a) which showed the relationship between the emission current density and the electric field (J-E). The corresponding Fowler-Nordheim plots for CNTs were also depicted in Figure 2-15(b) and the negative slope confirmed the Fowler-Nordheim tunneling phenomena. The turn-on field defined at 10 μA/cm^2 of CNTs decreased from 3.786 V/μm to 2.107 V/μm with the thickness of the Ti capping layer increased from 0 nm to 4 nm. It might result from the suppression of the screening effects with the density of CNTs dropped from 2.8×10^8 emitter/cm^2 to 1.2×10^7 emitter/cm^2. However, the turn-on field did not always decrease with the increase in the thickness of the thin Ti capping layer. When the thickness of the Ti capping layer was added to 10 nm, the turn-on field would rise to 3.85 V/μm. It might due to the decrease in the length of CNTs which would result in the reduction of aspect ratio and cause the decline in the field enhancement factor (β). When the thickness of the Ti capping layer was added to 20 nm, there was almost no CNT could be observed via the SEM images due to the thickness of the Ti capping layer was too thick for carbon radicals to diffuse into the catalytic nanoparticles. The threshold field defined at 10 mA/cm^2 of CNTs field emission diode decreased from 5.857 V/μm to 3.5 V/μm with the thickness of the thin Ti capping layer increased from 0 nm to 2 nm. The density of CNTs was decreased from 2.8×10^8 emitter/cm^2 to 2.8×10^7 emitter/cm^2. Here, the rise of the threshold field when the thickness of the thin Ti capping layer was 4 nm might due to the reduction of field emission sites.

The field emission current density was improved from 11.12 mA/cm^2 to 97.6 mA/cm^2 at electric field of 6 V/μm when the thickness of the thin Ti capping layer was increased from 0 nm to 2 nm, respectively. When the thickness of the thin Ti capping layer was 4 nm, the field emission current density dropped to 20.48 mA/cm^2 at 6 V/μm because of the reduction of

field emission sites. Moreover, if the thickness of the thin Ti capping layer was over 2 nm, the field emission current density reduced with the increase of thickness and the field emission current density was almost zero when the thickness of the Ti capping layer was 20 nm. Table 2-2(b) showed the summarized field emission properties of CNTs grown with different thicknesses of the thin Ti capping layer. The simulations of literature [2.23] predict that an inter-tube distance of about 2 times the height of CNTs optimizes the emitted current per unit area. In this experiment, the average length of CNTs was probably 1 μm and this would correspond to an ideal density of 2.5×10^7 emitter/cm^2 by simulation. From the experimental results, the optimum thin Ti capping layer thickness, 2 nm, was found out in this experiment and the density of CNTs of this sample was about 2.8×10^7 emitter/cm^2 which was similar to the simulation results in the literature [2.23].

2.3.2.3 Summary

The density of CNTs could be controlled by a deposition with different thicknesses of the thin Ti capping layer on pretreated catalytic nanoparticles therefore reduced the turn-on field and improved the field emission current density. It might due to the suppression of screening effect. In this experiment, the optimum thin Ti capping layer thickness, 2 nm, was found out and the field emission current density improved from 11.12 mA/cm^2 to 97.6 mA/cm^2 at the electric field of 6 V/μm, the turn-on field decreased from 3.786 V/μm to 2.5 V/μm, and the density of CNTs was about 2.8×10^7 emitter/cm^2 which was similar to simulations for suppression the phenomenon of screening effect. As a consequence, the experimental results revealed that improved the field emission properties can be achieved by optimizing the density of CNTs under proper thin Ti capping layer thickness.

2.3.3 Co-deposited Fe with Ti

2.3.3.1 Experimental Procedures

The fabrication procedures of patterned CNT emitters were shown schematically in Figures 2-16(a) ~ 2-16(d). As shown in Figure 2-16(a), about 1-μm-thick photoresist was spin-coated on an n-type silicon wafer (100) with low resistance and square cells with lengths of 10 μm, 100 μm, and 1000 μm were defined by photolithography. Then a Ti layer with 50-nm in thickness was deposited by the E-beam evaporation system as a buffer layer and 5-nm-thick catalytic metal, Fe, was co-deposited subsequently with different weight percentages of Ti in the same system, as shown in Figure 2-16(b). Then the patterns were formed after the photoresist was removed by lift-off method as depicted in Figure 2-16(c). Finally, CNTs were grown selectively by thermal CVD system to investigate the growth phenomenon and the field emission properties of CNTs that was shown in Figure 2-16(d). In the thermal CVD chamber, the samples with different weight percentages of Ti were pre-treated in atmospheric pressure at 700 ℃ with H_2 (500 sccm) and CH_4 (200 sccm) for 5 min to form catalytic Fe nanoparticles and grown CNTs subsequently in atmospheric pressure at 700 ℃ with C_2H_4 (5 sccm) for 10 min as depicted in Figure 2-16(e).

Scanning electron microscopy (SEM) was performed to discover the density and the morphology of CNTs. The wall structure and crystallinity of CNTs were determined by high-resolution transmission electron microscopy (HRTEM) and the components of nanoparticles were analyzed by energy dispersive spectroscopy (EDS). A high-vacuum measurement environment with a base pressure of 5×10^{-6} Torr was set up to characterize the field emission properties of CNTs (Figure 2-5). Cathode contact was made directly on the wafer. A glass plate coated with indium-tin-oxide (ITO) was positioned 120 μm to 160 μm above the sample surface as an anode. All cables were shielded except for the ground return path to the power source. The emission current densities of CNTs were measured as a function of applied electric field, using Keithley 237 high voltage units as DC source and Keithley 238

high current units as ground source. The measurement instruments were auto-controlled by the computer with IEEE 488 interface. The cathode luminescence could be obtained from the ITO glass with P22 phosphor coating on it.

2.3.3.2 Results and Discussion

Figures 2-17 (a) ~ (e) showed the SEM images of CNTs from the top view with different weight percentages of Ti corresponded to 0 %, 36 %, 53 %, 70 %, and 85 %, respectively. From the SEM observation, the density of CNTs decreased if the weight percentage of Ti in the co-deposition of Fe and Ti increased. To calculate the quantity conveniently, the pictures were divided into one fourth and then estimated the number of CNTs. Afterwards, the number which was multiplied by four was approximate density value. For the case of weight percentage of Ti was 0 %, the density of CNTs was about 8×10^9 emitter/cm^2. With the increase of weight percentage of Ti, the density of CNTs was getting low. When the weight percentage of Ti was increased to 85 %, the density of CNTs had already dropped to 8×10^6 emitter/cm^2. The approximate densities of CNTs could be counted and listed in Table 2-3(a). As a speculation, the percentage of Fe catalytic nanoparticles buried under the Ti film could be increased with the increase of weight percentage of Ti and the Ti film could hinder the growth of CNTs as a diffusion barrier. With thicker Ti film, the probability of carbon radicals to diffuse into the catalyst would be reduced therefore reduced the growth of CNTs. To estimate the length of CNTs, the SEM images were taken from a 90° viewing angle and were shown in Figures 2-18 (a) ~ (e) corresponded to Figures 2-17 (a) ~ (e). With the increase of weight percentage of Ti, on the one hand the turn-on field would be raised resulted from the shortening of length of CNTs, on the other hand the turn-on field would be lowered which might result from the decrease of density of CNTs. So there would be appearances of optimal value between the two mechanisms and they would be verified later.

In order to investigate the microstructure of CNTs, the high resolution transmission

microscope (HRTEM) images were taken in Figure 2-19. Figure 2-19(a) showed the HRTEM image of CNTs with low magnification and a nanoparticle was enclosed in the CNTs. From the HRTEM images with high magnification in Figures 2-19(b), the layer-by-layer structure of graphite could be clearly observed. It could also demonstrate that the CNT in this TEM image was a multi-wall structure. Moreover, the composition of the catalytic nanoparticle was analyzed by energy dispersive spectrum (EDS) via the TEM instrument. The EDS spectrum in Figure 2-20 showed that only Fe, C, and Cu existed in the results of the EDS analysis. The peaks of Cu were from the Cu mesh which was used to hold CNTs in the TEM system. The peak of C was from the CNT and the peaks of Fe were from the catalytic nanoparticle enclosed in the CNT. No signal of Ti was detected which indicated that the Fe would not form the alloy with Ti in this process. From the images of HRTEM and the analysis of EDS, Fe played a critical role in the growth of CNTs and Ti seemed not involve in the formation of CNTs by Ti-Fe alloy.

The field emission properties of CNTs with different weight percentages of Ti were shown in Figure 2-21(a) which showed the relationship between emission current density and electric field (J-E). The corresponding Fowler-Nordheim plots for CNTs were depicted in Figure 2-21(b) and the linearity slope of the plots confirmed the field emission phenomena. From Table 2-3, the turn-on field defined at 10 $\mu A/cm^2$ of CNTs decreased from 3.679 V/μm to 3 V/μm with the weight percentage of Ti in the co-deposition of Fe and Ti increased from 0 % to 53 %. It might result from the suppression of the screening effects with the density of CNTs dropped from 8×10^9 emitter/cm^2 to 5×10^8 emitter/cm^2. However, the turn-on field did not always decrease with the increase in the weight percentage of Ti. When the weight percentage of Ti was added to 70 %, the turn-on field would rise to 4.594 V/μm. It might due to the decrease in the length of CNTs which would result in the reduction of aspect ratio and cause the decline in the field enhancement factor (β). When the weight percentage of Ti was added to 85 %, only little CNTs could be observed via the SEM images due to the majority of

Fe catalytic nanoparticles buried under the Ti film and the Ti film could hinder the growth of CNTs as a diffusion barrier. With thicker Ti film, the probability of carbon radicals to diffuse into the catalyst would be reduced therefore reduced the growth of CNTs. The threshold field defined at 10 mA/cm^2 of CNTs field emission diode decreased from 5.75 V/μm to 4.706 V/μm with the weight percentage of Ti increased from 0 % to 36 %. The density of CNTs was decreased from 8x10^9 emitter/cm^2 to 2x10^9 emitter/cm^2. Here, the rise of the threshold field when the weight percentage of Ti was 53 % might due to the reduction of field emission sites. The field emission current density was improved from 8 mA/cm^2 to 26.96 mA/cm^2 at electric field of 5.5 V/μm when the weight percentage of Ti was increased from 0 % to 36 %, respectively. When the weight percentage of Ti was 53 %, the field emission current density dropped to 8.24 mA/cm^2 at 5.5 V/μm because of the reduction of field emission sites. Moreover, if the weight percentage of Ti was over 36 %, the field emission current density reduced with the increase of weight percentage of Ti and the field emission current density was almost zero when the weight percentage of Ti was 85 %. Table 2-3(b) showed the summarized field emission properties of CNTs grown with different weight percentages of Ti.

Figure 2-22 showed the luminescent images on the ITO anode with phosphor coating on it. The distance of spacer was 100 μm and these samples were square cells with length of 1 cm. Samples (a), (b), and (c) showed the Fe/Ti (5 nm/50 nm) film at applied electric field 5, 6, and 7 V/μm, respectively. With the increase of electric field, the brightness of luminescent image would be increased and these three images were all revealed poor uniformity from Figures 2-22 (a), (b), and (c) observation. Samples (d), (e), and (f) showed the Fe/Ti (5 nm/ 50 nm) film and a 2-nm-thick Ti capping layer was deposited after pre-treatment at applied electric field 5, 6, and 7 V/μm, respectively. In Figures 2-22 (d), (e), and (f), the field emission current density would be larger and the luminescent images would also be more bright corresponded to Figures 2-22 (a), (b), and (c). However, the uniformity had not been improved by these methods. Samples (g), (h), and (i) showed the weight percentage of Ti was

36 % in the co-deposition of Fe and Ti were deposited on the 50-nm-thick Ti buffer layer at applied electric field 5, 6, and 7 V/μm, respectively. From Figures 2-22 (g), (h), and (i) observation, the uniformity would be improved obviously and the brightness of luminescent image was sufficient for commercial application at applied electric field 7 V/μm.

2.3.3.3 Summary

The density of CNTs could be controlled with different weight percentages of Ti and reduced the turn-on field and improved the field emission current density due to the suppression of screening effects. Low density could reduce the turn-on field, however, the number of the emitting sites would also be reduced hence cause the reduction in field emission current density. So it needed an optimized weight percentage of Ti to gain a reasonable field emission current density. In this experiment, the optimum weight percentage of Ti was found out to be 36 %. The field emission current density was improved from 8 mA/cm^2 to 26.96 mA/cm^2 at the electric field of 5.5 V/μm and the turn-on field was decreased from 3.679 V/μm to 3.059 V/μm with the weight percentage of Ti increased from 0 % to 36 %. From the luminescent images observation, the uniformity would be improved obviously by the co-deposition of Fe and Ti and the brightness on the ITO anode was sufficient for commercial application at applied electric field 7 V/μm.

2.4 Mechanisms

In order to realize the growing processes of CNTs for three novel methods including a thin Ti capping layer without pre-treatment, a thin Ti capping layer with pre-treatment, and co-deposited Fe with Ti, two mechanisms were put forward in this section. According to Lindemann Criterion as depicted in Figure 2-23 (a), when the thickness of film is decreased to nanometer degree the melting point may be dropped to 1/3 and the liquid-like metal can be

congregated due to the cohesion. In terms of the Lindemann's theory, the vibrations among the atoms are called mean square displacement (MSD) which is rapidly increased with higher temperature. Figure 2-23 (b) showed the primitive situation of films after deposition. The temperature was up to 700℃ when the growth of CNTs so it was possible for the Ti atoms to move around the surface due to the decrease of Ti film thickness to nano-size and the increase of thermionic energy of Ti atoms even if the bulk melting point of Ti was 1668℃. When the Ti atoms moved to the Ti buffer layer and merged each other due to the cohesion and the surface energy, the Fe catalytic nanoparticles might be revealed out and the carbon radicals could diffuse into the catalytic metal to grow the CNTs as shown in Figure 2-23 (c). Another synthetical mechanism was that the Fe catalytic nanoparticles might not be revealed out directly and a very thin Ti film was remained after the Ti atoms moved to the Ti buffer layer and merged each other. However, the carbon radicals could still overcome the diffusion barrier of very thin Ti film and diffuse through the very thin Ti film into the catalytic metal to grow the CNTs as shown in Figure 2-23 (d). Therefore, the vapor-liquid-solid (VLS) model could happen when the Fe catalytic nanoparticles might be revealed out directly and a Ti film was thin enough to carbon radicals could overcome.

2.5 Conclusions

For CNTs of high density, screening effects raised the turn-on field and reduced the field enhancement factor (β) and thus the emitted current. CNTs of low density yielded low current density essentially because the emitter density and the field enhancement factor (β) were low. For CNTs of proper density, there was an ideal compromise between the emitter density and the intertube distance, which was sufficiently large to avoid screening effects. In this chapter, to effectively control the density of CNTs, three novel methods including two thin Ti capping layer processes and a co-deposition of Ti and Fe process were introduced to improve the

emission properties via controlling the density of CNTs.

For the thin Ti capping layer without pre-treatment, the optimum thickness of thin Ti capping layer was found out to be 2 nm and the density of CNTs was altered from 8.8×10^8 emitter/cm^2 to 8×10^6 emitter/cm^2. The field emission current density was improved from 1.568 mA/cm^2 to 10.2 mA/cm^2 at the electric field of 6 V/μm and the turn-on field was decreased from 4.071 V/μm to 3.545 V/μm with the thickness of the Ti capping layer increased from 0 nm to 2 nm. However, the field emission properties were not good enough for this method.

For the thin Ti capping layer with pre-treatment, the density of CNTs could be controlled by a deposition with different thicknesses of the thin Ti capping layer on pretreated catalytic nanoparticles. In this experiment, the optimum thin Ti capping layer thickness, 2 nm, was found out. The field emission current density improved from 11.12 mA/cm^2 to 97.6 mA/cm^2 at the electric field of 6 V/μm with the thickness of the Ti capping layer increased from 0 nm to 2 nm. The turn-on field of 2.5 V/μm and threshold field of 3.5 V/μm were obtained at the turn-on current of 10 μA/cm^2 and the threshold current of 10 mA/cm^2. The density of CNTs was about 2.8×10^7 emitter/cm^2 which was similar to simulations for suppression the phenomenon of screening effects. However, the field emission properties could be improved apparently than first density control method, but the uniformity was not still improved from the luminescent images observation.

For the co-deposition of Fe and Ti, the optimum weight percentage of Ti was found out to be 36 %. The field emission current density was improved from 8 mA/cm^2 to 26.96 mA/cm^2 at the electric field of 5.5 V/μm with the weight percentage of Ti increased from 0 % to 36 %. The turn-on field was decreased from 3.679 V/μm to 3.059 V/μm and the threshold field was decreased from 5.75 V/μm to 4.706 V/μm with the weight percentage of Ti increased from 0 % to 36 %. From the luminescent images observation, the uniformity would be improved obviously by the co-deposition of Fe and Ti. Although the field emission

properties had not been superior to second density control method, they had been enough to commercial application. As a consequence, the co-deposition of Fe and Ti was a very promising method to suppress the screening effects and improve the uniformity of CNTs.

Chapter 3

By Modification of Triode Structure to Improve the Efficiency of Field Emission Properties of CNTs

3.1 Motivation

A high anode voltage of more than 500 V is required to excite the phosphor resulted in the extremely high driving voltage of diode-type FED. To reduce the required driving voltage, triode-type FED are proposed and characterized. However, triode-type FED has a serious problem to be solved that is efficiency. Heralded as the new generation of high-quality large flat-screen display in Figures 3-1(a) and (b), the SED [3.1-3.2], jointly developed by Canon and Toshiba Corporation, is almost ready for practical applications. But the field emission efficiency Ie/If is only about 3 ~ 4 % as shown in Figures 3-1(c) and (d), it will cause the consumption of the power. To the traditional triode-type structure (oxide-poly) of CNT emitters in this thesis, there are the same problem with efficiency is about 1 ~ 2 % as depicted in Figure 3-2. In Figure 3-3, the simulations of electrostatic potential and electric field are worked out to find out the reason. It can be observed that the electrostatic potential of the gate is the densest and the electric field of the gate is also the most powerful so the majority of electrons are emitted to the gate and only a small fraction of electrons can pass through the gate holes and collected by the anode. This is the main reason causing the decline of efficiency. In this chapter, the traditional triode-type structure (oxide-poly) acceded a nitride insulating layer are introduced to improve the field emission efficiency and reduce the gate leakage which may result from the change of the electrostatic potential distribution and the suppression of some electrons to reach the gate electrode.

3.2 Introduction

CNTs have attracted increasing attention owing to the promising applications in vacuum microelectronics. Several groups [3.3-3.7] have demonstrated the low turn on electric field properties and extremely large emission current of the CNTs field emission diodes. However, the driving voltage of the diode-type FED is still too high. To lower the required driving voltage, triode-type FED is proposed and characterized to cost down the driving circuits. Triode-type FED employing arc-produced CNTs is therefore demonstrated to reduce the driving voltage. Lee, *et al* [3.8] have fabricated a gated CNT-FED by employing a metal mesh as the gate electrode and achieved the turn-on voltage of 100 V. Wang, *el al* [3.9] have demonstrated a triode-type FED with a specific filling method to reduce the operation voltage. That is not merely these methods, nowadays, several methods have been developed to synthesize the triode-type FED of CNT emitters, such as poly-gate structure [3.10-3.11], metal-gate structure [3.12-3.13], under-gate structure [3.14-3.15], and focus-gate structure [3.16-3.18]. However, they have a common problem to be solved that is efficiency and the lost efficiency will cause the consumption of the power. In the literature, there is not an effective method to put forward at present. In this thesis, two novel triode structures including oxide-nitride-poly and oxide-poly-nitride are proposed to improve the field emission efficiency and reduce the gate leakage.

3.3 Experiments

In this chapter, one traditional triode structure with oxide-poly and two novel triode structures including oxide-nitride-poly and oxide-poly-nitride had been put forward to compare the field emission efficiency with each other. Thereinafter, discussed about these three kinds of triode structures separately.

3.3.1 The Triode Structure with Oxide-Poly Composition

3.3.1.1 Experimental Procedures

The fabrication procedures of the triode structure with oxide-poly composition were shown schematically in Figures 3-4(a) ~ 3-4(g). As shown in Figure 3-4(a), a 1-μm-thick silicon dioxide layer was thermally grown on an n-type Si(100) substrate at 1050 ℃ and a 350-nm-thick poly-Si layer was subsequently deposited on the thermal oxide by low pressure chemical vapor deposition (LPCVD) using a pure SiH_4 gas at 620 ℃. The poly-Si layer was further doped by $POCl_3$ at 950 ℃ for 40 min. About 1-μm-thick photoresist was spin-coated on the poly-Si and square cells with lengths of 10 μm were defined by photolithography [Figure 3-4(b)]. Firstly, the poly-Si layer was dry etched by the RIE200L using SF_6 for 190 s and the parameter would cause the lateral etching of poly-Si. The under cut of poly-Si gate was therefore formed as gate-to-emitter gap about 2.7 μm to avoid the short circuit problem as depicted in Figure 3-4(c). Secondly, the SiO_2 layer was laterally etched in the wet etching solution of BOE, the etching time was precisely controlled, which acts as the interelectrode gap of the fabricated device [Figure 3-4(d)]. Employing the previously patterned photoresist layer as the shadow mask, a Ti layer with 50-nm in thickness was deposited by the E-beam evaporation system as a buffer layer and a Fe layer with 5-nm in thickness was deposited subsequently as catalytic metal in the same system [Figure 3-4(e)]. The SEM image was shown in Figure 3-6(a). Then Fe/Ti (5 nm/50 nm) patterns were formed after the photoresist was removed by lift-off method as shown in Figure 3-4(f) and the SEM image was revealed in Figure 3-6(b). Finally, CNTs were grown selectively by thermal CVD system to investigate the growth phenomenon and the field emission properties of CNTs that was shown in Figure 3-4(g). In the thermal CVD chamber [Figure 3-5(a) and 3-5(b)], the samples were pre-treated in atmospheric pressure at 700 ℃ with H_2 (500 sccm) and CH_4 (200 sccm) for 5 min to form catalytic Fe nanoparticles and grown CNTs subsequently in atmospheric pressure at 700 ℃ with C_2H_4 (5 sccm) for 5 min as depicted in Figure 3-5(c).

Scanning electron microscopy (SEM) was performed to observe the structure of oxide-poly composition and the morphology of CNTs. A high-vacuum measurement environment with a base pressure of 5×10^{-6} Torr was set up to characterize the field emission properties of triode-type of CNT emitters. A glass plate coated with indium-tin-oxide (ITO) was positioned 500 μm above the sample surface as an anode. The measurement instruments were auto-controlled by the computer with IEEE 488 interface.

3.3.1.2 Results and Discussion

Figure 3-6(c) showed the SEM micrograph of the fabricated device arrays and the CNTs emitter layers were selectively deposited within the emitter areas. An array of 50x50 square patterns with the length of 10 μm was defined and the equivalent emitter area was about 250000 μm^2. Figures 3-6(d) and 3-6(e) revealed the SEM images of a single triode device from a cross-sectional viewing angle of the triode structure using oxide-poly composition with low magnification and high magnification, respectively. The average height of the CNTs was about 400-500 nm and the gap between the gate and CNTs was about 2.7 μm.

The field emission properties of triode structure with oxide-poly composition were shown in Figures 3-7 and 3-8 which discussed the relationship between emission current density and supply voltage (J-V). The emission gate current density (Jg) and emission anode current density (Ja) were measured as a function of gate voltage (Vg) with the anode voltage kept at 1000 V as depicted in Figure 3-7(a) and 3-7(b), respectively. The linearity of Fowler-Nordheim plot exhibited in the inset of Figure 3-7(b) clarified the field emission phenomena. The emission gate current density and the emission anode current density were about 65.2 mA/cm^2 and 0.81 mA/cm^2, respectively, as the gate voltage of 100 V. Therefore, the anode current density was much smaller than the gate current density and the ratio was about 1.23 %. From the simulations of Figure 3-3 observation, this was due to the fact that a large electric field was created by the gate voltage and most emitted electrons were drawn

toward the gate. Only a small fraction of electrons could pass through the gate holes and be collected by the anode. This was the main reason causing the decline of efficiency. Figure 3-8 revealed the emission anode current density versus anode voltage under different gate bias. When the anode voltage exceeded 800 V, the emission anode current density was about 0.6 mA/cm^2 to 1.0 mA/cm^2 with the gate voltage kept at 100 V.

3.3.2 The Triode Structure with Oxide-Nitride-Poly Composition

3.3.2.1 Experimental Procedures

The fabrication procedures of the triode structure with oxide-nitride-poly composition were shown schematically in Figures 3-9(a) ~ 3-9(g). As shown in Figure 3-9(a), a 1-μm-thick silicon dioxide layer was thermally grown on an n-type Si(100) substrate at 1050 ℃. A 300-nm-thick nitride layer was then deposited on the thermal oxide by low pressure chemical vapor deposition (LPCVD) using SiH_2Cl_2 and NH_3 mixture at 800 ℃. A 350-nm-thick poly-Si layer was subsequently deposited on the nitride by LPCVD using a pure SiH_4 gas at 620 ℃. The poly-Si layer was further doped by $POCl_3$ at 950 ℃ for 40 min. About 1-μm-thick photoresist was spin-coated on the poly-Si and square cells with lengths of 10 μm were defined by photolithography [Figure 3-9(b)]. Firstly, the poly-Si layer was dry etched by the RIE200L using SF_6 for 190 s and the parameter would cause the lateral etching of poly-Si. The under cut of poly-Si gate was therefore formed as gate-to-emitter gap about 2.7 μm to avoid the short circuit problem as depicted in Figure 3-9(c). Secondly, the nitride layer was dry etched by the same system using CF_4 and O_2 mixture for 210 s. Thirdly, the SiO_2 layer was laterally etched in the wet etching solution of BOE, the etching time was precisely controlled, which acts as the interelectrode gap of the fabricated device [Figure 3-9(d)]. Employing the previously patterned photoresist layer as the shadow mask, a Ti layer with 50-nm in thickness was deposited by the E-beam evaporation system as a buffer layer and a

Fe layer with 5-nm in thickness was deposited subsequently as catalytic metal in the same system [Figure 3-9(e)]. The SEM image was shown in Figure 3-10(a). Then Fe/Ti (5 nm/50 nm) patterns were formed after the photoresist was removed by lift-off method as shown in Figure 3-9(f) and the SEM image was revealed in Figure 3-10(b). Finally, CNTs were grown selectively by thermal CVD system to investigate the growth phenomenon and the field emission properties of CNTs that was shown in Figure 3-9(g). In the thermal CVD chamber [Figure 3-5(a) and 3-5(b)], the samples were pre-treated in atmospheric pressure at 700 ℃ with H_2 (500 sccm) and CH_4 (200 sccm) for 5 min to form catalytic Fe nanoparticles and grown CNTs subsequently in atmospheric pressure at 700 ℃ with C_2H_4 (5 sccm) for 5 min as depicted in Figure 3-5(c).

Scanning electron microscopy (SEM) was performed to observe the structure of oxide-nitride-poly composition and the morphology of CNTs. A high-vacuum measurement environment with a base pressure of 5×10^{-6} Torr was set up to characterize the field emission properties of triode-type of CNT emitters. A glass plate coated with indium-tin-oxide (ITO) was positioned 500 μm above the sample surface as an anode. The measurement instruments were auto-controlled by the computer with IEEE 488 interface.

3.3.2.2 Results and Discussion

Figure 3-10(c) showed the SEM micrograph of the fabricated device arrays and the CNTs emitter layers were selectively deposited within the emitter areas. An array of 50x50 square patterns with the length of 10 μm was defined and the equivalent emitter area was about 250000 μm². Figures 3-10(d) and 3-10(e) revealed the SEM images of a single triode device from a cross-sectional viewing angle of the triode structure using oxide-nitride-poly composition with low magnification and high magnification, respectively. The average height of the CNTs was about 400-500 nm and the gap between the gate and CNTs was about 2.7 μm.

The field emission properties of triode structure with oxide-nitride-poly composition were shown in Figures 3-11 and 3-12 which discussed the relationship between emission current density and supply voltage (J-V). The emission gate current density (J_g) and emission anode current density (J_a) were measured as a function of gate voltage (V_g) with the anode voltage kept at 1000 V as depicted in Figure 3-11(a) and 3-11(b), respectively. The linearity of Fowler-Nordheim plot exhibited in the inset of Figure 3-11(b) clarified the field emission phenomena. The emission gate current density and the emission anode current density were about 14.02 mA/cm^2 and 2.01 mA/cm^2, respectively, as the gate voltage of 100 V. Therefore, the ratio of anode current density to total current density was about 12.54 % so the efficiency had risen obviously. From the simulations of electrostatic potential in Figure 3-13, two kinds of phenomena explained this reason. Firstly, it could be observed that the electrostatic potential near the gate electrode was getting sparse and the distribution of electrostatic potential was also changed resulting from acceding a nitride insulting layer between oxide and poly. Consequently, it would cause more electrons to pass through the gate holes and reach the anode electrode hence bring out the raise of efficiency. Secondly, because of the nitride insulting layer was added under the poly-Si layer, some electrons below the poly gate could be blocked from emitting to the gate electrode. Obviously, it would make the decline of gate leakage and the increase of efficiency. Figure 3-12 revealed the emission anode current density versus anode voltage under different gate bias and no significant increase of emission anode current density was discovered as the anode voltage exceeded 200 V which represented that the field emission current was dominated by the gate voltage.

3.3.3 The Triode Structure with Oxide-Poly-Nitride Composition

3.3.3.1 Experimental Procedures

The fabrication procedures of the triode structure with oxide-poly-nitride composition

were shown schematically in Figures 3-14(a) ~ 3-14(g). As shown in Figure 3-14(a), a 1-μm-thick silicon dioxide layer was thermally grown on an n-type Si(100) substrate at 1050 ℃. A 350-nm-thick poly-Si layer was subsequently deposited on the thermal oxide by low pressure chemical vapor deposition (LPCVD) using a pure SiH_4 gas at 620 ℃. The poly-Si layer was further doped by $POCl_3$ at 950 ℃ for 40 min. Afterwards a 300-nm-thick nitride layer was deposited on the poly-Si layer by LPCVD using SiH_2Cl_2 and NH_3 mixture at 800 ℃. About 1-μm-thick photoresist was spin-coated on the nitride layer and square cells with lengths of 10 μm were defined by photolithography [Figure 3-14(b)]. At the beginning, the nitride layer was dry etched by the RIE200L using CF_4 and O_2 mixture for 210 s as shown in Figure 3-14(c). After that the poly-Si layer was dry etched by the same system using SF_6 for 190 s and the parameter would cause the lateral etching of poly-Si. The under cut of poly-Si gate was therefore formed as gate-to-emitter gap about 2.7 μm to avoid the short circuit problem. Lastly the SiO_2 layer was laterally etched in the wet etching solution of BOE, the etching time was precisely controlled, which acts as the interelectrode gap of the fabricated device [Figure 3-14(d)]. Then a Ti layer with 50-nm in thickness was deposited by the E-beam evaporation system as a buffer layer and a Fe layer with 5-nm in thickness was deposited subsequently as catalytic metal in the same system [Figure 3-14(e)]. The SEM image was shown in Figure 3-15(a). The Fe/Ti (5 nm/50 nm) patterns were formed after the photoresist was removed by lift-off method as shown in Figure 3-14(f) and the SEM image was revealed in Figure 3-15(b). CNTs were grown selectively by thermal CVD system to investigate the growth phenomenon and the field emission properties of CNTs that was shown in Figure 3-14(g). In the thermal CVD chamber [Figure 3-5(a) and 3-5(b)], the samples were pre-treated in atmospheric pressure at 700 ℃ with H_2 (500 sccm) and CH_4 (200 sccm) for 5 min to form catalytic Fe nanoparticles and grown CNTs subsequently in atmospheric pressure at 700 ℃ with C_2H_4 (5 sccm) for 5 min as depicted in Figure 3-5(c).

Scanning electron microscopy (SEM) was performed to observe the structure of

oxide-poly-nitride composition and the morphology of CNTs. A high-vacuum measurement environment with a base pressure of 5×10^{-6} Torr was set up to characterize the field emission properties of triode-type of CNT emitters. A glass plate coated with indium-tin-oxide (ITO) was positioned 500 μm above the sample surface as an anode. The measurement instruments were auto-controlled by the computer with IEEE 488 interface.

3.3.3.2 Results and Discussion

Figure 3-15(c) showed the SEM micrograph of the fabricated device arrays and the CNTs emitter layers were selectively deposited within the emitter areas. An array of 50x50 square patterns with the length of 10 μm was defined and the equivalent emitter area was about 250000 μm^2. Figures 3-15(d) and 3-15(e) revealed the SEM images of a single triode device from a cross-sectional viewing angle of the triode structure using oxide-poly-nitride composition with low magnification and high magnification, respectively. The average height of the CNTs was about 400-500 nm and the gap between the gate and CNTs was about 2.7 μm. The experimental date was extracted by averaging measurement data.

The field emission properties of triode structure with oxide-poly-nitride composition were shown in Figures 3-16 and 3-17 which discussed the relationship between emission current density and supply voltage (J-V). The emission gate current density (Jg) and emission anode current density (Ja) were measured as a function of gate voltage (Vg) with the anode voltage kept at 1000 V as depicted in Figure 3-16(a) and 3-16(b), respectively. The linearity of Fowler-Nordheim plot exhibited in the inset of Figure 3-16(b) clarified the field emission phenomena. The emission gate current density and the emission anode current density were about 58.14 mA/cm^2 and 5.44 mA/cm^2, respectively, as the gate voltage of 100 V. Therefore, the ratio of anode current density to total current density was about 8.56 % so the efficiency was higher than traditional structure with oxide-poly composition. The reason was similar to triode structure with oxide-nitride-poly composition. From the simulations of electrostatic

potential in Figure 3-18, one of the reasons was that the electrostatic potential near the gate electrode was getting sparse and the distribution of electrostatic potential was also changed resulting from acceding a nitride insulting layer above the poly-Si layer. Consequently, it would cause more electrons to pass through the gate holes and collect by the anode hence make the raise of efficiency. The other reason was due to adding a nitride insulting layer upon the poly-Si layer, some electrons above the poly gate could be blocked from emitting to the gate electrode. Obviously, it would make the decline of gate leakage and the increase of efficiency. As compared with oxide-nitride-poly structure, the efficiency of oxide-poly-nitride structure was lower than 4 %.

However, for the triode structure with oxide-nitride-poly composition, because of adding a nitride insulting layer between oxide and poly, so it would reduce the domination of gate electrode to CNT emitters which could result in the decline of gate controllability (16.03 mA/cm^2), defined emission gate current density (Jg) and emission anode current density (Ja) added together. For the oxide-poly-nitride structure, the gate controllability (63.58 mA/cm^2) was similar to oxide-poly device (66.01 mA/cm^2) due to the nitride insulting layer was adding above the poly-Si layer. Therefore, the gate controllability of oxide-poly-nitride structure was much greater than oxide-nitride-poly structure. Besides, oxide-poly-nitride structure got a larger emission anode current density (5.44 mA/cm^2) than oxide-nitride-poly structure (2.01 mA/cm^2) at gate voltage and anode voltage of 100 V and 1000 V, respectively. Table 3-1 showed the summarized field emission properties of triode-type CNT emitters with different structures. Figure 3-17 revealed the emission anode current density versus anode voltage under different gate bias and no significant increase of emission anode current density was discovered as the anode voltage exceeded 200 V which represented that the field emission current was dominated by the gate voltage.

3.4 Conclusions

To reduce the driving voltage of diode-type CNT emitters, triode-type CNT emitters were proposed and characterized. However, the traditional triode structure (oxide-poly) had a serious problem, namely, efficiency was too low. In this experiment, the efficiency of traditional triode structure was only about 1~2 %, that is to say, nearly 99 % of the energy would be wasted and it could make the increase of power consumption. In order to overcome this question, the traditional triode structure adding a nitride insulting layer was introduced. After putting a nitride insulting layer together, the electrostatic potential near the gate electrode was getting sparse and the distribution of electrostatic potential was also changed. It would make more electrons to pass through the gate holes and collect by the anode hence cause the raise of efficiency. According to the simulations, the electrostatic potential below the gate electrode was much denser than above the gate electrode and it proved the majority of leakage was produced below the gate electrode. Therefore, the nitride insulting layer added below the poly-gate could prevent more electrons than added above the poly-gate. From the Table 3-1, the efficiency of oxide-nitride-poly structure was about 12.54 % which was larger than the efficiency of oxide-poly-nitride structure (8.56 %), so these results agreed with simulations. However, the gate controllability of oxide-nitride-poly would decline due to adding a nitride insulting layer between oxide and poly. Therefore, oxide-nitride-poly structure got a smaller emission anode current density (2.01 mA/cm^2) than oxide-poly-nitride structure (5.44 mA/cm^2) at gate voltage and anode voltage of 100 V and 1000 V, respectively. Although the efficiency of oxide-poly-nitride structure was not higher than oxide-nitride-poly structure, the emission anode current density was more than twice. In order to estimate the impact on the increase distance between the gate and CNTs after adding a nitride layer, the distance between the gate and CNTs was calculated accurately. The gaps between the gate and CNTs were 2.746 μm, 2.816 μm, and 2.746 μm which were corresponded to oxide-poly structure, oxide-nitride-poly structure, and oxide-poly-nitride structure, respectively. The

emission gate current density (Jg) and emission anode current density (Ja) were measured as a function of gate electric field (Eg) with the anode voltage kept at 1000 V as depicted in Figure 3-19(a) and 3-19(b), respectively. However, the result was not much difference than before which without calculating the impact on the increase distance between the gate and CNTs after adding a nitride layer. As a consequence, better emission properties offered the promising future of the CNTs field emission triode with oxide-poly-nitride structure for vacuum microelectronic applications and flat panel displays.

Chapter 4

Conclusions and Future Prospects

4.1 Conclusions

CNTs synthesized by thermal CVD were used as field emitters for the nano-sized feature, which could provide large aspect ratio to increase the field enhancement factor (β). However, density of CNTs synthesized by thermal CVD was still very high and thus reduced the β value due to the screening effects. Therefore, the density distribution of CNTs was one of the critical parameters dominating the field emission characteristics of CNTs. To effectively enhance the field emission properties, three novel methods including two thin Ti capping layer processes and a co-deposition of Ti and Fe process were introduced. For the thin Ti capping layer without pre-treatment, the optimum thickness of thin Ti capping layer was found out to be 2 nm but the best field emission properties were not good enough. For the thin Ti capping layer with pre-treatment, the optimum thickness of thin Ti capping layer was 2 nm. The turn-on field of 2.5 V/μm and threshold field of 3.5 V/μm were obtained at the turn-on current of 10 μA/cm^2 and the threshold current of 10 mA/cm^2. The field emission current density improved from 11.12 mA/cm^2 to 97.6 mA/cm^2 at the electric field of 6 V/μm with the thickness of the Ti capping layer increased from 0 nm to 2 nm. In this case, the density of CNTs was about 2.8x10^7 emitter/cm^2 which roughly matched the simulation results for suppression the screening effects. Nevertheless, the uniformity was still very poor. For the co-deposition of Fe and Ti, the optimum weight percentage of Ti was 36 %. The turn-on field of 3.059 V/μm and threshold field of 4.706 V/μm were obtained at the turn-on current of 10 μA/cm^2 and the threshold current of 10 mA/cm^2. The field emission current density improved from 8 mA/cm^2 to 26.96 mA/cm^2 at the electric field of 5.5 V/μm with the weight percentage of Ti increased from 0 % to 36 % nm. Although the field emission properties had not been

superior to method of Ti capping layer with pre-treatment, the uniformity would be improved obviously from the luminescent images. As a consequence, the co-deposition of Fe and Ti was a very promising method to suppress the screening effects and improve the uniformity of CNTs so it had a great potential for commercial application.

To reduce the driving voltage of diode-type CNT emitters, triode-type CNT emitters were proposed and characterized. However, the traditional triode structure (oxide-poly) had a serious problem of low efficiency (1.23 %). After adding a nitride insulting layer below the poly-Si layer, the electrostatic potential near the gate electrode was getting sparse and the distribution of electrostatic potential was also changed. Besides, some electrons below the gate electrode could be blocked by the nitride insulting layer. Consequently, it would make more electrons to pass through the gate holes and collect by the anode hence cause the increase of efficiency. Although, the efficiency of oxide-nitride-poly structure was increased to 12.54 %, the gate controllability would decline rapidly due to adding a nitride insulting layer between oxide and poly. If the nitride insulting layer acceded above the poly-Si layer, the efficiency was also increased to 8.56 % due to the same reasons. Furthermore, it could keep the gate controllability and get a larger emission anode current density (5.44 mA/cm^2) at the gate voltage and anode voltage of 100 V and 1000 V, respectively. The triode structure with oxide-poly-nitride composition showed the feasibility and promising technique for future applications in FED.

4.2 Future Prospects

For controlling the density of CNTs, the further research topics are proposed as follows:

(1) Try other capping materials (such as Mo and Al) and analyze the field emission properties.

(2) For co-deposition with Fe and Ti, the uniformity is improved but the field emission properties are not good enough. Therefore, look for the best conditions for co-deposition

technique.

(3) Try other buffer layer materials (such as Mo, Al, Cr, Ta, TaN, and TiN) and expect to improve the adhesion between CNTs and substrate.

(4) The growth temperature of CNTs should be reduced to below 500 ℃ and hope for large-area application.

(5) In-situ vacuum sealed field emission diode of CNTs for high frequency circuit applications.

For the triode structures of CNTs, the further research topics are proposed as follows:

(1) Establish the simulations of oxide-poly-nitride structure and tune the conditions (such as the gate-to-emitter gap and the length of emitters) to obtain the best field emission properties.

(2) Combine with the optimal parameters of density control to obtain the better characteristics.

(3) Try the triode structure with oxide-nitride-poly-nitride composition.

(4) The focus gate with oxide-poly-nitride-poly composition can be applied to improve the emission characteristics.

(5) In-situ vacuum sealed field emission triode of CNTs for high frequency circuit applications.
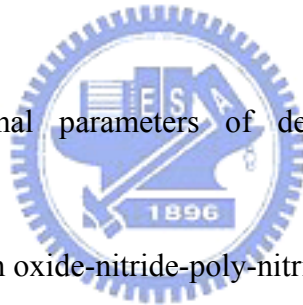
Table 1-1

Comparison between vacuum microelectronics and solid-state electronics.

Items	Solid State Microelectronics	Vacuum Microelectronics
Current Density	$10^4 - 10^5$ (A/cm^2)	similar
Turn-on Voltage	0.1 – 0.7 V	5 – 300 V
Structure	solid/solid interface	solid/vacuum interface
Electron Transport	in solid	in vacuum
Electron Velocity	3×10^7 (cm/sec)	3×10^{10} (cm/sec)
Flicker Noise	due to interface	due to emission
Thermal & Short Noise	comparable	comparable
Electron Energy	< 0.3 eV	a few to 1000 eV
Cut-off Frequency	< 20 GHz (Si) & 100 GHz (GaAs)	< 100 – 1000 GHz
Power	small – medium	medium – large
Radiation Hardness	poor	excellent
Temperature Effect	-30 – 50 °C	< 500 °C
Fabrication & Materials	well established (Si) & fairly well (GaAs)	not well established

Table 2-1

(a) The densities of CNTs with different thicknesses of thin Ti capping layer listed in this table.

(b) The turn-on field, threshold field, and emission current density at 6 V/μm of CNTs with different thicknesses of the thin Ti capping layer

(a)

Ti Capping Layer Thickness (nm)	Density of CNTs (emitter/cm^2)
0 nm	8.8x10^8 (emitter/cm^2)
0.5 nm	3.6x10^8 (emitter/cm^2)
1 nm	1.2x10^8 (emitter/cm^2)
2 nm	8x10^6 (emitter/cm^2)
4 nm	3x10^6 (emitter/cm^2)

(b)

Ti Capping Layer Thickness	Turn-on field at 10 μA/cm^2	Threshold field at 10 mA/cm^2	Emission current density at 6 V/μm
0 nm	4.071 V/μm	N. A.	1.568 mA/cm^2
0.5 nm	3.681 V/μm	N. A.	2.420 mA/cm^2
1 nm	3.667 V/μm	N. A.	3.384 mA/cm^2
2 nm	3.545 V/μm	5.909 V/μm	10.200 mA/cm^2
4 nm	4.000 V/μm	N. A.	0.972 mA/cm^2

Table 2-2

(a) The densities of CNTs with different thicknesses of thin Ti capping layer listed in this table.

(b) The turn-on field, threshold field, and emission current density at 6 V/μm of CNTs with different thicknesses of the thin Ti capping layer

(a)

Ti Capping Layer Thickness (nm)	Density of CNTs (emitter/cm^2)
0 nm	2.8x10^8 (emitter/cm^2)
1 nm	1x10^8 (emitter/cm^2)
2 nm	2.8x10^7 (emitter/cm^2)
4 nm	1.2x10^7 (emitter/cm^2)
10 nm	9x10^6 (emitter/cm^2)
20 nm	< 1x10^6 (emitter/cm^2)

(b)

Ti Capping Layer Thickness	Turn-on field at 10 μA/cm^2	Threshold field at 10 mA/cm^2	Emission current density at 6 V/μm
0 nm	3.786 V/μm	5.857 V/μm	11.12 mA/cm^2
1 nm	2.571 V/μm	5.179 V/μm	15.68 mA/cm^2
2 nm	2.500 V/μm	3.500 V/μm	97.60 mA/cm^2
4 nm	2.107 V/μm	4.571 V/μm	20.48 mA/cm^2
10 nm	3.850 V/μm	5.950 V/μm	10.20 mA/cm^2
20 nm	4.714 V/μm	N. A.	0.20 mA/cm^2

Table 2-3

(a) The densities of CNTs with different weight percentages of Ti listed in this table.

(b) The turn-on field, threshold field, and emission current density at 5.5 V/μ m of CNTs with different weight percentages of Ti

(a)

Weight Percentage of Ti (%)	Density of CNTs (emitter/cm^2)
0 %	8x10^9 (emitter/cm^2)
36 %	2x10^9 (emitter/cm^2)
53 %	5x10^8 (emitter/cm^2)
70 %	2x10^8 (emitter/cm^2)
85 %	8x10^6 (emitter/cm^2)

(b)

Weight Percentage of Ti	Turn-on field at 10 μ A/cm^2	Threshold field at 10 mA/cm^2	Emission current density at 5.5 V/μ m
0 %	3.679 V/μ m	5.75 V/μ m	8.00 mA/cm^2
36 %	3.059 V/μ m	4.706 V/μ m	26.96 mA/cm^2
53 %	3.000 V/μ m	~ 6 V/μ m	8.24 mA/cm^2
70 %	4.594 V/μ m	N. A.	0.30 mA/cm^2
85 %	5.531 V/μ m	N. A.	< 0.01 mA/cm^2

Table 3-1

Show the summarized field emission properties of triode-type CNT emitters with different structures.
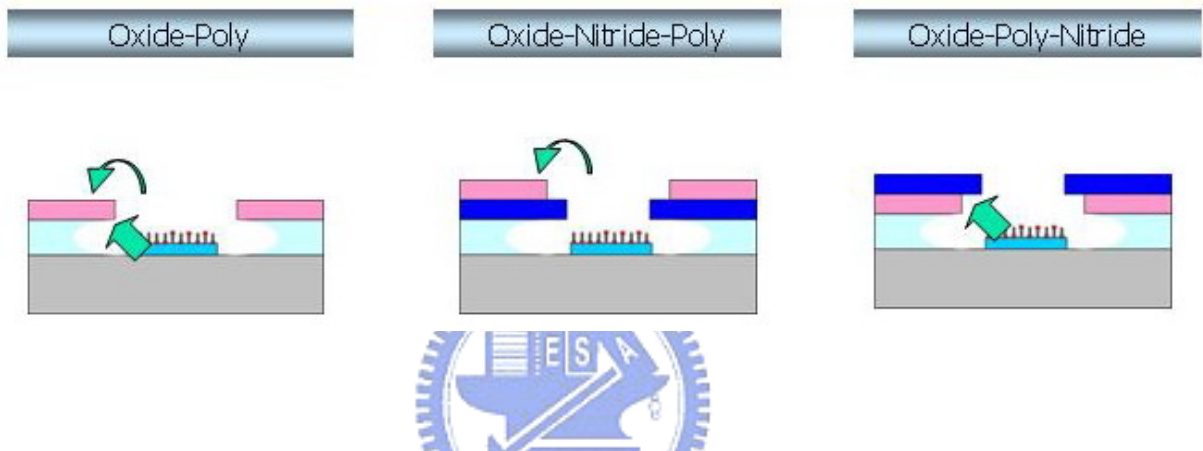
		Oxide-Poly	Oxide-Nitride-Poly	Oxide-Poly-Nitride
Va = 1000 V **Vg = 100 V**	**Ja**	**0.81 mA/cm^2**	**2.01 mA/cm^2**	**5.44 mA/cm^2**
	Jg	**65.20 mA/cm^2**	**14.02 mA/cm^2**	**58.14 mA/cm^2**
	Eff.	**1.23 %**	**12.54 %**	**8.56 %**
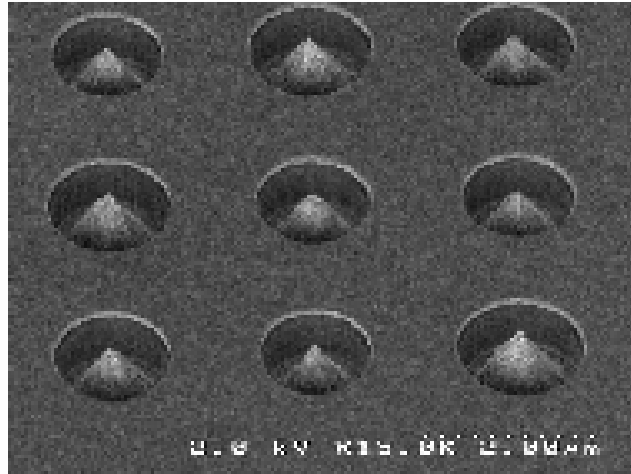
(a)
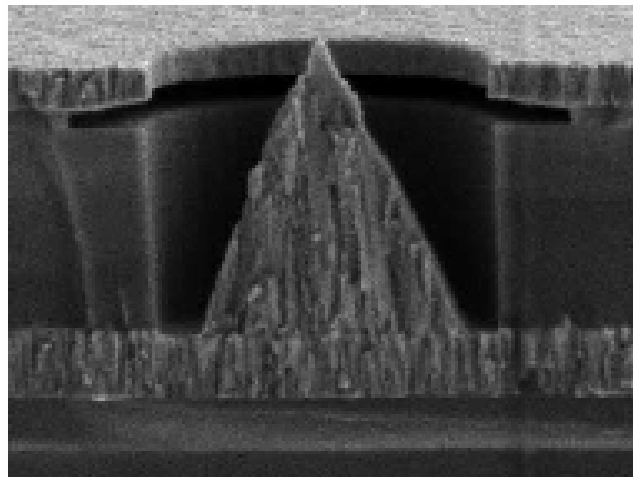
(b)

Figure 1-1 The SEM micrograph of (a) Spindt type triodes array, (b) Spindt type field

emission triode
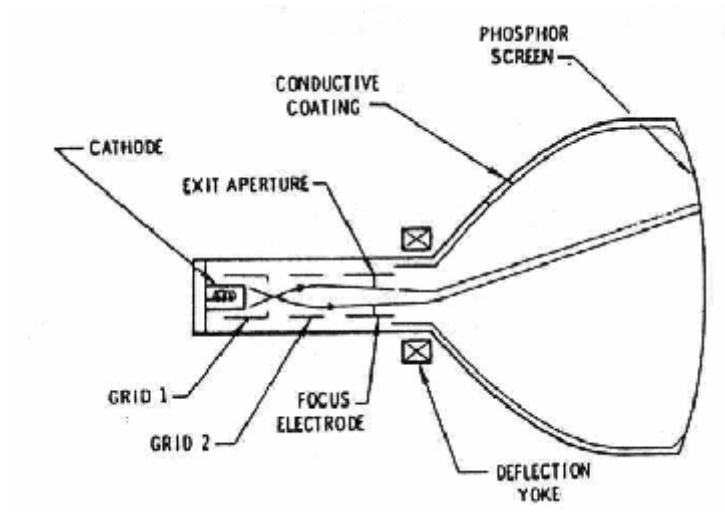
(a)
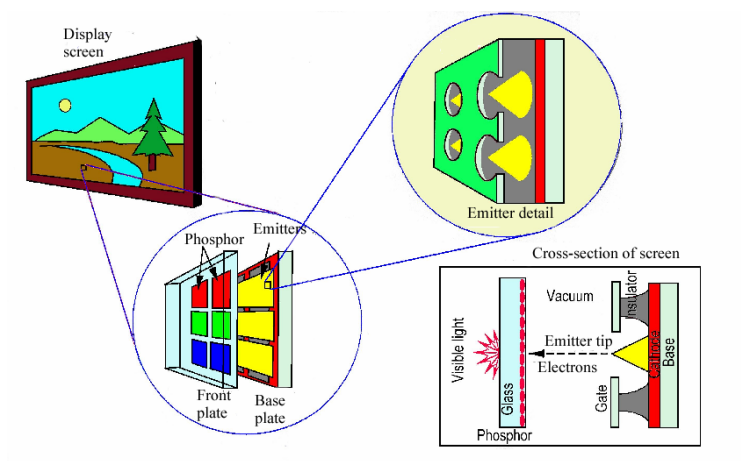
(b)

Figure 1-2 The schematic diagram of (a) conventional CRT, (b) FED.
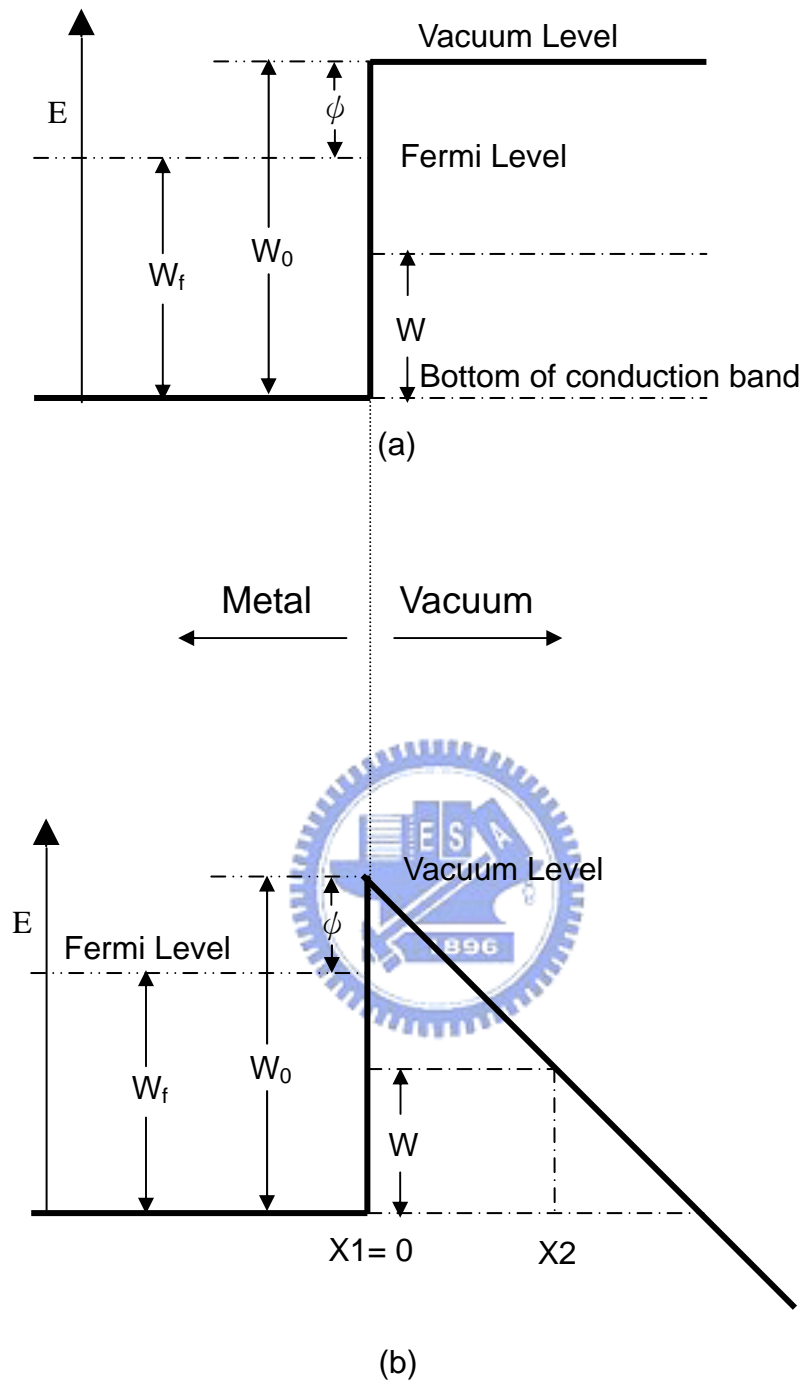
Figure 1-3 Energy diagrams of vacuum-metal boundary:

(a) without external electric field;

(b) with an external electric field.

(a)

(b)

(c)

(d)

Figure 1-4 The FED products based on Spindt type field emitters, (a) motorola 5.6" color FED, (b) Pixtech 5.6" color FED, (c) Futaba 7" color FED and (d) Sony/Candescent 13.2" color FED.
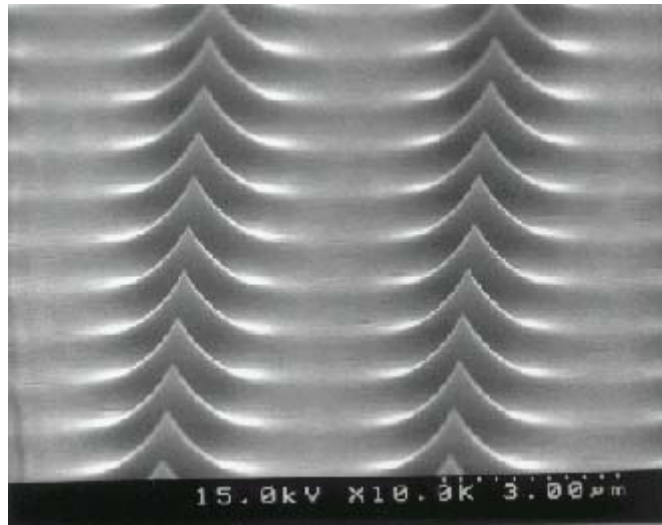
(a)
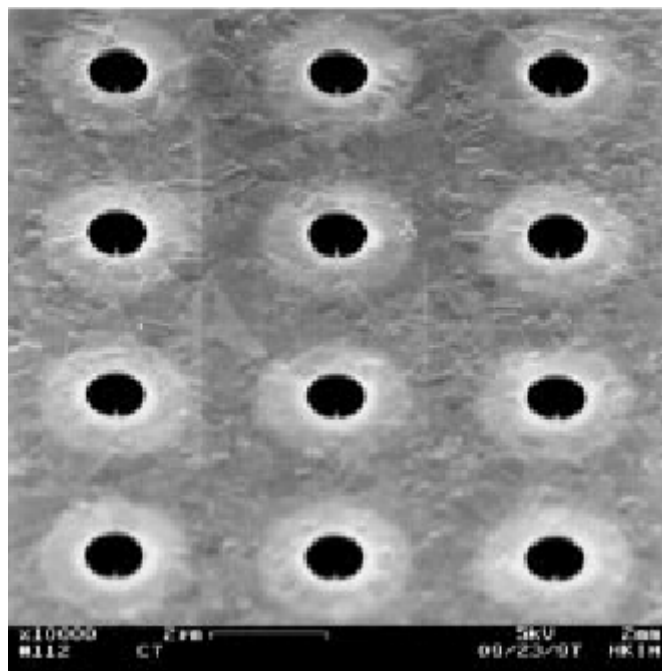
(b)

Figure 1-5 (a) Si tip formed by isotropic etching and (b) Si tip field emission triodes array

formed by CMP
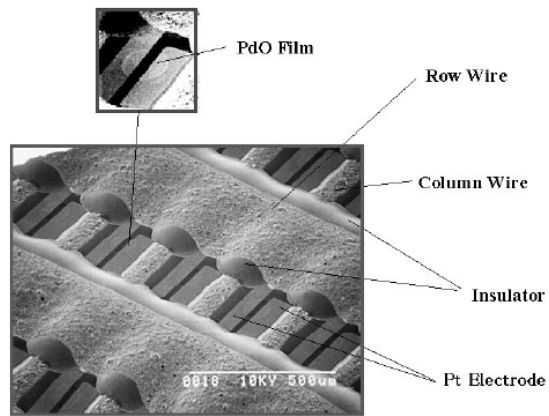
(a)
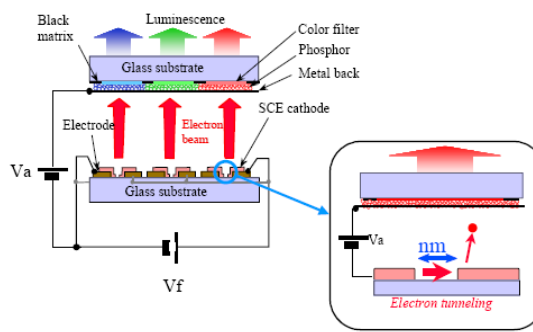
(b)

(c)

Figure 1-6 (a) SEM image of SCE cathode array (b) structure of SED (c) a 36-inch prototype

of surface conduction electron emitter display
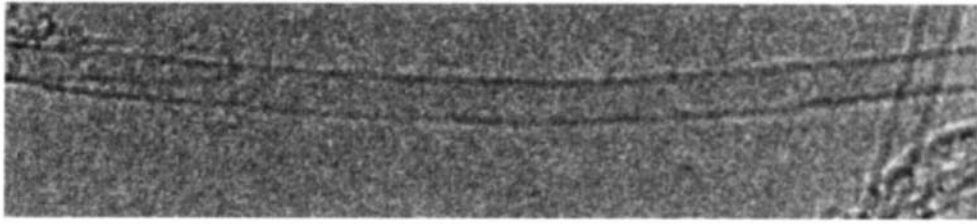
(a)
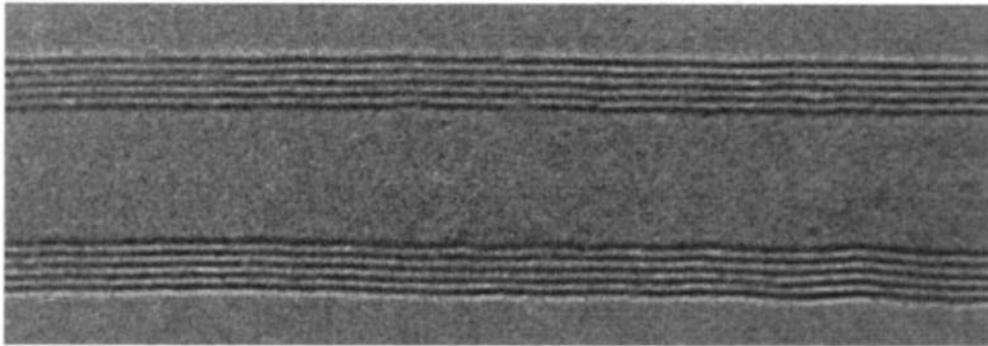
(b)

Figure 1-7 High-resolution transmission electron microscopy images of (a) single-walled nanotubes (SWNTs) and (b) multiwalled nanotubes (MWNTs). Every layer in the image (fringe) corresponds to the edges of each cylinder in the nanotube assembly.
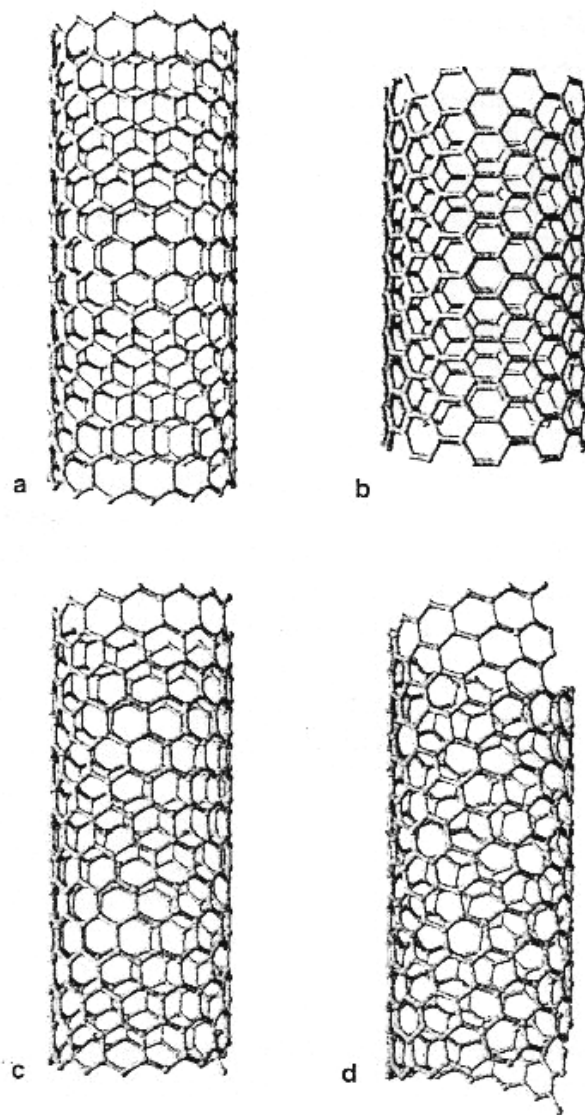
Figure 1-8 Molecular models of single-walled nanotubes with different helicities: (a) zig-zag arrangement; (b) armchair configuration; (c) and (d) two different helicities.
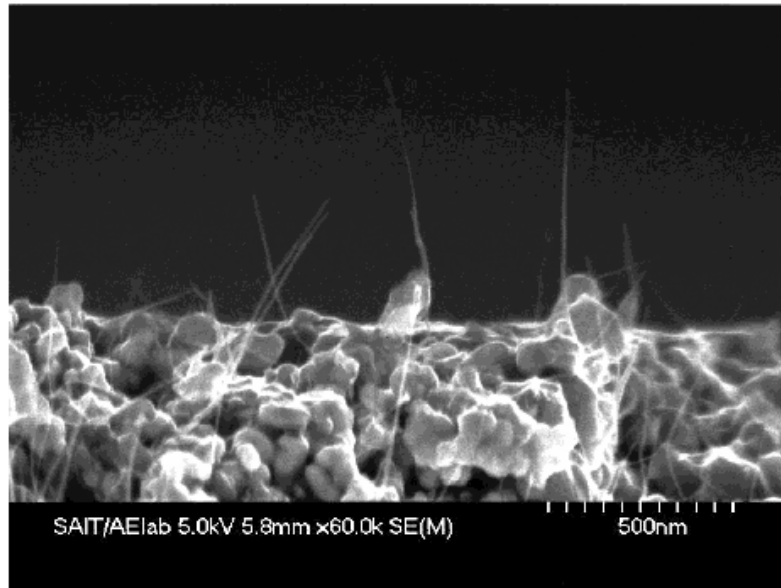
(a)

(b)

(c)

Figure 1-9 (a) SEM image of CNT cathode from Samsung's FED, (b) a 4.5-inch FED from

Samsung, the emitting image of fully sealed SWNT-FED at color mode with red,

green, and blue phosphor columns, and (c) a prototype of 5" CNT flat panel

display by Samsung
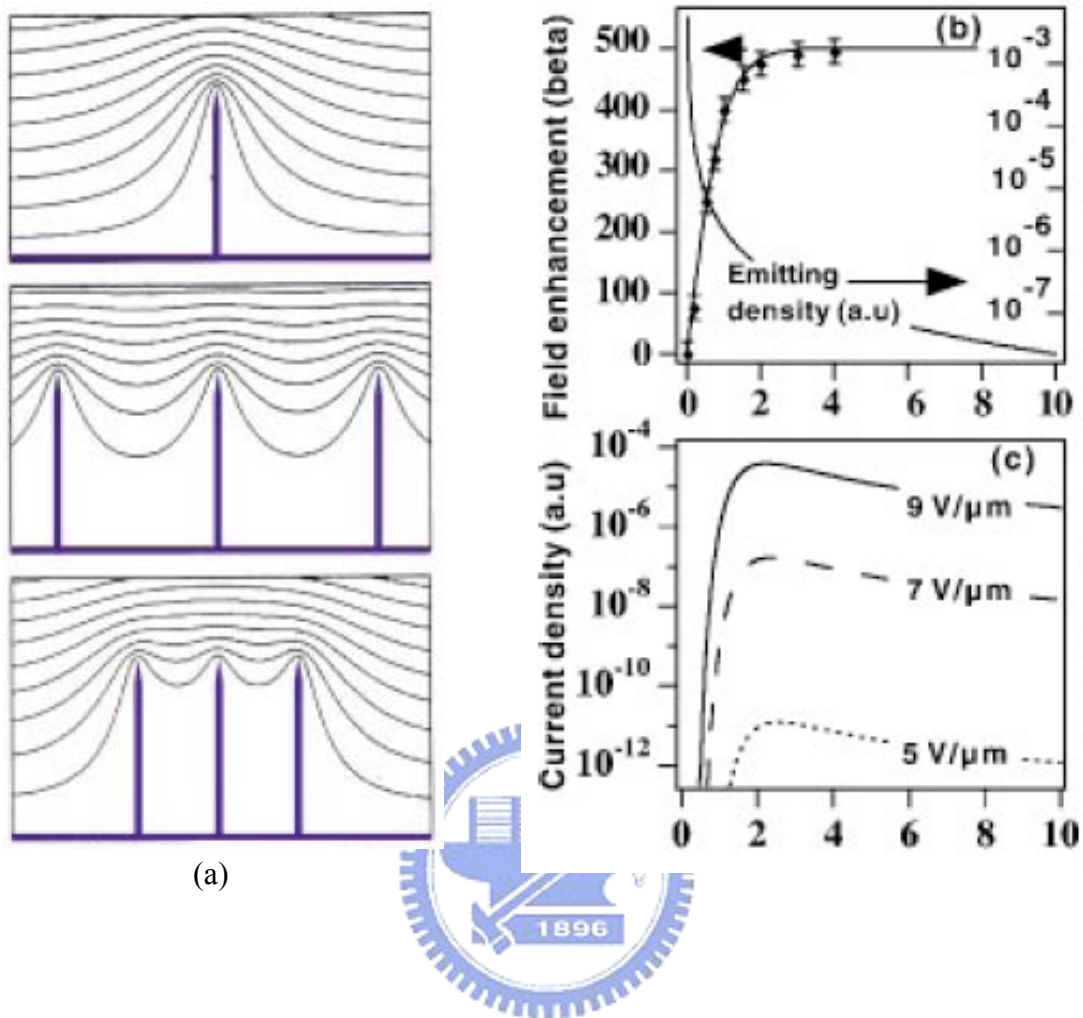
Figure 2-1 (a) Simulation of the equipotential lines of the electrostatic field for tubes of 1 μm height and 2 nm radius, for distances between tubes of 4, 1, and 0.5 μm; along with the corresponding changes of the field enhancement factor β and emitter density (b), and current density (c) as a function of the distance.

(Ref. Appl. Phys. Lett. 76 (2000) 2071)
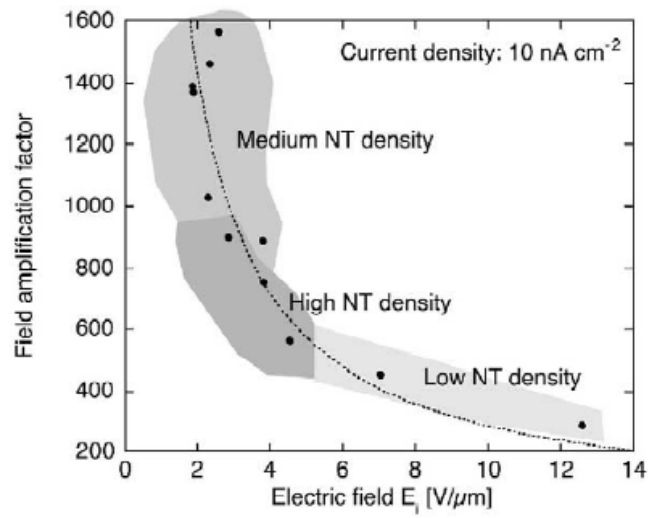
(a)
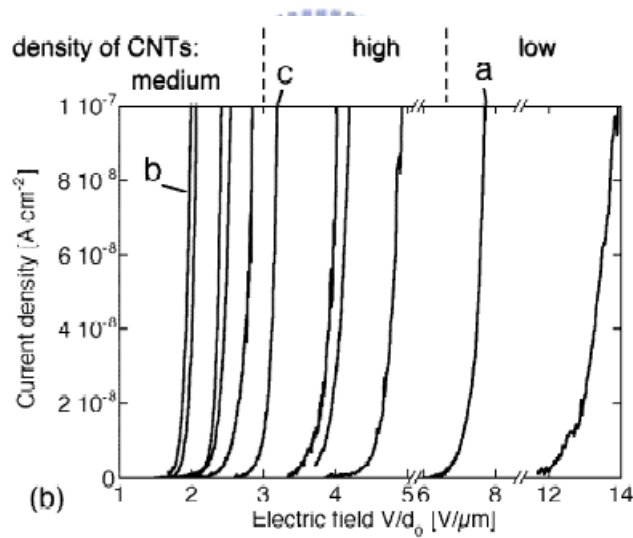
Figure 2-2 (a) Field amplification factor β as a function of the onset field after training, Ei, for the films obtained by CVD with different catalyst concentrations. (b) Low current field emission characteristics of the 11 samples after training.

(Ref. Carbon 40 (2002) 1715)

Exposure

Mask

Photoresistance

Silicon Substrate

(a)

Fe Catalyst (5 nm)
Ti Buffer Layer (50 nm)

(b)

Lift-off

(c)

A Thin Ti Capping Layer

(d)

Growth

(e)
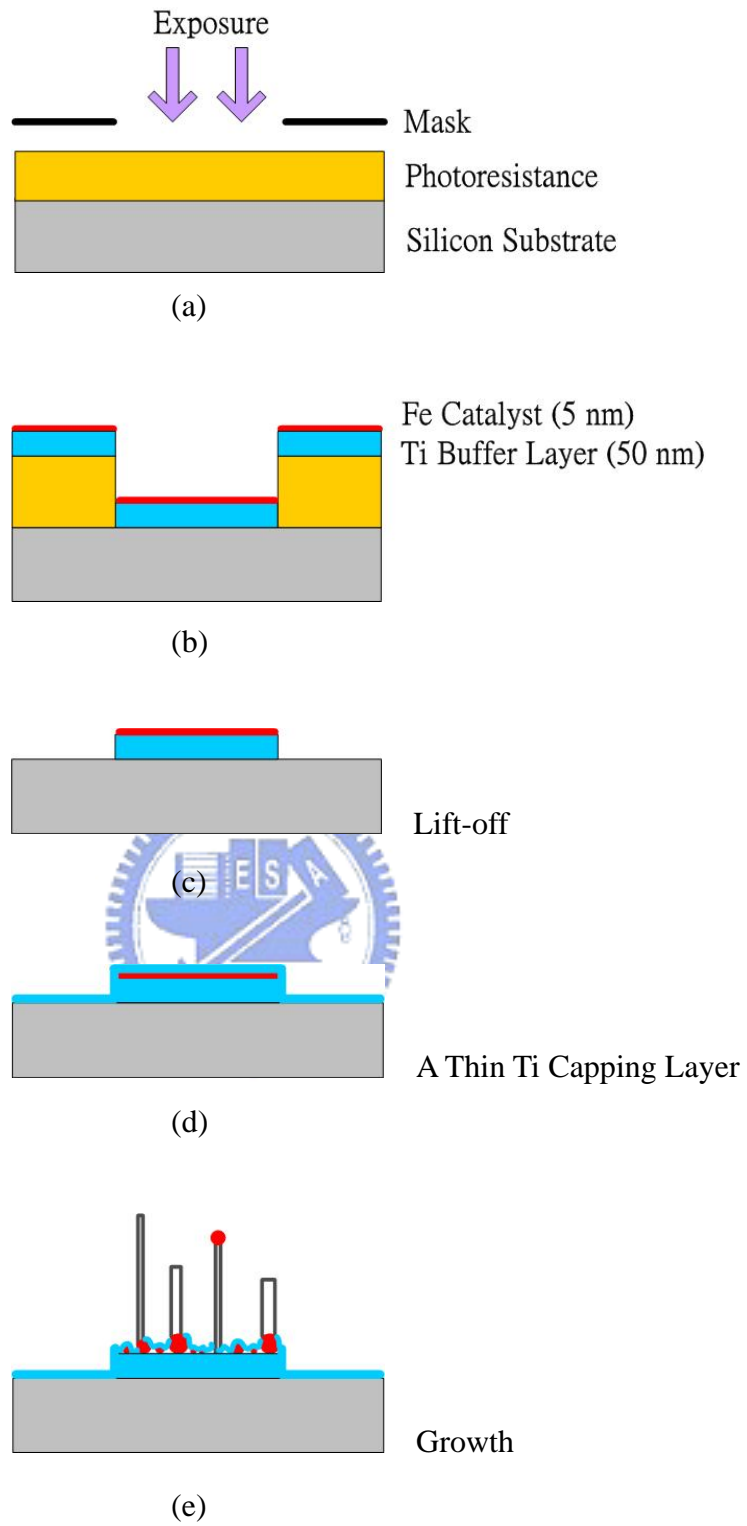
Figure 2-3 Experimental procedures of patterned CNTs synthesized by thermal CVD.

(a)

(b)
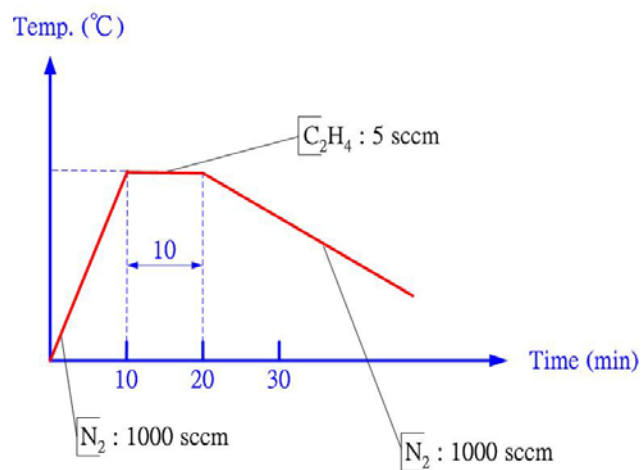
(c)

Figure 2-4 (a) (b) Show photo and schematic pictures of thermal CVD, and (c) the growth condition of CNTs in the thermal CVD.
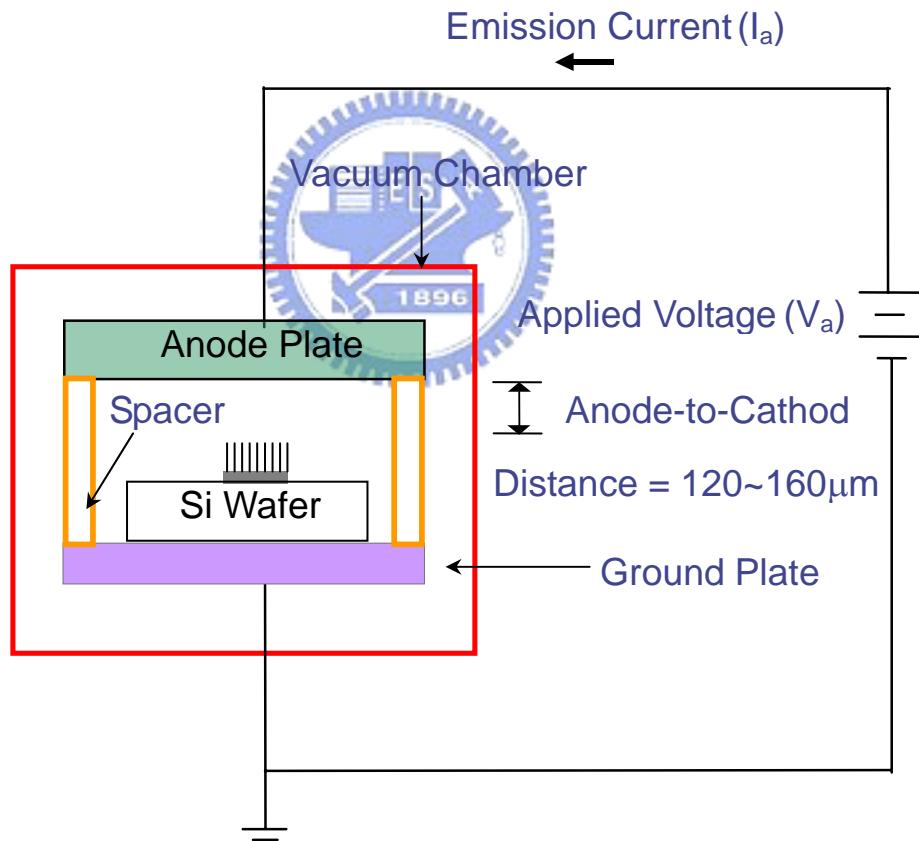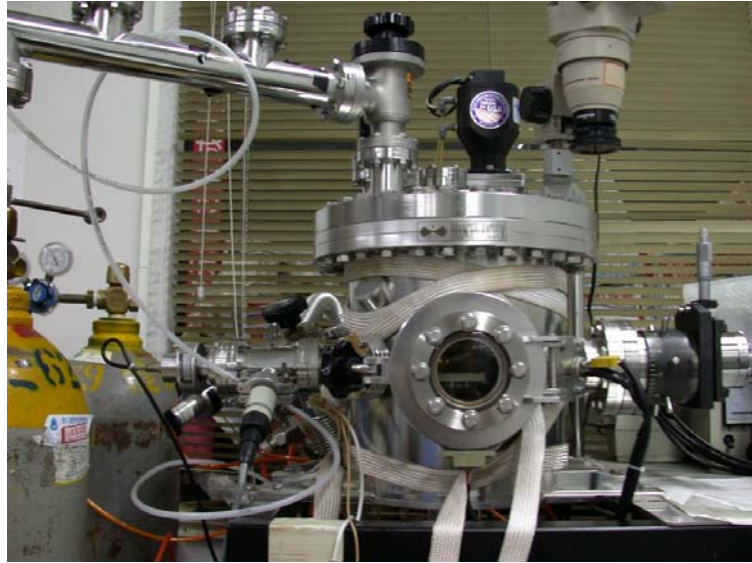
Figure 2-5 Schematic diagram of a high-vacuum system setup for field emission measurement.
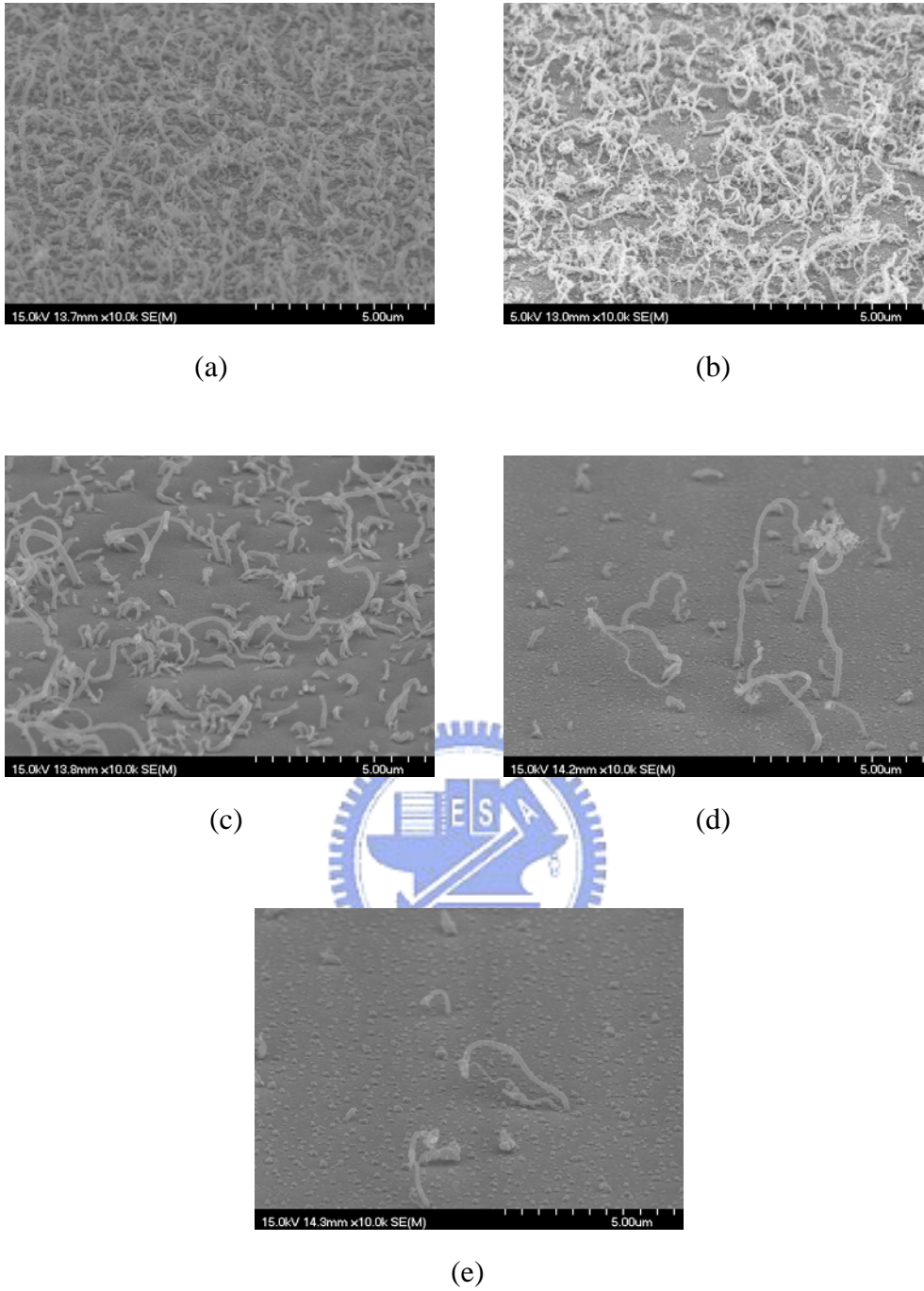
Figure 2-6 The SEM images of CNTs with different thicknesses of the thin Ti capping layer from a 45° viewing angle: (a) 0 nm, (b) 0.5 nm, (c) 1 nm, (d) 2 nm, and (e) 4 nm.

(a)

(b)

(c)

(d)

(e)
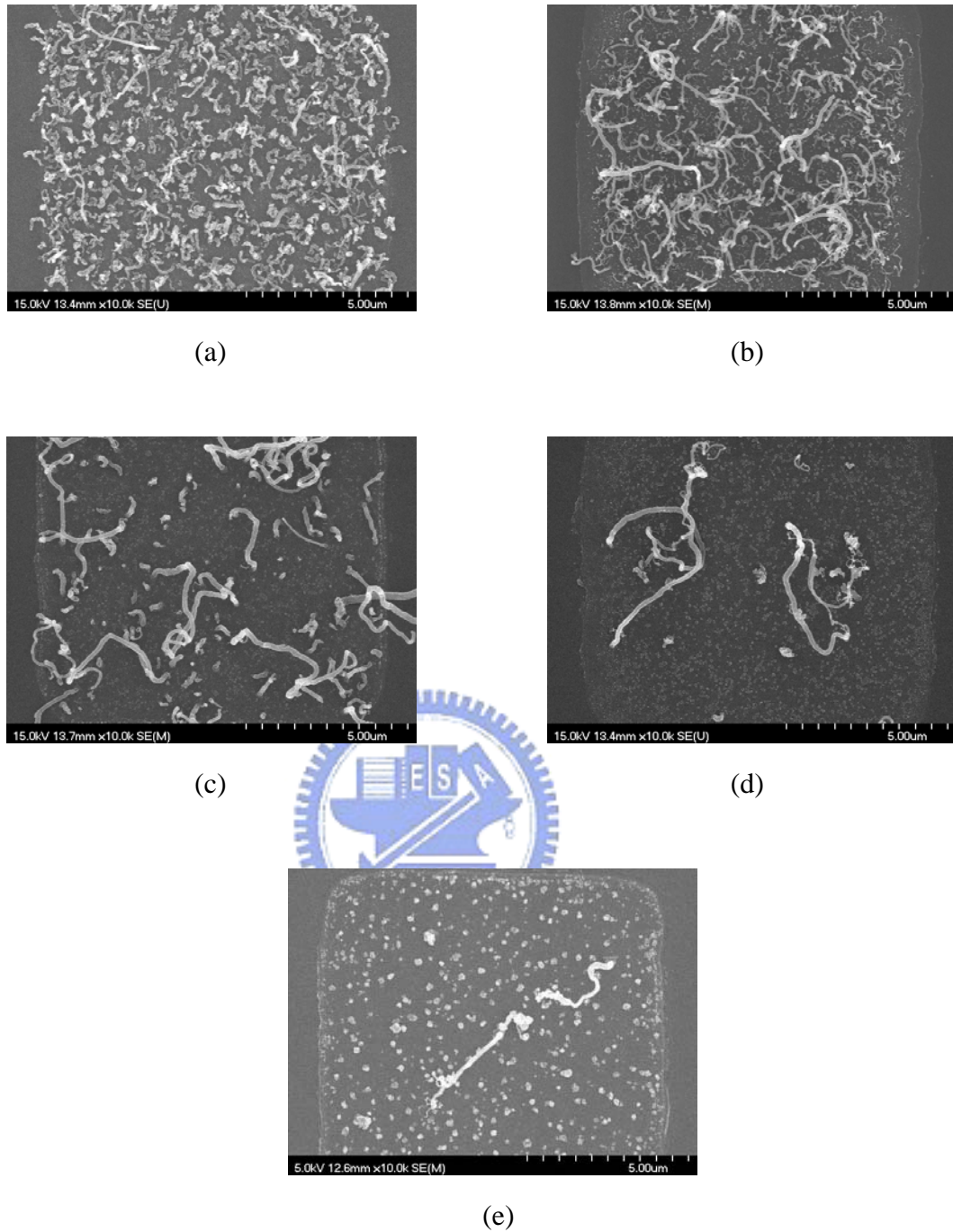
Figure 2-7 The SEM images of CNTs with different thicknesses of the thin Ti capping layer

from the top view: (a) 0 nm, (b) 0.5 nm, (c) 1 nm, (d) 2 nm, and (e) 4 nm.
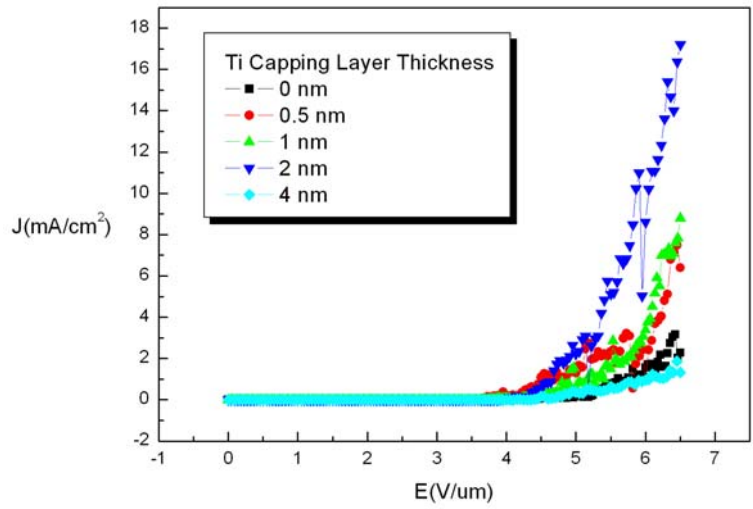
(a)
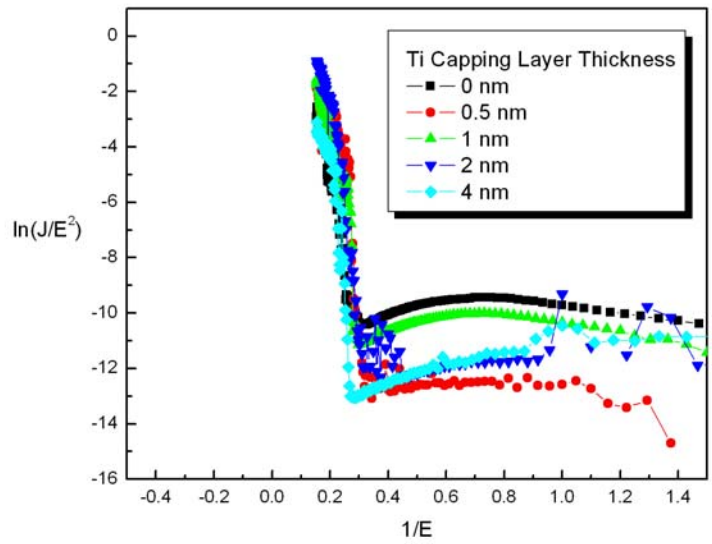
(b)

Figure 2-8 The field emission properties: (a) the relationship between emission current density and electric field (b) the Fowler-Nordheim plot

Exposure

Mask

Photoresistance

Silicon Substrate

(a)

Fe Catalyst (5 nm)
Ti Buffer Layer (50 nm)

(b)

Lift-off

(c)

Pre-treatment

(d)

A Thin Ti Capping Layer

(e)

Growth

(f)
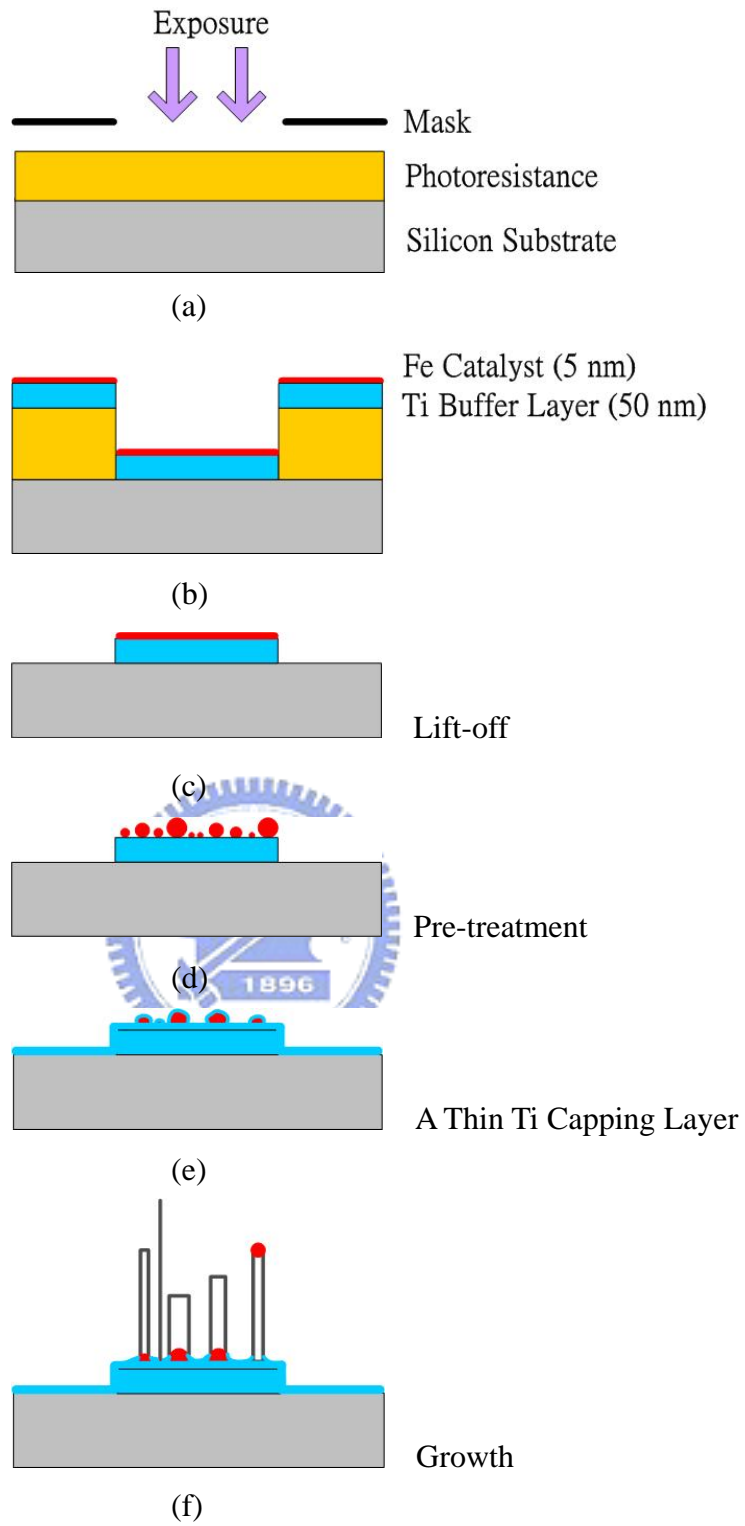
Figure 2-9 Experimental procedures of patterned CNTs synthesized by thermal CVD.

(a)   (b)

(c)   (d)

(e)   (f)
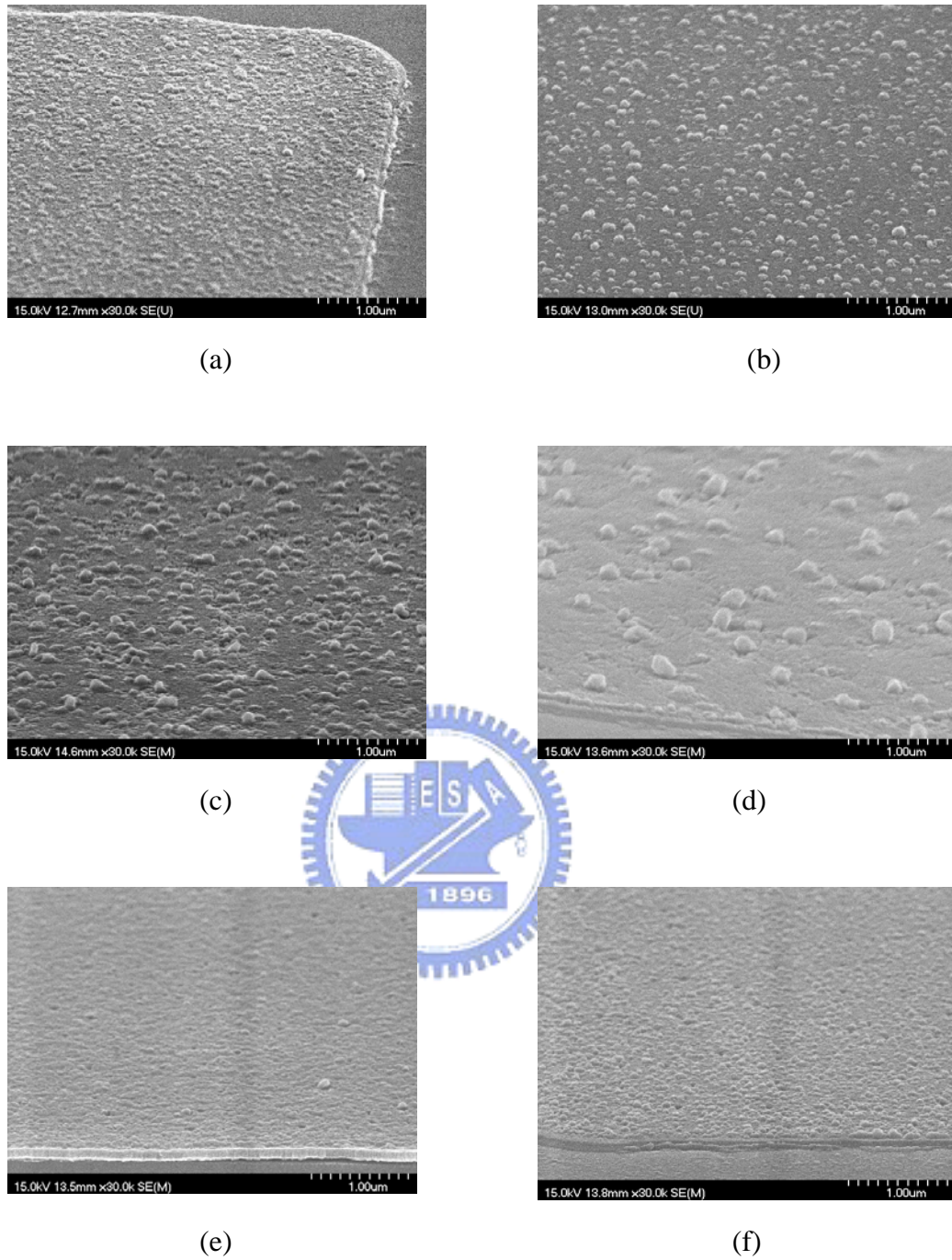
Figure 2-10 The SEM images of pre-treated catalytic nanoparticles with different thicknesses

of the thin Ti capping layer: (a) 0 nm, (b) 1 nm, (c) 2 nm, (d) 4 nm, (e) 10 nm,

and (f) 20 nm.

72

(a)

(b)

(c)

(d)

(e)

(f)
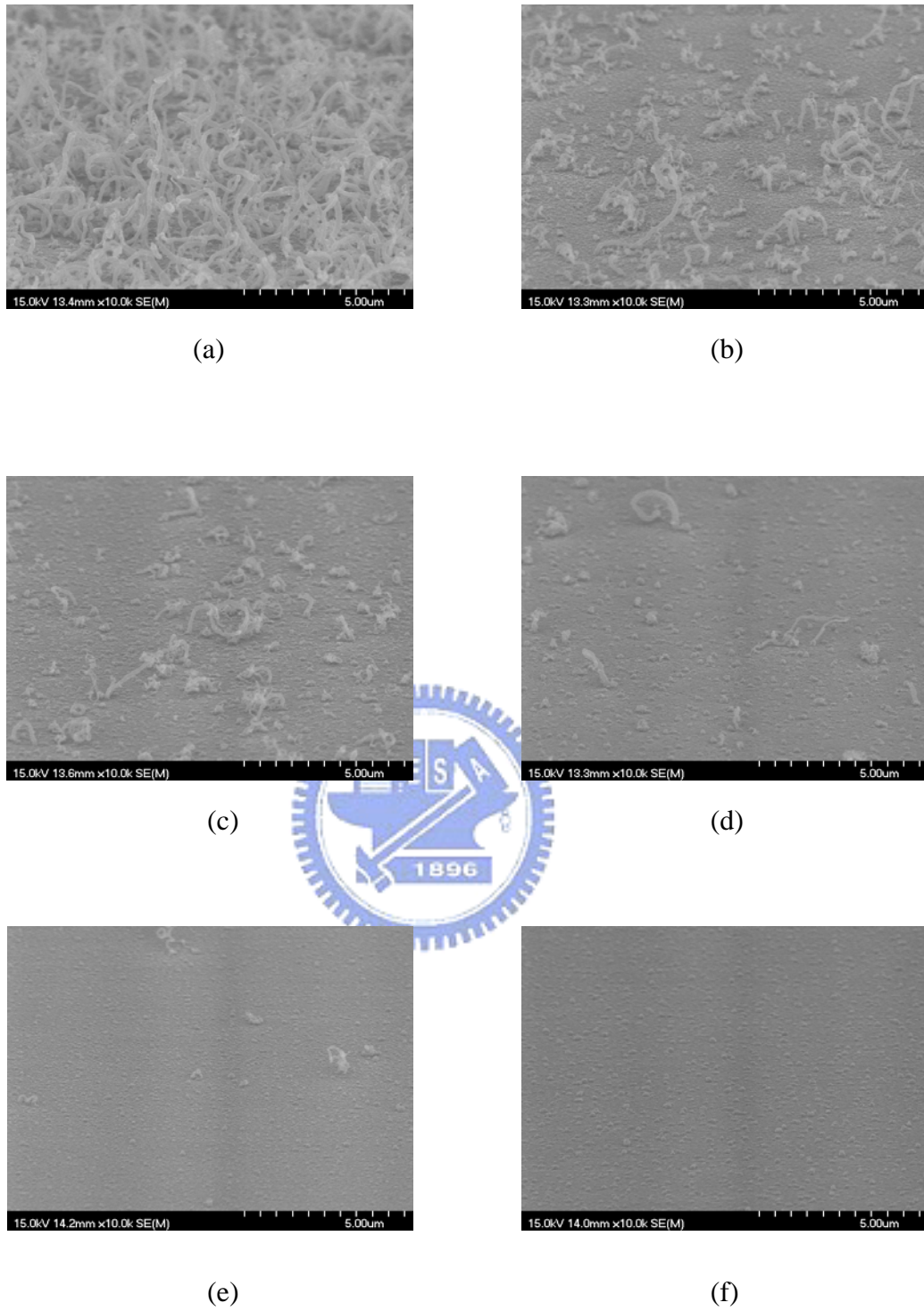
Figure 2-11 The SEM images of CNTs with different thicknesses of the thin Ti capping layer from a 45° viewing angle: (a) 0 nm, (b) 1 nm, (c) 2 nm, (d) 4 nm, (e) 10 nm, and (f) 20 nm.

(a)

(b)

(c)

(d)

(e)

(f)
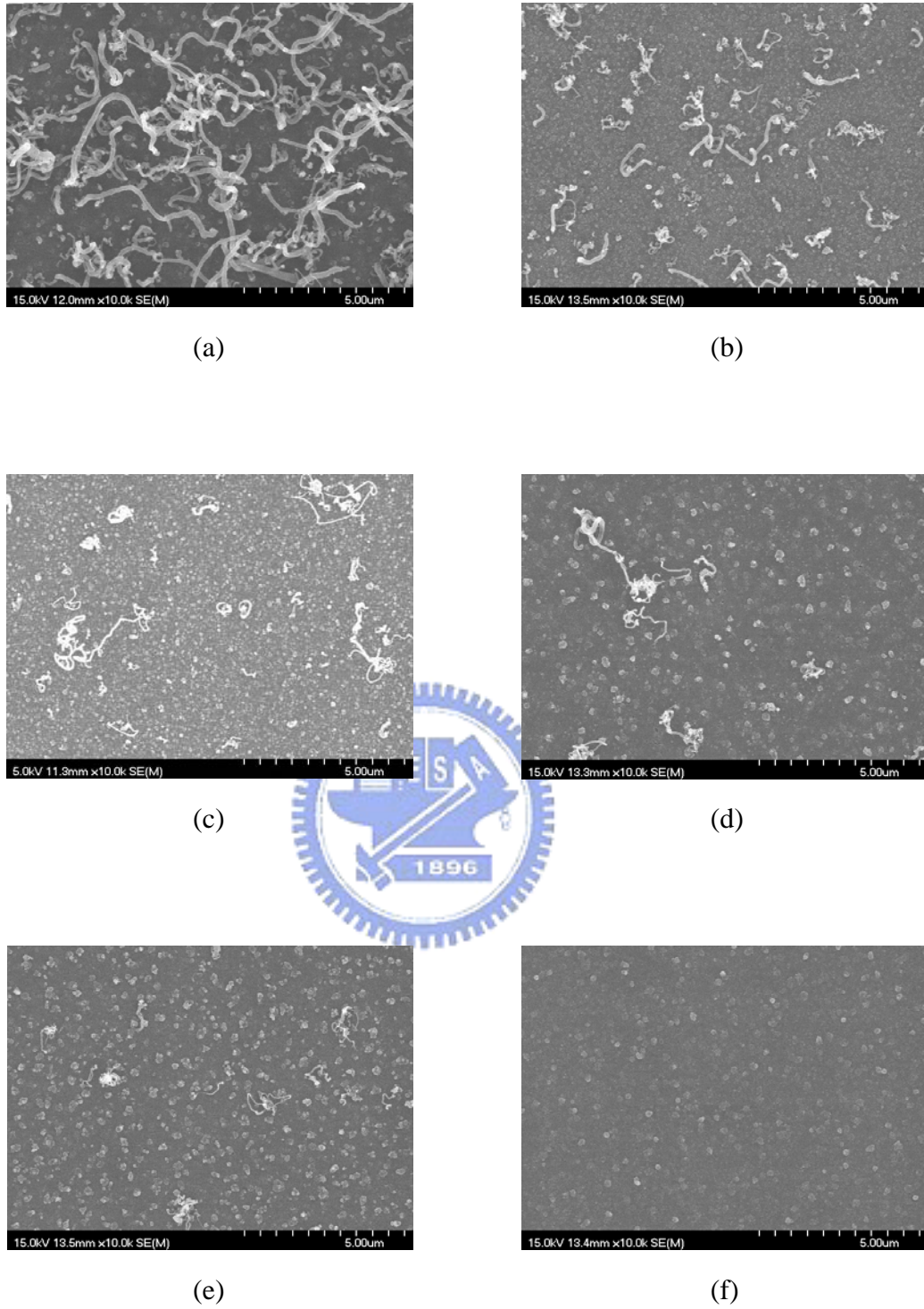
Figure 2-12 The SEM images of CNTs with different thicknesses of the thin Ti capping layer from the top view: (a) 0 nm, (b) 1 nm, (c) 2 nm, (d) 4 nm, (e) 10 nm, and (f) 20 nm.
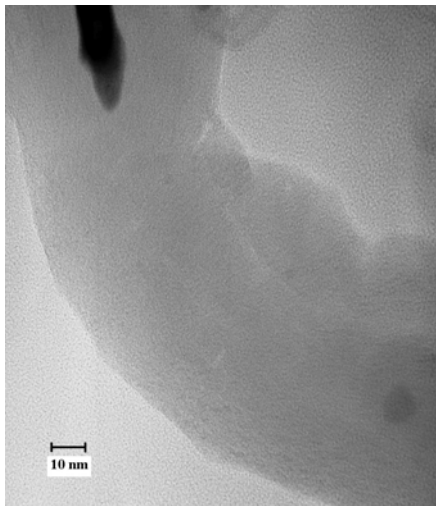
(a)
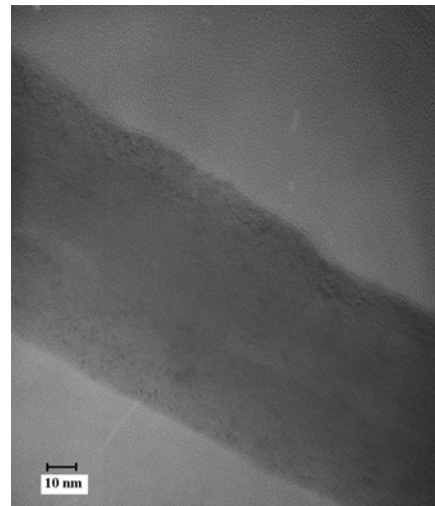
(b)
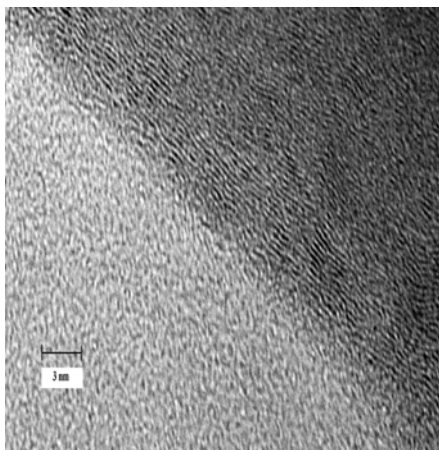
(c)
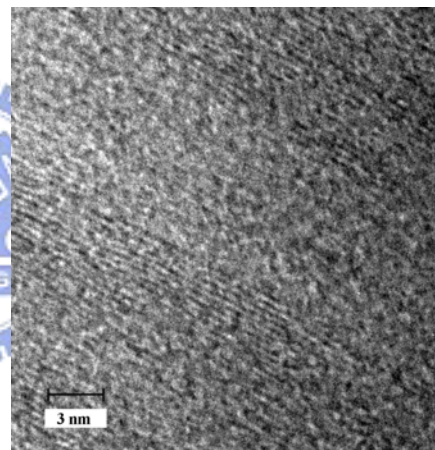
(d)

Figure 2-13 The HRTEM images of CNTs with (a) (b) low magnification images, and (c) (d)

high magnification images of sidewall and intertube, respectively.
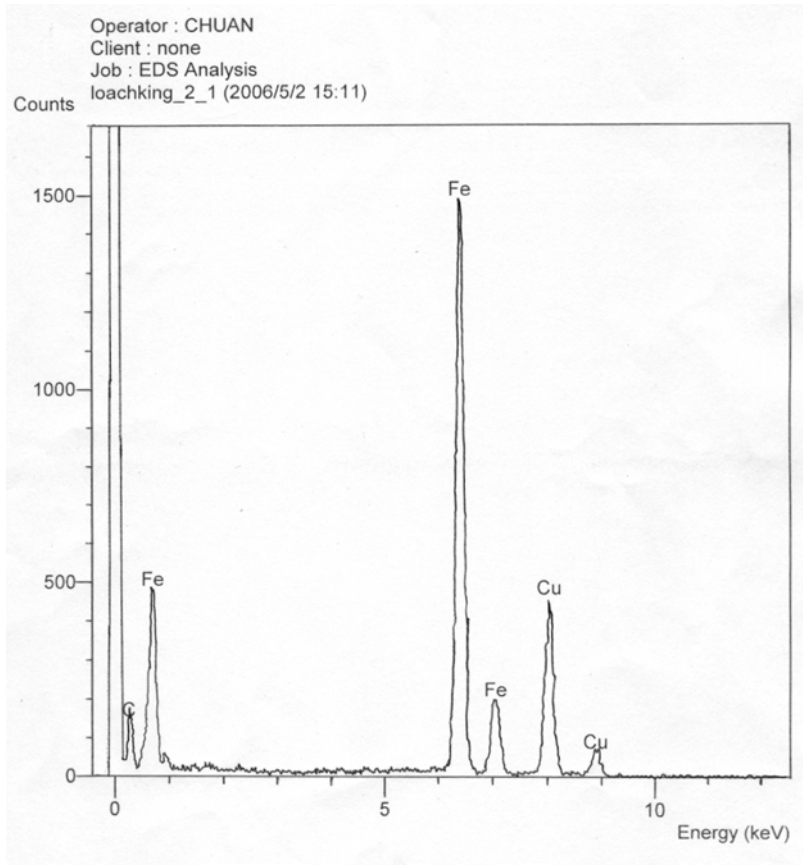
Figure 2-14 The EDS analysis of the catalytic nanoparticle in CNTs
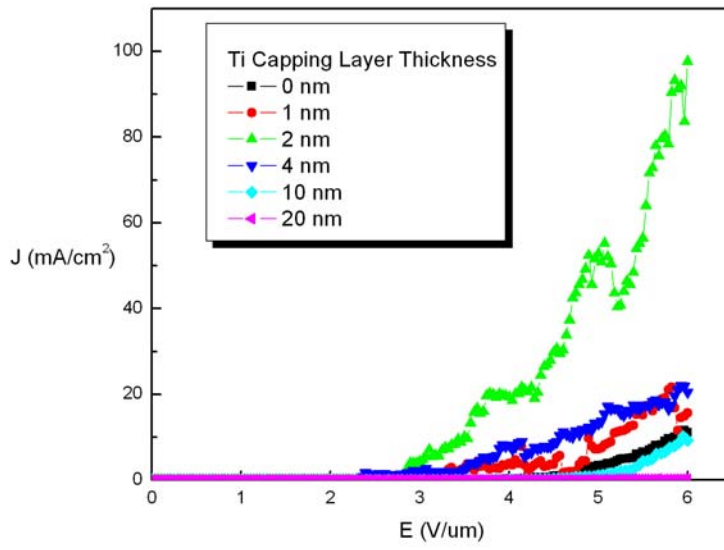
(a)
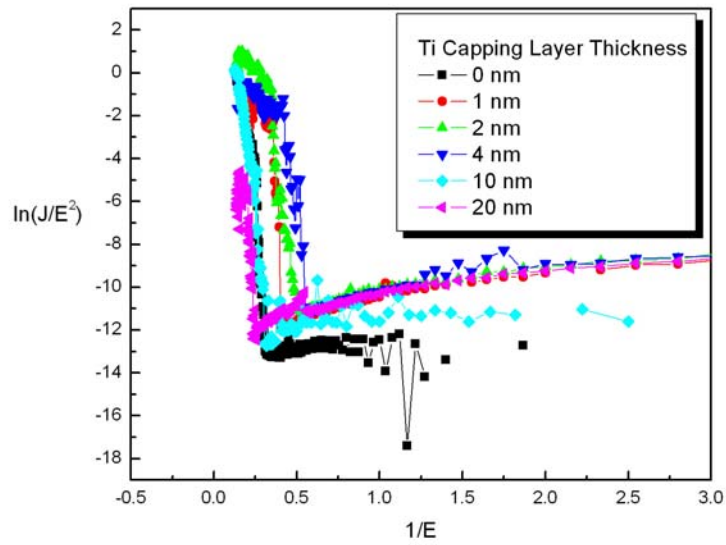
(b)

Figure 2-15 The field emission properties: (a) the relationship between emission current density and electric field (b) the Fowler-Nordheim plot
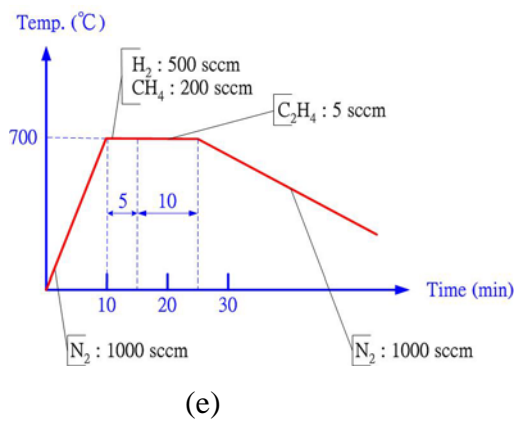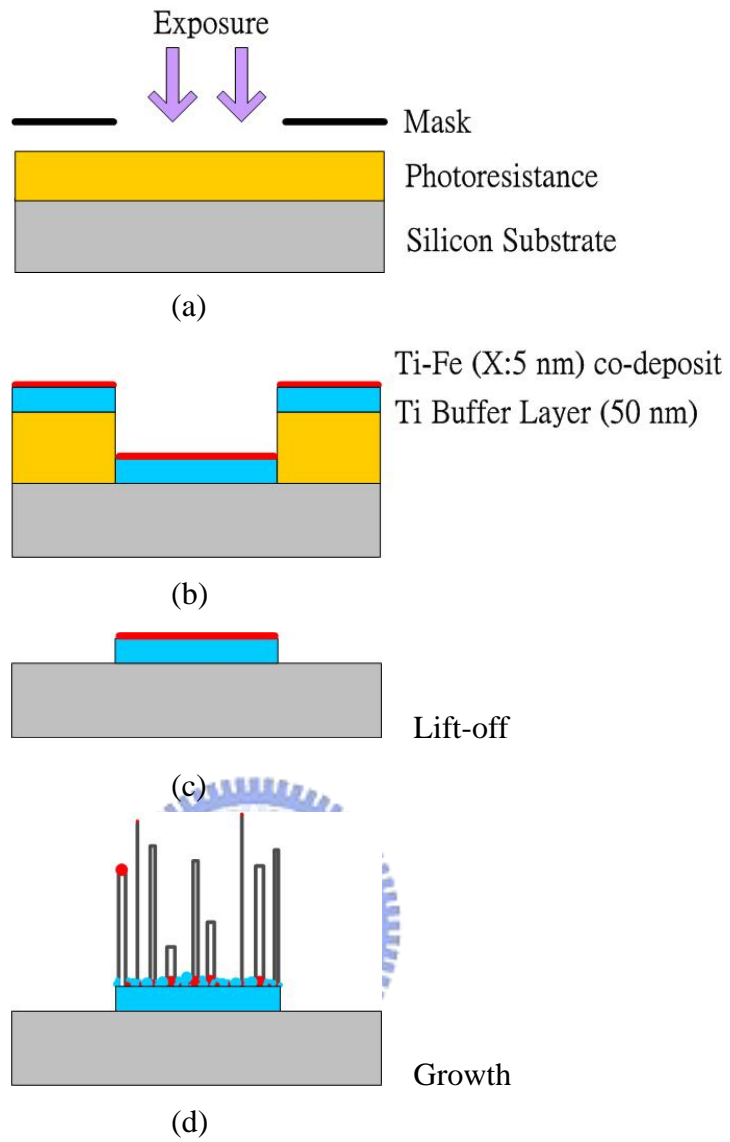
Figure 2-16 Experimental procedures of patterned CNTs synthesized by thermal CVD.

(a)

(b)

(c)

(d)

(e)
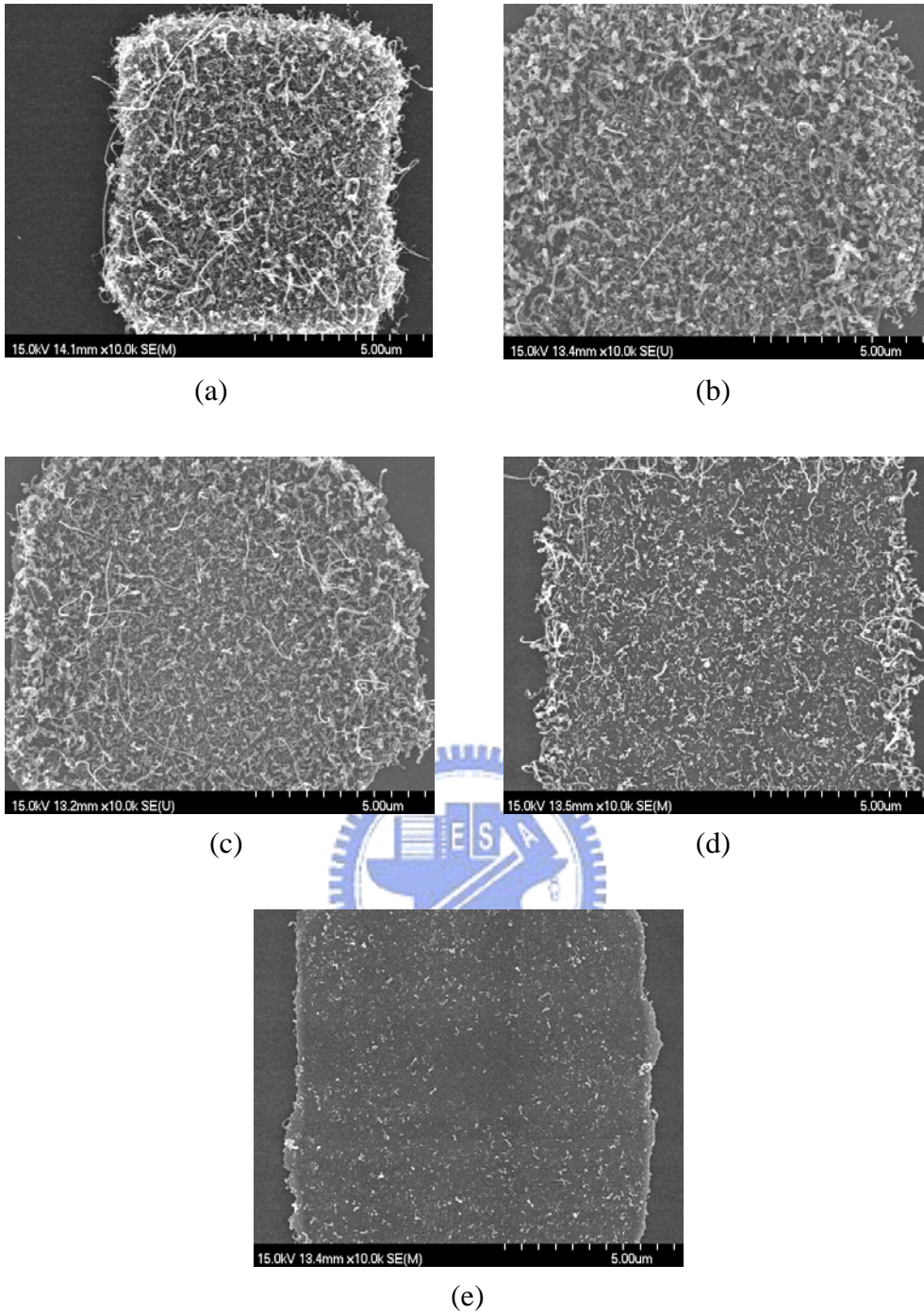
Figure 2-17 The SEM images of CNTs with different weight percentages of Ti from the top

view: (a) 0 %, (b) 36 %, (c) 53 %, (d) 70 %, and (e) 85 %.
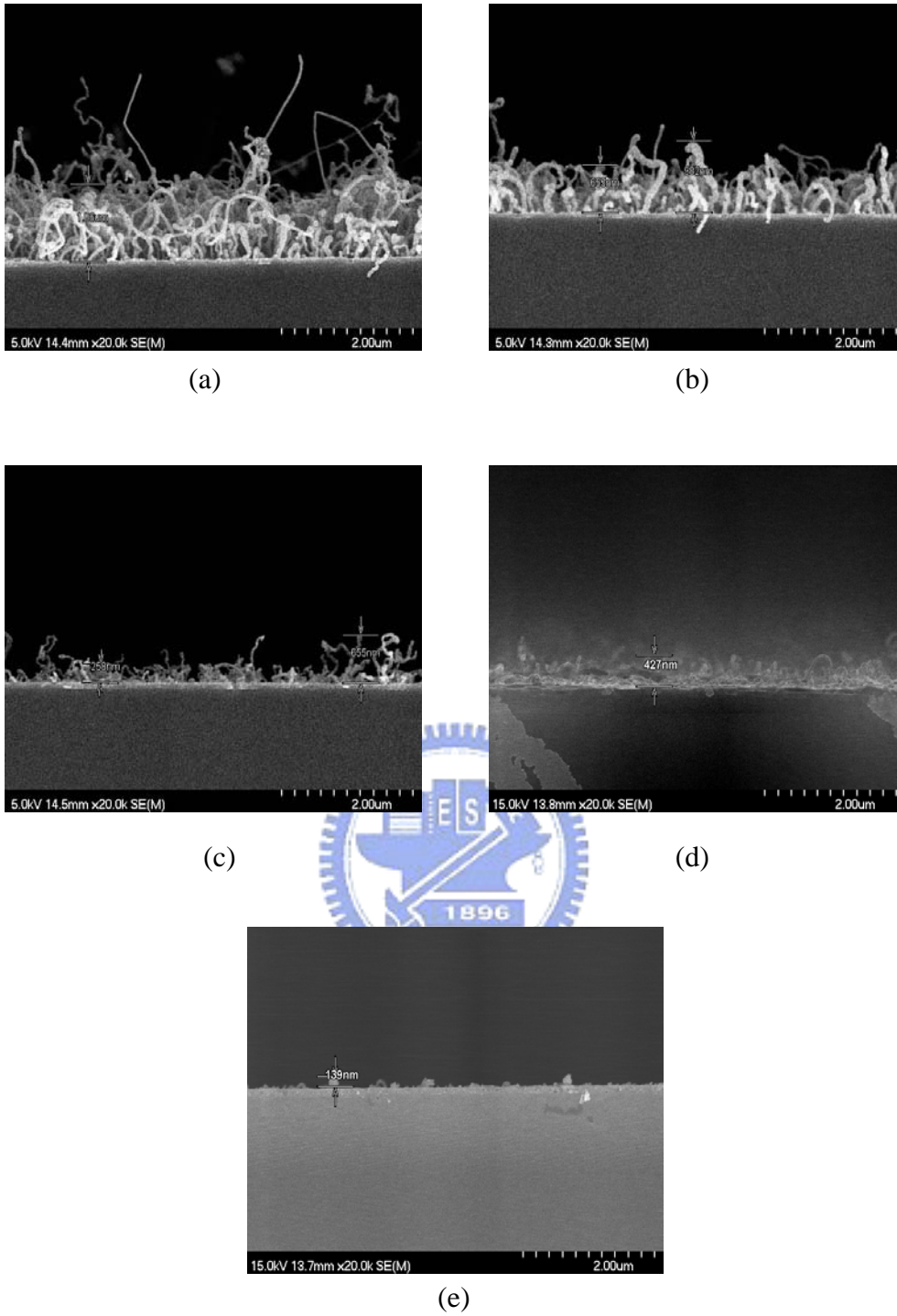
Figure 2-18 The SEM images of CNTs with different weight percentages of Ti from a 90°

viewing angle: (a) 0 %, (b) 36 %, (c) 53 %, (d) 70 %, and (e) 85 %.
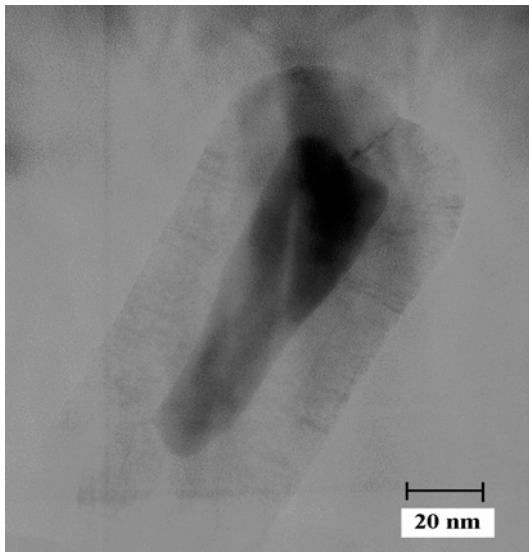
(a)
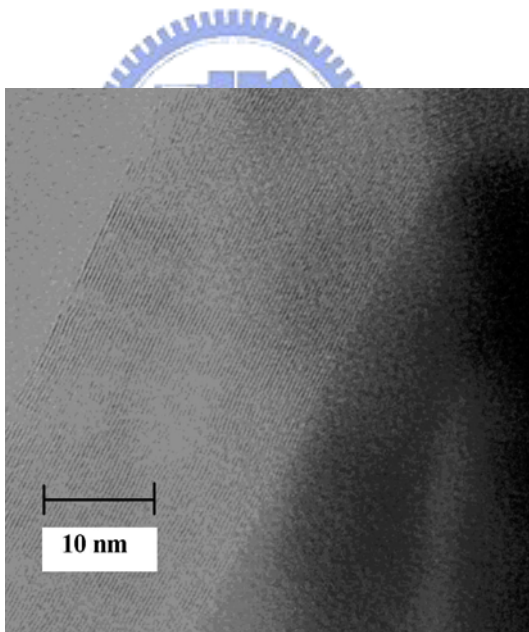
(b)

Figure 2-19 The HRTEM images of CNTs with (a) low magnification images and (b) high magnification images.
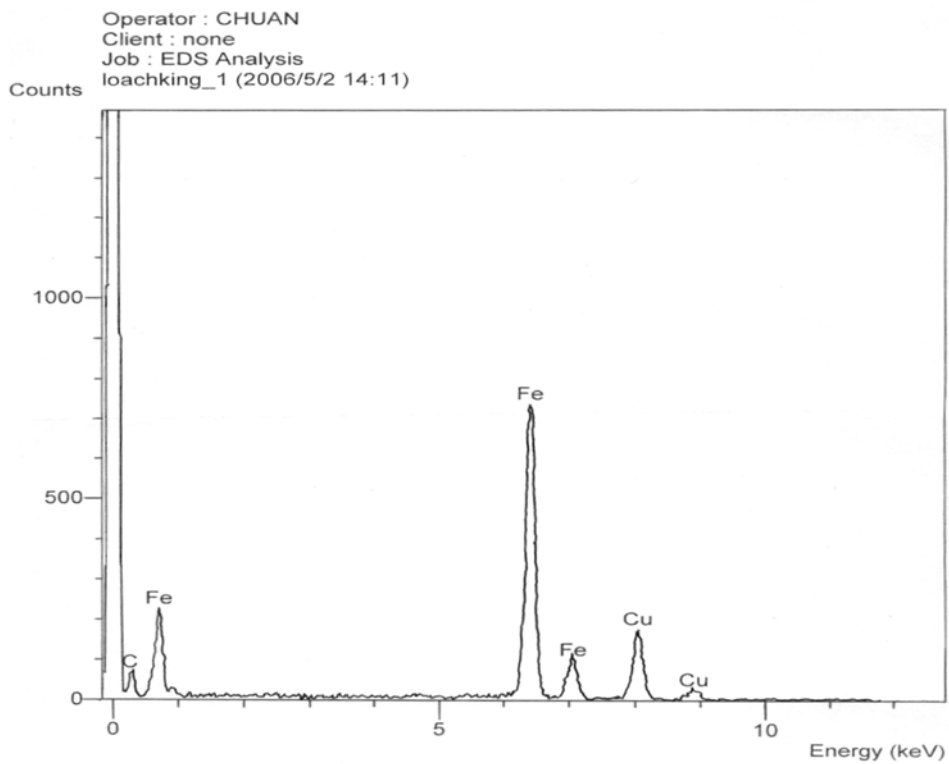
Figure 2-20 The EDS analysis of the catalytic nanoparticle in CNTs
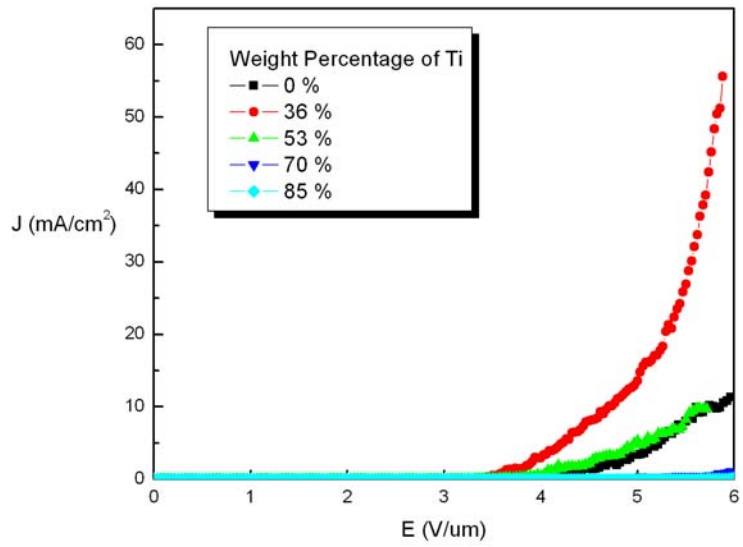
(a)
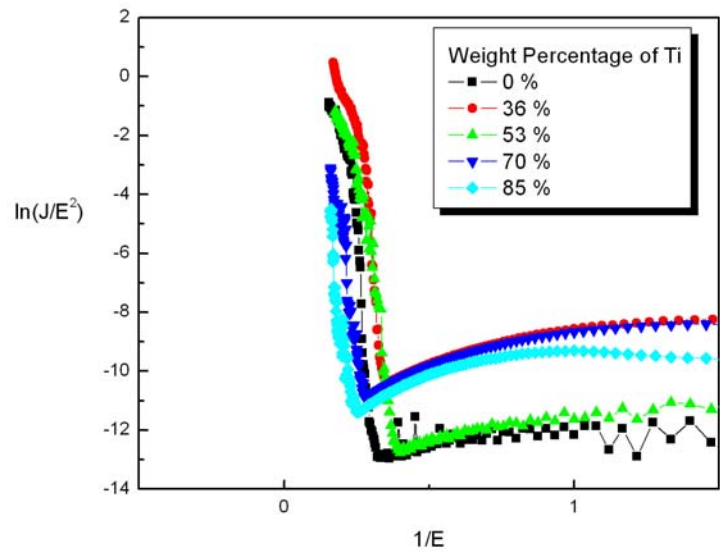
(b)

Figure 2-21 The field emission properties: (a) the relationship between emission current density and electric field (b) the Fowler-Nordheim plot

(a)   (b)   (c)

(d)   (e)   (f)

(g)   (h)   (i)
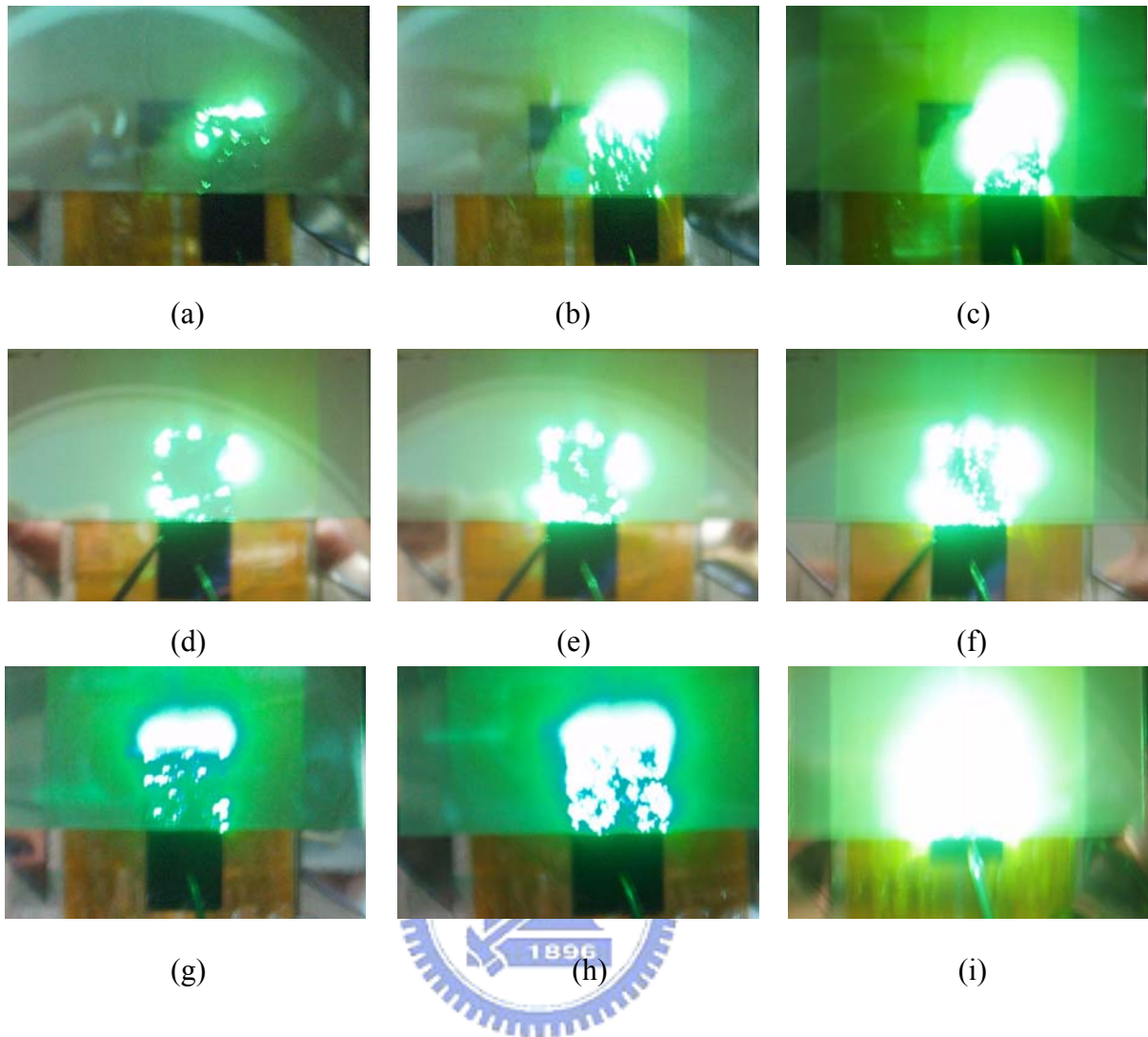
Figure 2-22 The luminescent images on the ITO anode with phosphor coating on it were observed. Samples (a), (b), and (c) showed the Fe/Ti (5 nm/50 nm) film at applied electric field 5, 6, and 7 V/μm, respectively. Samples (d), (e), and (f) showed the Fe/Ti (5 nm/ 50 nm) film and a 2-nm-thick Ti capping layer was deposited after pre-treatment at applied electric field 5, 6, and 7 V/μm, respectively. Samples (g), (h), and (i) showed the weight percentage of Ti was 36 % in the co-deposition of Fe and Ti were deposited on the 50-nm-thick Ti buffer layer at applied electric field 5, 6, and 7 V/μm, respectively. The distance of spacer was 100 μm and these samples were square cells with length of 1 cm.

(a)

(b)

(c)   (d)
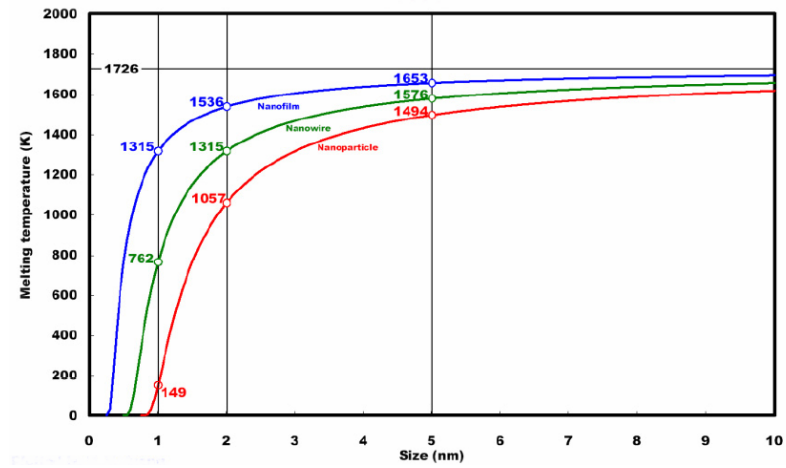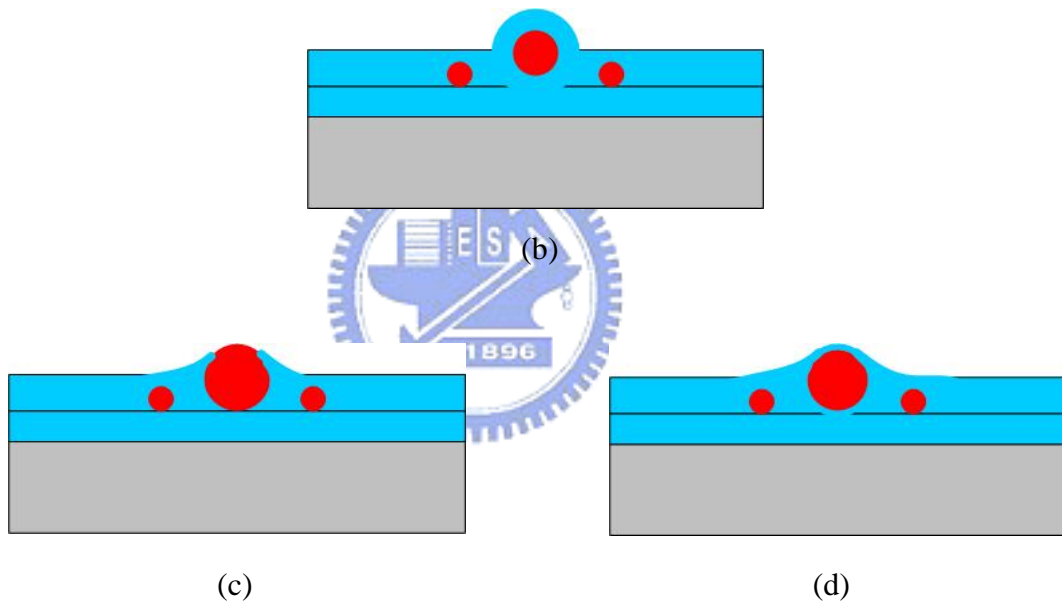
Figure 2-23 (a) Lindemann Criterion

The primitive situation after deposition (b) and two synthetical mechanisms of CNTs growth (c) Fe catalytic nanoparticles might be revealed out (d) Fe catalytic nanoparticles might not be revealed out but the carbon radicals still could diffuse through the thin Ti film.
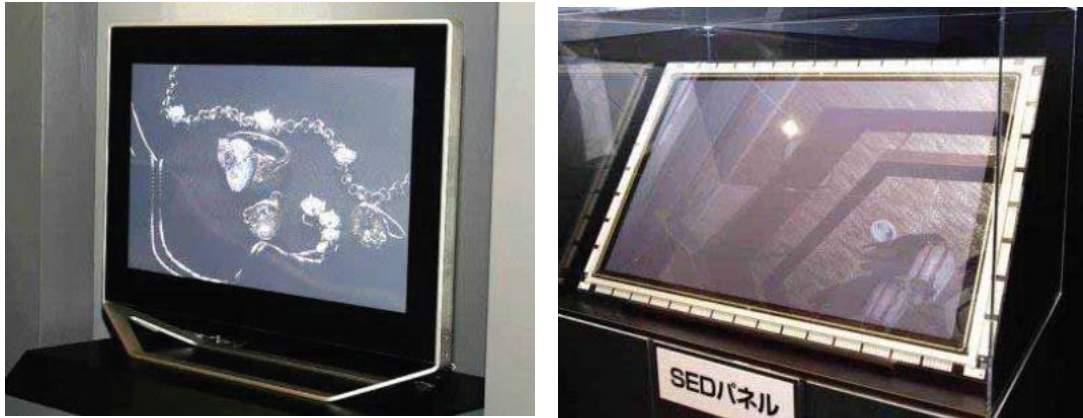
(a)   (b)
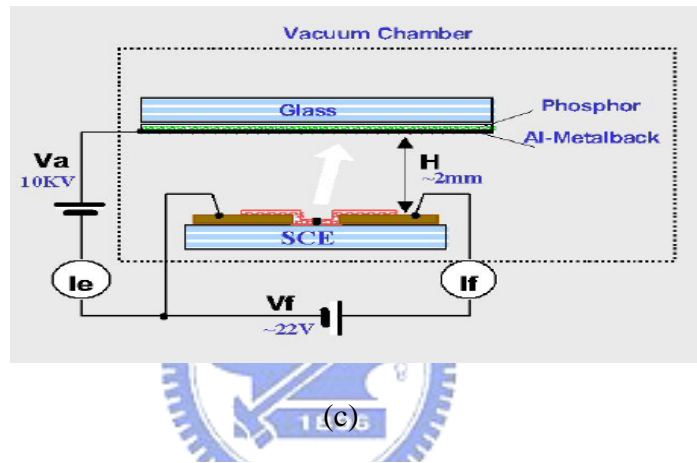
(c)
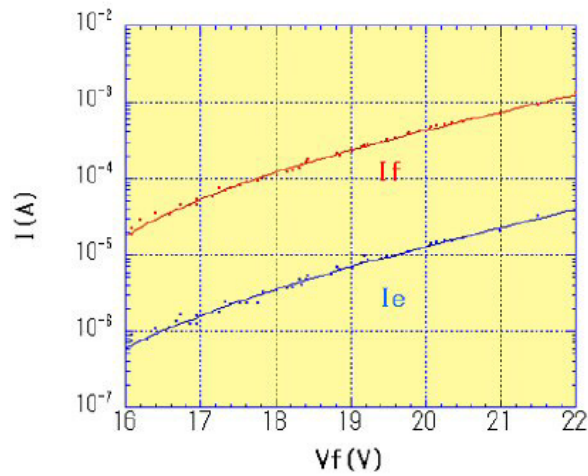
(d)

Figure 3-1 (a) (b) The SED jointly developed by Canon and Toshiba Corporation and (c) (d)

showed the field emission efficiency.
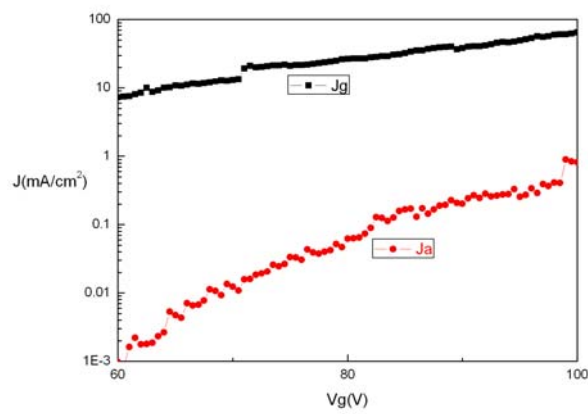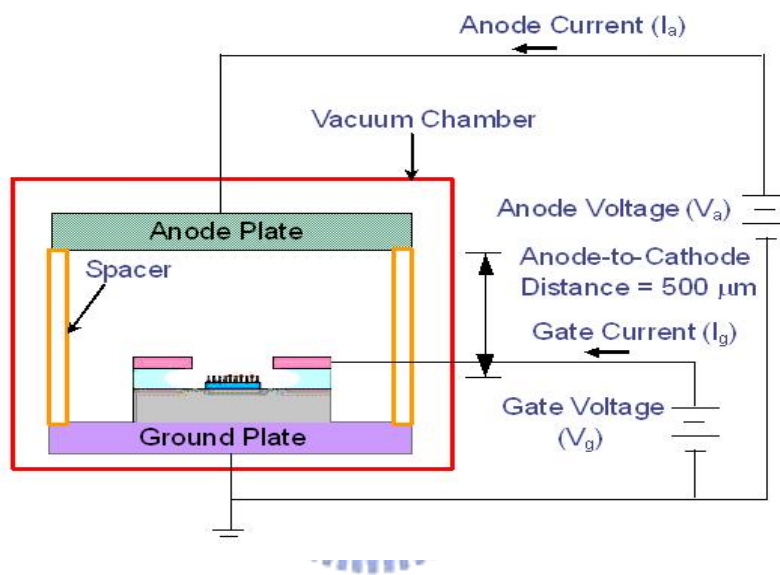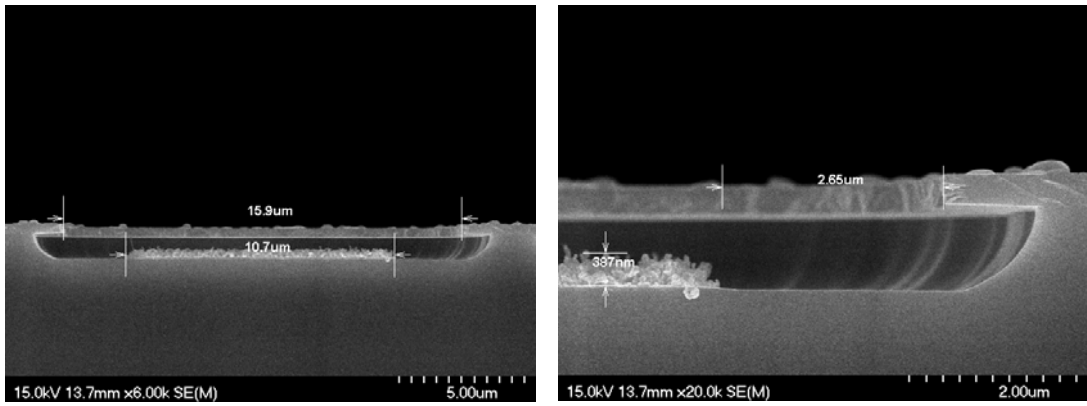
Figure 3-2 The traditional triode structure (oxide-poly) and the field emission efficiency.
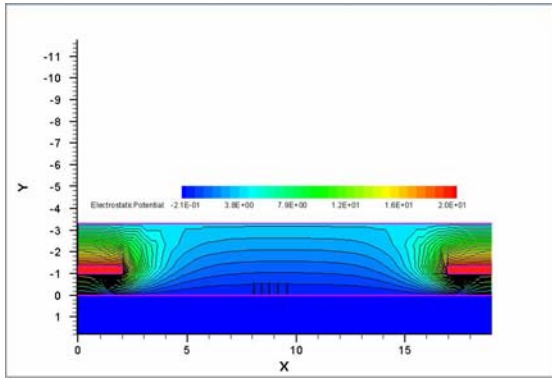
(a)
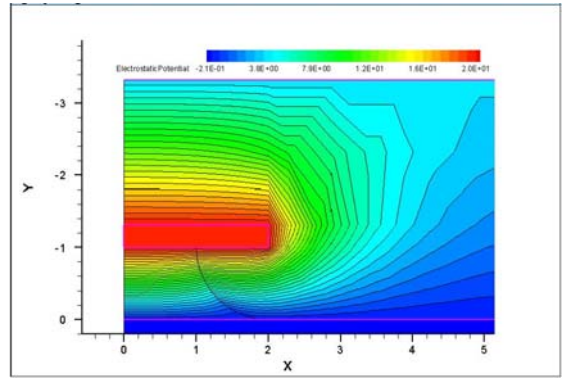
(b)
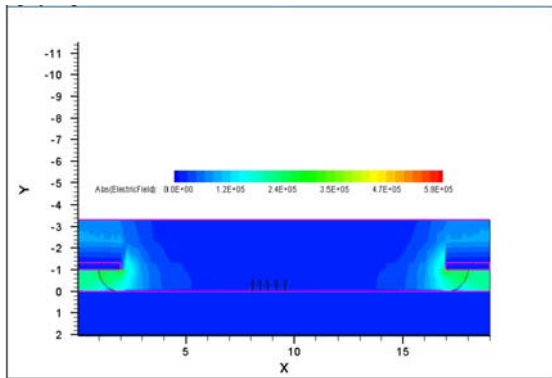
(c)
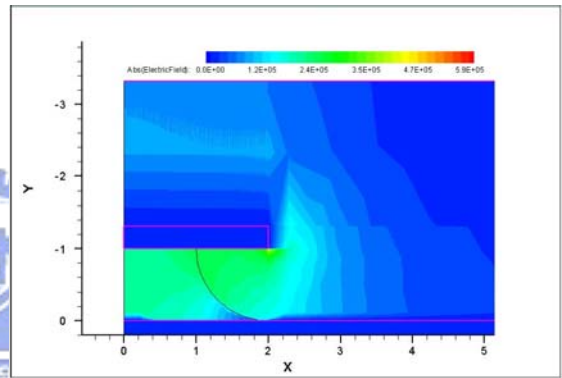
(d)

Figure 3-3 The simulations of (a) (b) Electrostatic potential and (c) (d) Electric field with oxide-poly structure.
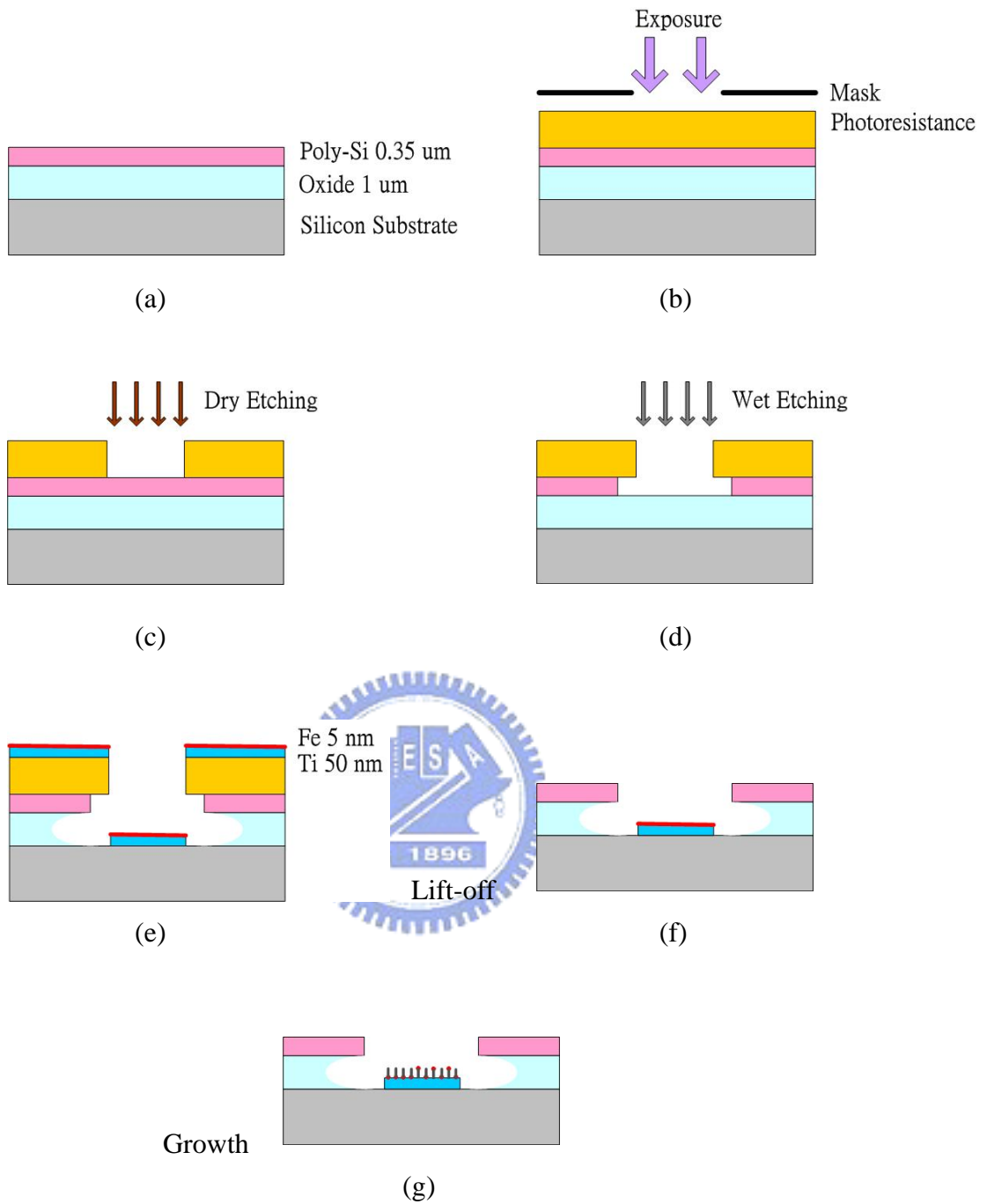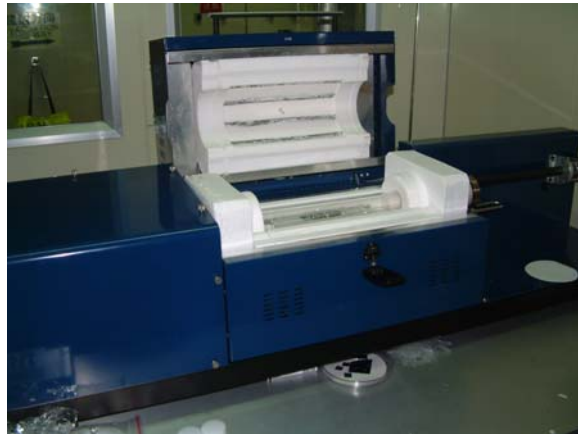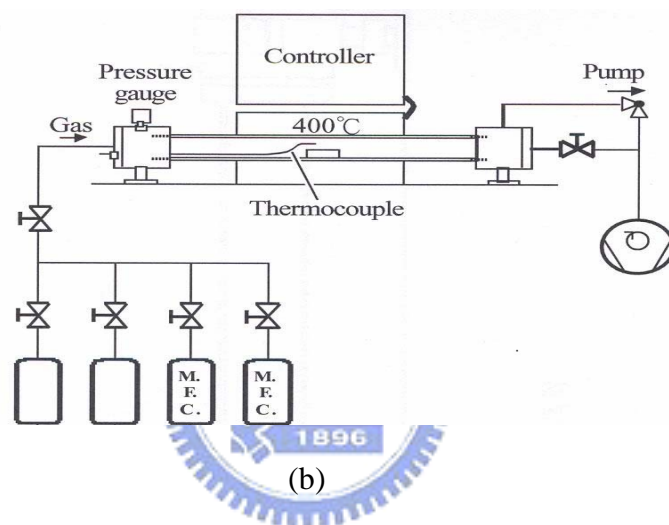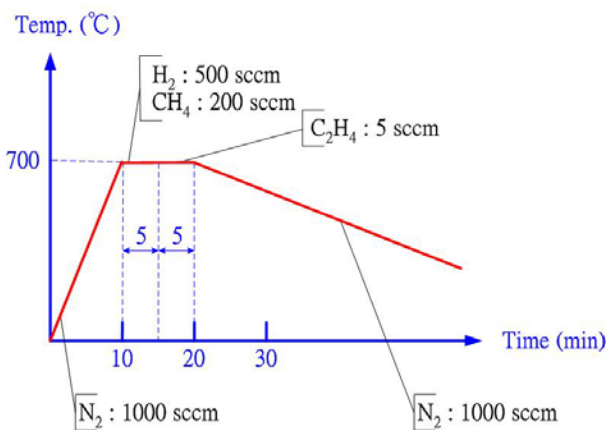
(a)

(b)

(c)

(d)

(e)

(f)

Growth

(g)

Figure 3-4 Experimental procedures of triode structure with oxide-poly composition.

(a)

(b)

(c)

Figure 3-5 (a) (b) Show photo and schematic pictures of thermal CVD, and (c) the growth condition of CNTs in the thermal CVD.

(a)　　　　　　　　　　　　　(b)
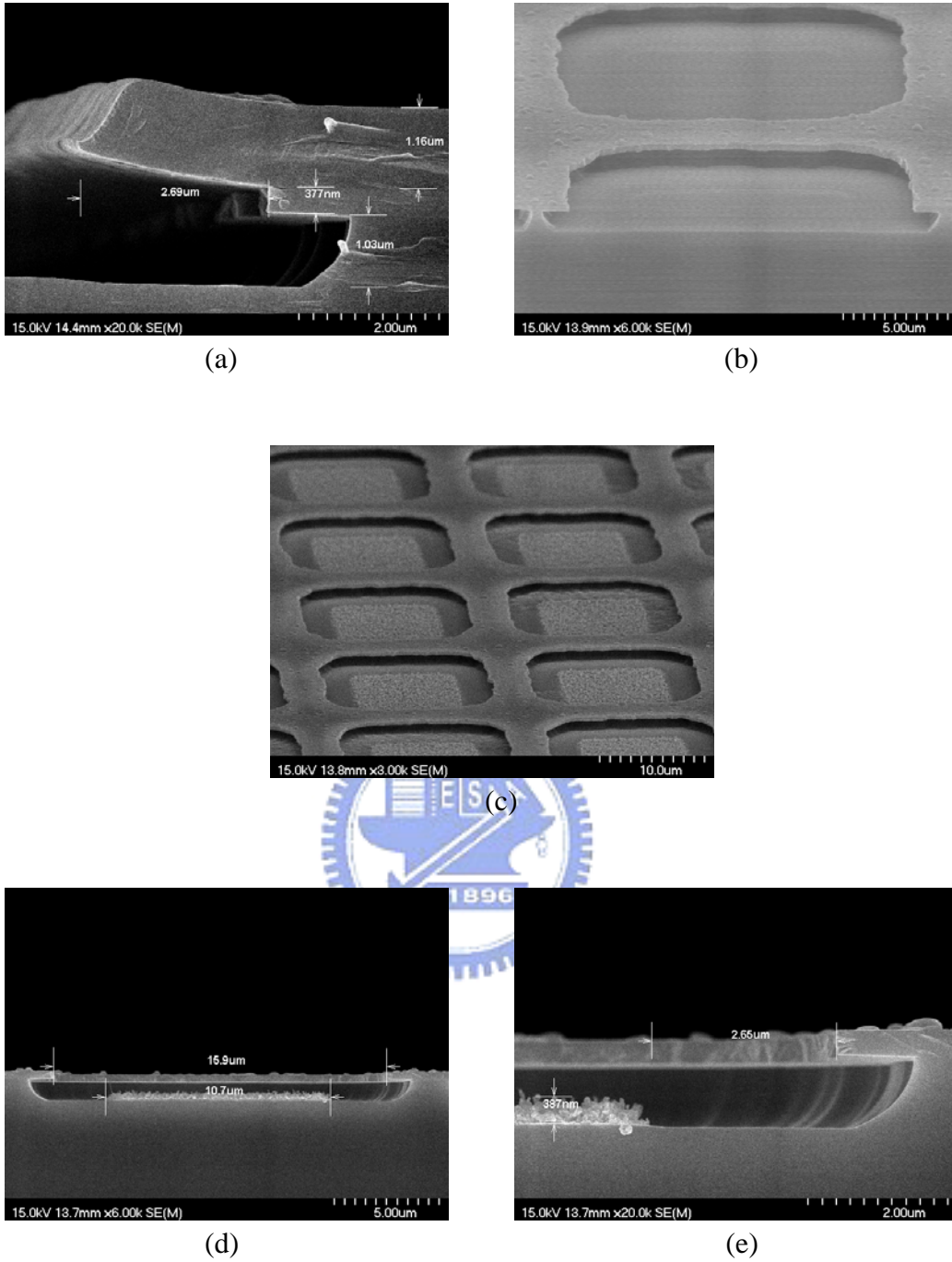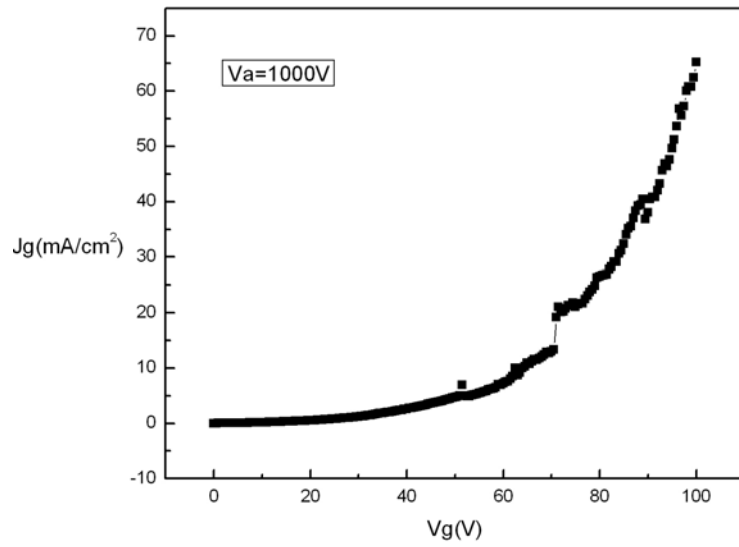
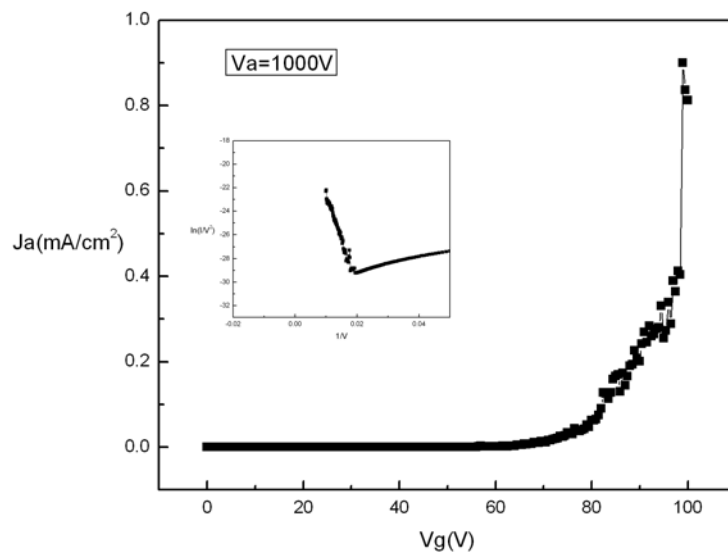

(c)

(d)　　　　　　　　　　　　　(e)

Figure 3-6 Fe/Ti (5 nm/50 nm) patterns were formed (a) before lift-off and (b) after lift-off. (c)
(d) (e) Showed the structure of oxide-poly composition and the morphology of
CNTs.

(a)

(b)

Figure 3-7 The field emission properties: (a) the relationship between emission gate current density and gate voltage (b) the relationship between emission anode current density and gate voltage and the inset showed the Fowler-Nordheim plot
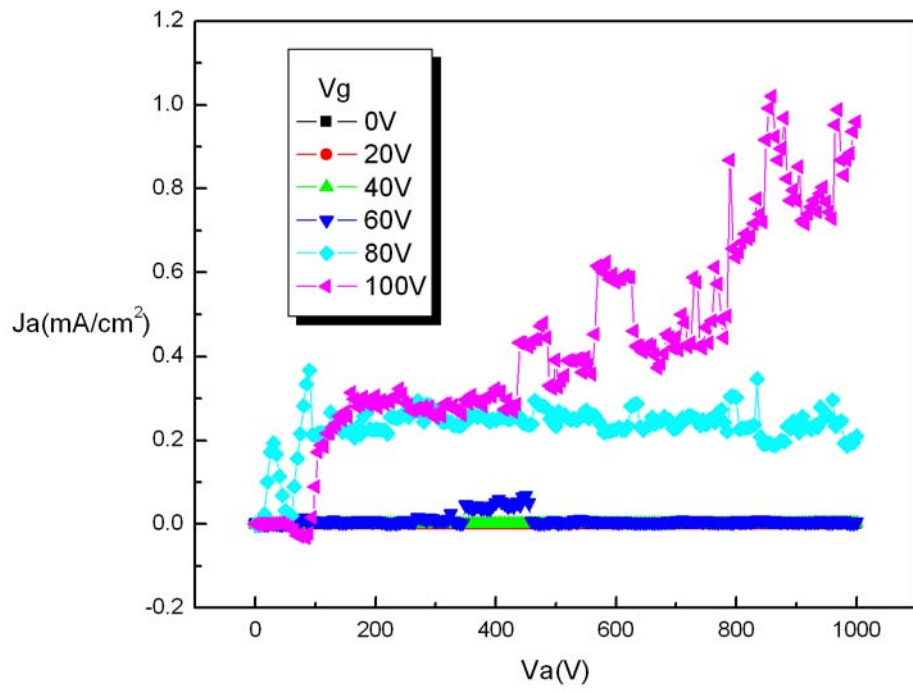
Figure 3-8 The emission anode current density versus anode voltage with different gate bias.
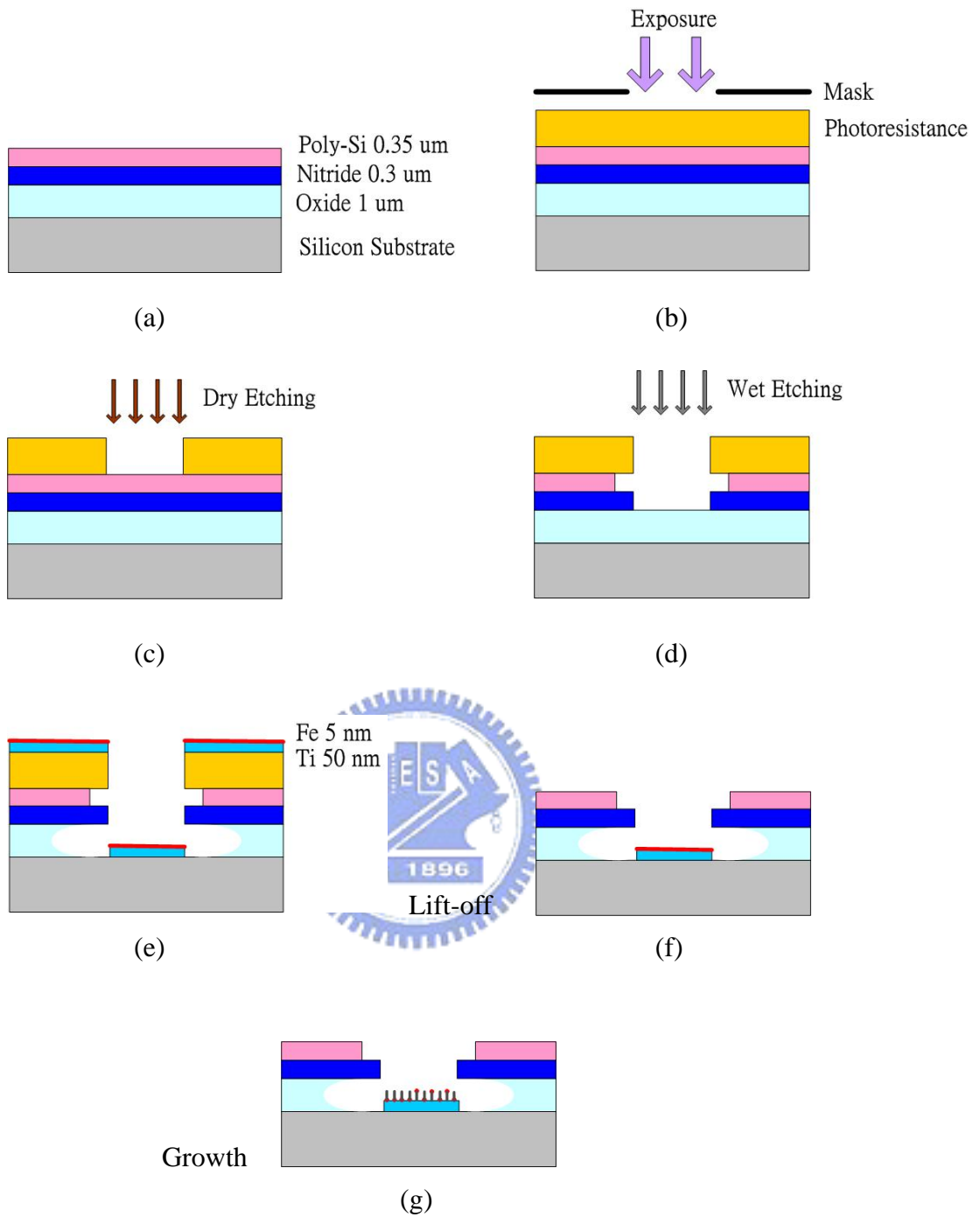
Figure 3-9 Experimental procedures of triode structure with oxide-nitride-poly composition.
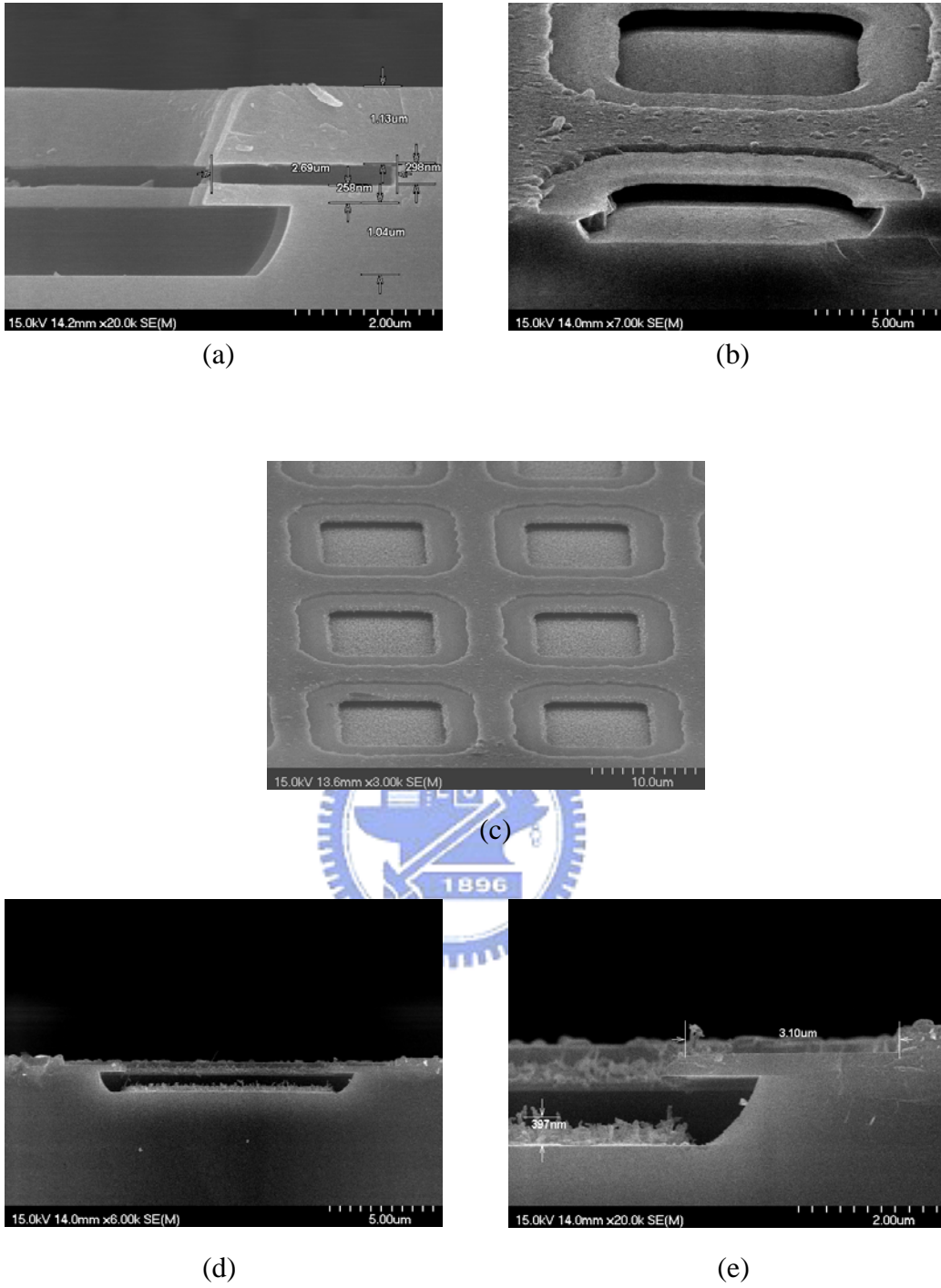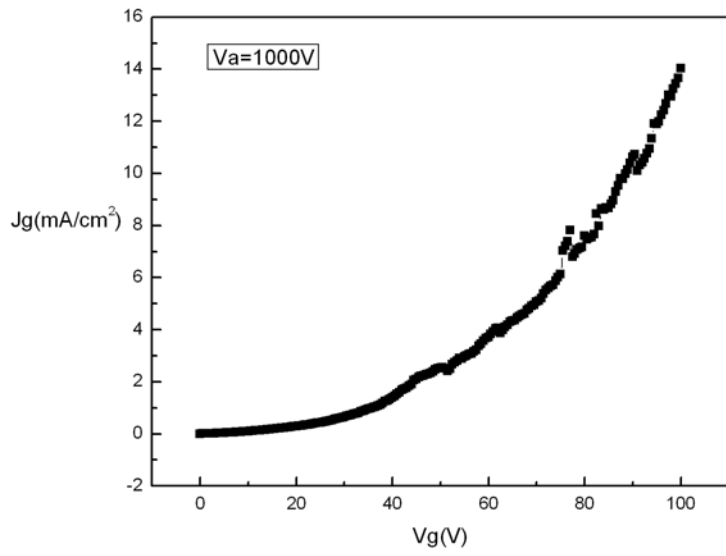
(a)

(b)

(c)

(d)

(e)

Figure 3-10 Fe/Ti (5 nm/50 nm) patterns were formed (a) before lift-off and (b) after lift-off.

(c) (d) (e) Showed the structure of oxide-nitride-poly composition and the

morphology of CNTs.

(a)

(b)

Figure 3-11 The field emission properties: (a) the relationship between emission gate current density and gate voltage (b) the relationship between emission anode current density and gate voltage and the inset showed the Fowler-Nordheim plot

Figure 3-12 The emission anode current density versus anode voltage with different gate bias.

(a)

(b)

Figure 3-13 The simulations of electrostatic potential with oxide-nitride-poly structure.

(a)　　　　　　　　　　　　　　　　　　(b)

(c)　　　　　　　　　　　　　　　　　　(d)

(e)　　　　　　　　　　　　　　　　　　(f)

(g)

Figure 3-14 Experimental procedures of triode structure with oxide-poly-nitride composition.
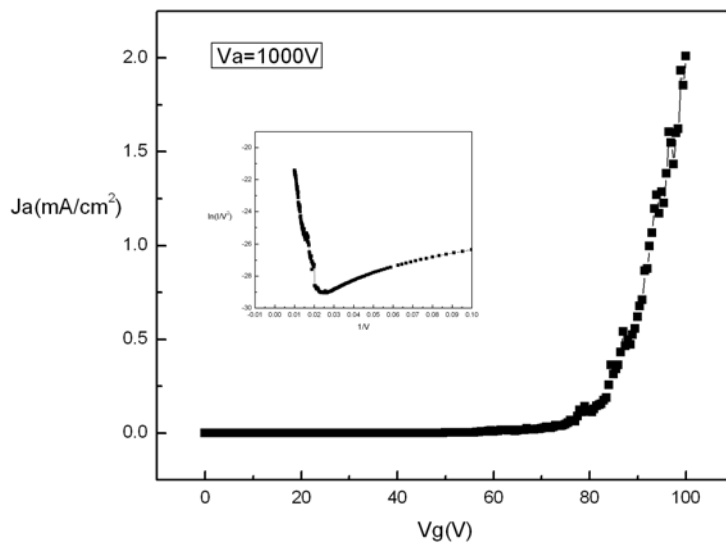
(a)

(b)

(c)
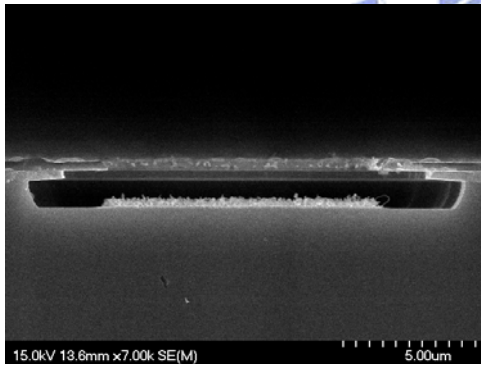
(d)
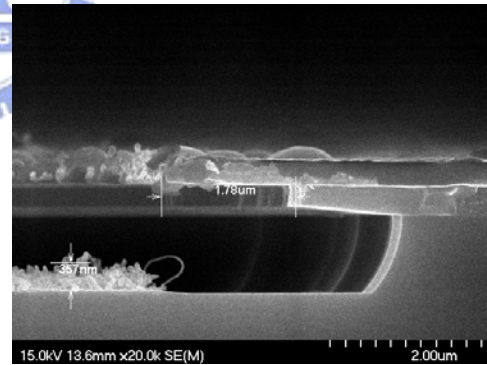
(e)

Figure 3-15 Fe/Ti (5 nm/50 nm) patterns were formed (a) before lift-off and (b) after lift-off. (c) (d) (e) Showed the structure of oxide-poly-nitride composition and the morphology of CNTs.
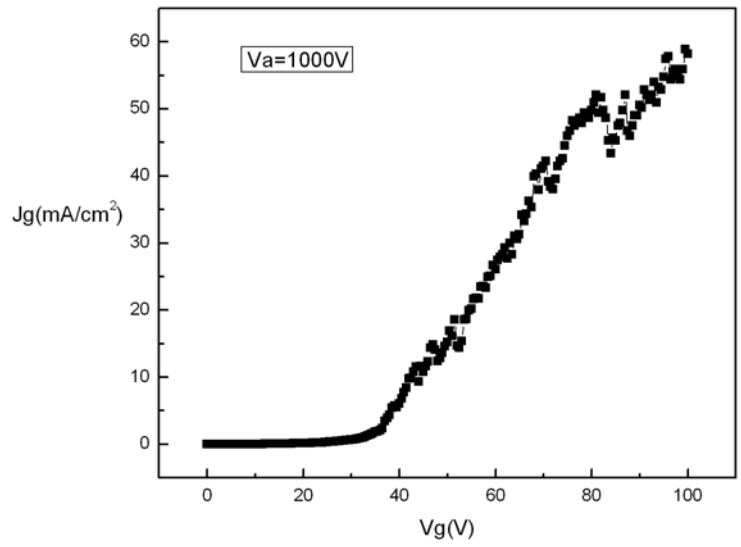
(a)
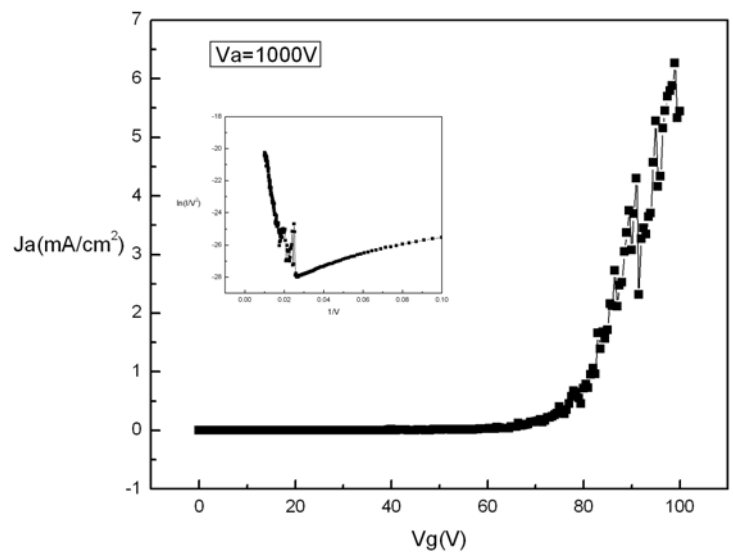
(b)

Figure 3-16 The field emission properties: (a) the relationship between emission gate current density and gate voltage (b) the relationship between emission anode current density and gate voltage and the inset showed the Fowler-Nordheim plot
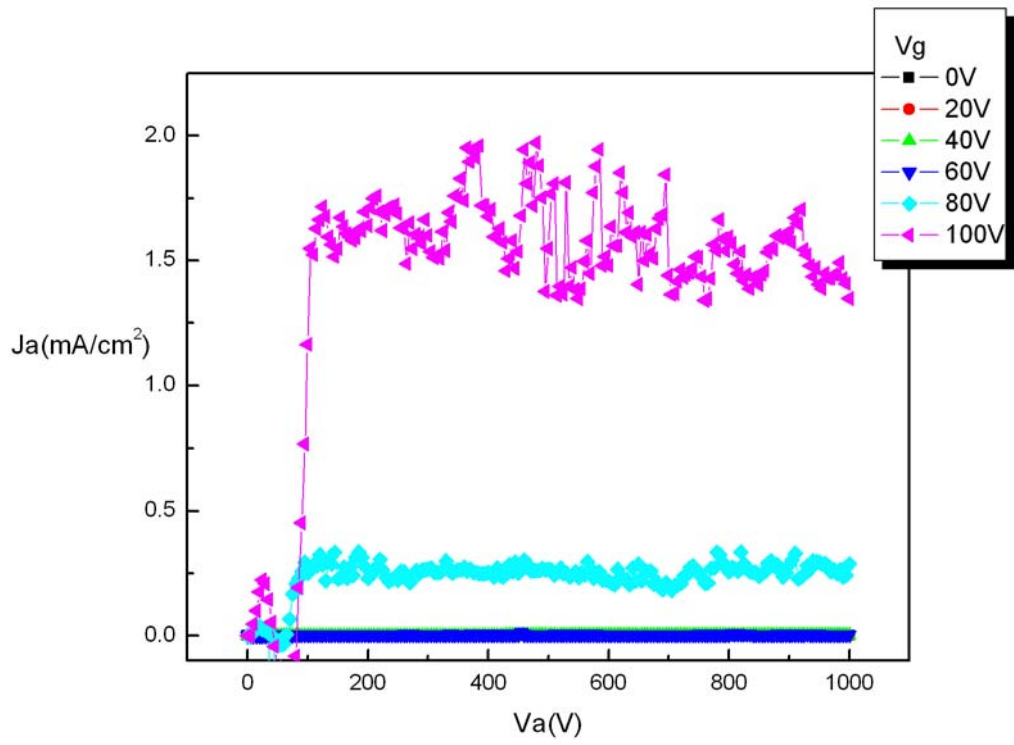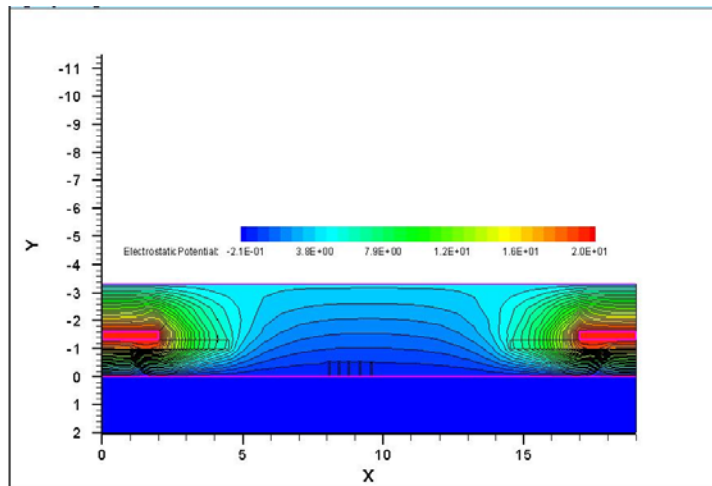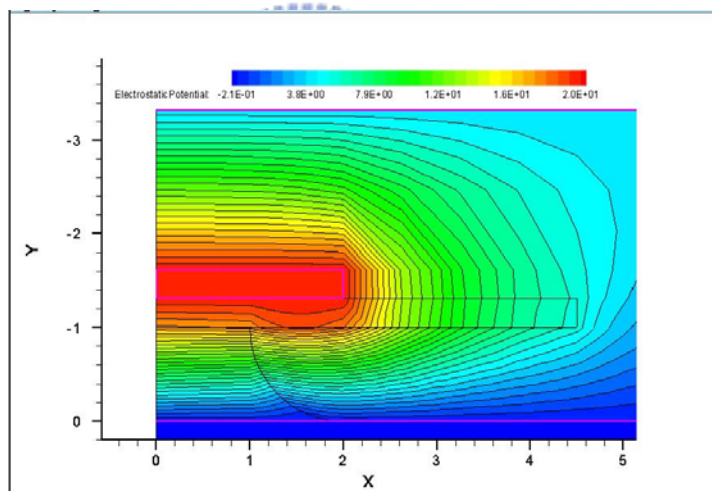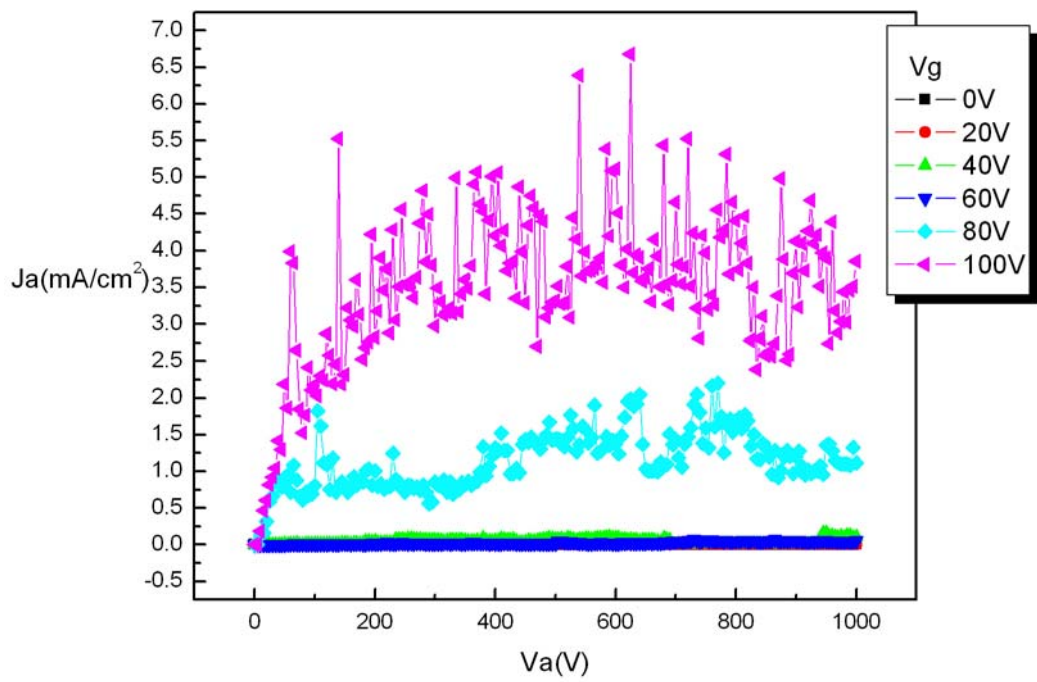
Figure 3-17 The emission anode current density versus anode voltage with different gate bias.
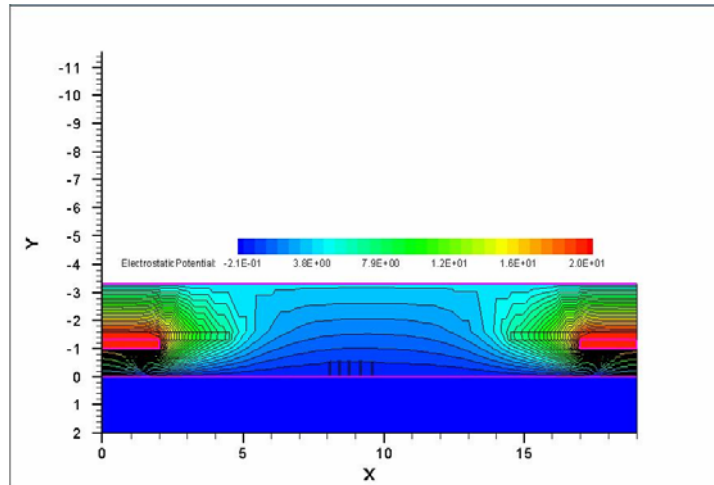
(a)
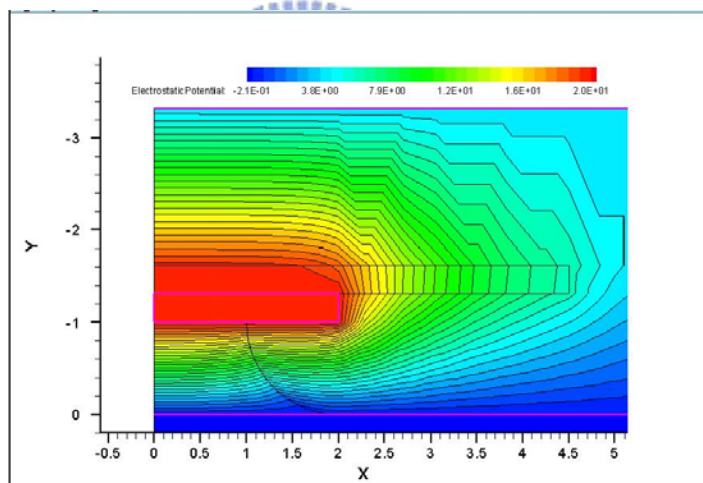
(b)

Figure 3-18 The simulations of electrostatic potential with oxide-poly-nitride structure.
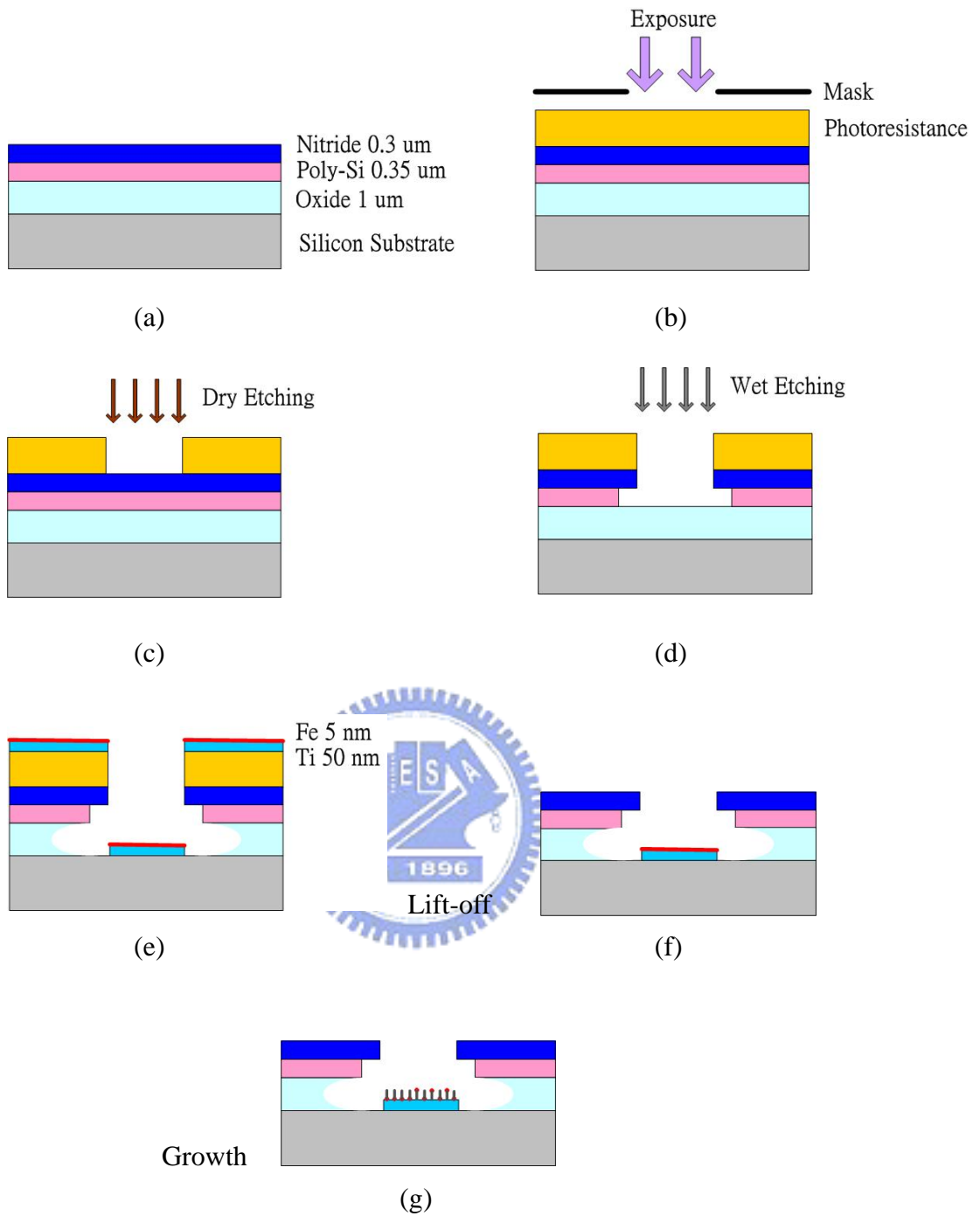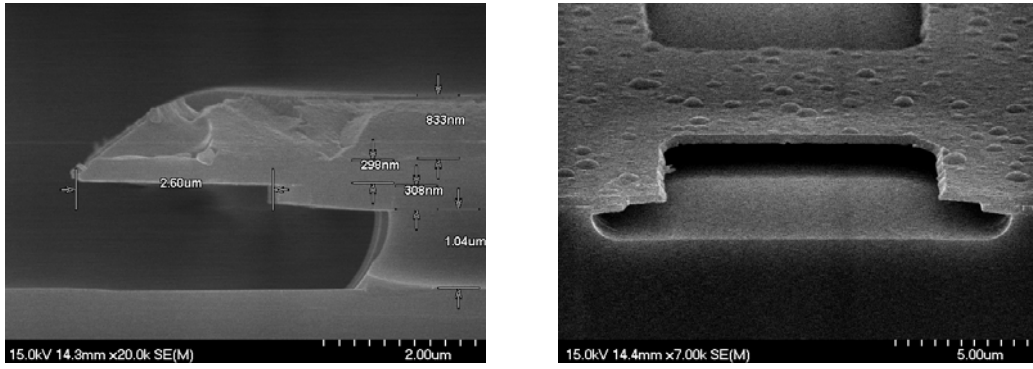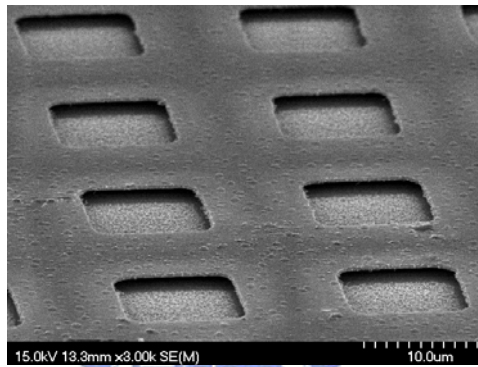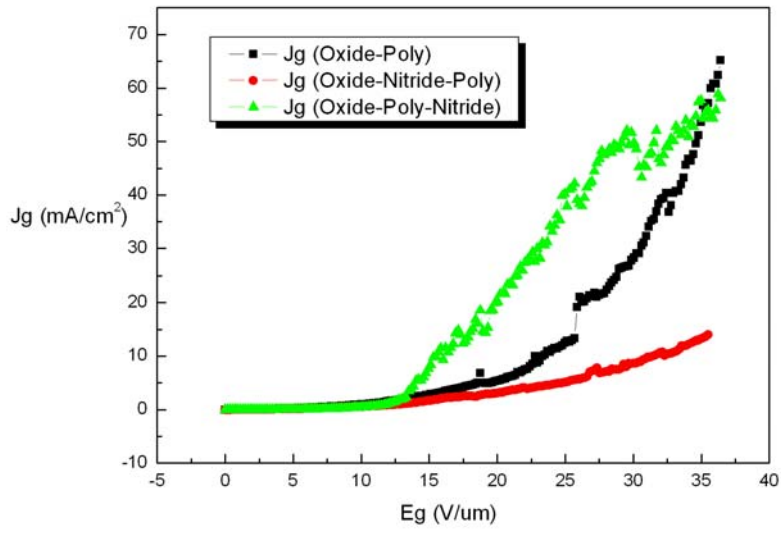
(a)
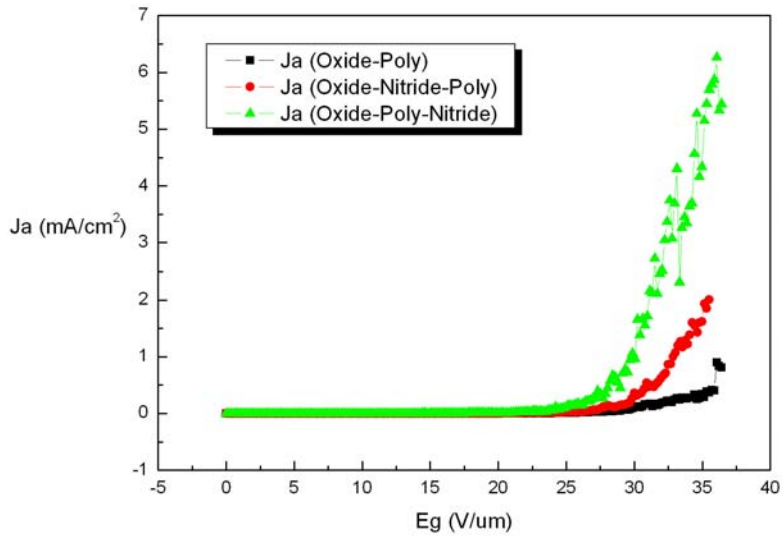
(b)

Figure 3-19 The field emission properties: (a) the relationship between emission gate current

density and gate electric field (b) the relationship between emission anode current

density and gate electric field

References

Chapter 1

[1.1] S. M. Sze, "Physics of semiconductor devices", 2nd ed., John-Wiley & Sons pulisher, New York, p. 648, 1981.

[1.2] C. A. Spindt, I. Brodie, L. Humpnrey, and E. R. Westerberg, "Electrical properties of thin-film field emission cathodes with molybdenum cones," J. Appl. Phys., Vol. 47, p. 5248, 1976.

[1.3] R. H. Fowler and L. W. Nordheim, "Electron emission in intense field," Proc. R. SOC. A229, p. 173, 1928.

[1.4] R. Meyer, "Recent development on microtips display at LETI," IVMC'91 Technical Digest, p. 6, 1991.

[1.5] N. E. McGruer and K. Warner, "Oxidation-sharpened gated field emitter array process," IEEE Trans. Electron Devices, Vol. 38, No. 10, p. 488, 1991.

[1.6] S. E. Huq and L. Chen, "Fabrication of sub-10 nm silicon tips: a new approach," J. Vac. Sci. & Technol. B, Vol. 13, No. 6, p. 2718, 1995.

[1.7] D. W. Branston and D. Stephani, "Field emission from metal-coated Silicon tips," IEEE Trans. Electron Devices, Vol. 38, No. 10, p. 2329, 1991.

[1.8] V. V. Zhirnov and E. I. Givargizov, "Field emission from silicon spikes with diamond coating," J. Vac. Sci. & Technol. B, Vol. 13, No. 2, p. 418, 1995.

[1.9] J. H. Jung and B. K. Ju, "Enhancement of electron emission efficiency and stability of molybdenum field emitter array by diamond-like carbon coating," IEEE IEDM'96, p. 293, 1996.

[1.10] P. Vaudaine and R. Meyer, "Microtips fluorescent display," IEEE IEDM'91, p. 197, 1991.

[1.11] C. Curtin, "The field emission display," International Display Research Conference p.

12, 1991.

[1.12]   C. A. Spindt, C. E. Holland, I. Brodie, J. B. Mooney, and E. R. Westerberg, "Field-emitter array applied to vacuum fluorescent displays," IEEE Trans. Electron Devices, Vol. 36, No. 1, p. 225, 1989.

[1.13]   David A. Cathey, "Field emission displays," Information Display, p. 16, Oct., 1995.

[1.14]   "Pixtech to produce color FEDs from November," News reported in Nikkei Electronics ASIA, p. 42, Nov., 1995.

[1.15]   R. E. Burgess, H. Kroemer, and J. M. Honston, "Corrected value of Fowler-Norheim field emission function v(y) and s(y)," Phys. Rev., Vol. 1, No. 4, p. 515, 1953.

[1.16]   R. B. Marcus, T. S. Ravi, T. Gmitter, H. H. Busta, J. T. Niccum, K. K. Chin, and D. Liu, "Atomically sharp silicon and metal field emitters," IEEE Trans. Electron Devices, Vol. 38, p. 2289, 1991.

[1.17]   C. A. Spindt, "A thin film emission cathode," Communications, p. 3504, 1968.

[1.18]   S. Itoh, T. Watanabe, T. Yamaura, and K. Yano, "A challenge to field emission displays," in Proc. Asia Display, p. 617, Oct. 1995.

[1.19]   R. Meyer, A. Ghis, P. Rambaud, and F. Muller, "Microtips fluores-cent display," in Proc. Japan Display, p. 512, Sept./Oct. 1986.

[1.20]   S. Itoh AND M. Tanaka, "Current Status of Field-Emission Displays", Proceedings of the IEEE, VOL. 90, NO. 4, APRIL 2002.

[1.21]   M. Ding, H. Kim, and A. I. Akinwande "Highly Uniform and Low Turn-On Voltage Si Field Emitter Arrays Fabricated Using Chemical Mechanical Polishing", IEEE Electron Device Letters, Vol. 21, No. 2, Feb. 2000.

[1.22]   J Itoh, Y Tohma, K Morigawa, S. Kanemaru and K. Shimizu "Fabrication of double gate Si field emitter arrays for focused electron beam generation" J. Vac. Sci. & Technol. B., Vol. 13(5), p. 1968, 1995.

[1.23]   K. Yamamoto, I. Nomura, K. Yamazaki, S. Uzawa and K. Hatanaka, "Fabrication and

characterization of surface conduction electron emitters," SID Digest, p. 1933, 2005.

[1.24] T. Oguchi, E. Yamaguchi, K. Sasaki, K. Suzuki, S. Uzawa and K. Hatanake, "A 36-inch surface conduction electron emitter display (SED) ," SID Digest, p. 1929, 2005.

[1.25] S. Iijima, "Helical microtubules of graphitic carbon," Nature, Vol. 354, p. 56, 1991.

[1.26] M. S. Dresselhaus, G. Dresselhaus, K. Sugihara, L. I. Spain, and H. A. Goldberg, "Graphite fibers and filaments," Springer-Verlag, New York, 1998.

[1.27] P. M. Ajayan, "Nanotubes from carbon," Chem. Rev., Vol. 99, p. 1787, 1999.

[1.28] S. Iijima and T. Ichihashi, "Single-shell carbon nanotubes of 1-nm diameter," Nature, Vol. 363, p. 603, 1993.

[1.29] D. S. Bethune, C. H. Kiang, M. S. de Vries, G. Gorman, R. Savoy, J. Vazquez, and R. Beyers, "Cobalt-catalyzed growth of carbon nanotubes with single-atomic-layer walls," Nature, Vol. 363, p. 605, 1993.

[1.30] M. S. Dresselhaus, G. Dresselhaus, and P. C. Eklund, "Science of fullerenses and carbon nanotubes," Academic Press, New York, 1996.

[1.31] R. Saito, M. S. Dresselhaus, and G. Dresselhaus, "Physical properties of carbon nanotubes," World Scientific, New York, 1998.

[1.32] C. H. Olk and J. P. Heremans, "Scanning tunneling spectroscopy of carbon nanotubes," J. Mater. Res., Vol. 9, p. 259, 1994

[1.33] D. L. Carroll, P. Redlich, P. M. Ajayan, J. C. Charlier, X. Blasé, A. De Vita, and R. Car, "Electronic structure and localized states at carbon nanotube tips," Phys. Rev. Lett., Vol. 78, p. 2811, 1997.

[1.34] D. L. Carroll, X. Blasé, J. C. Charlier, S. Curran, P. Redlich, P. M. Ajayan, S. Roth, and M. Ruhle, "Effects of nanodomain formation on the electronic structure of doped carbon nanotubes," Phys. Rev. Lett., Vol. 81, p. 2332, 1998.

[1.35] Y. K. Kwon, T. H. Lee, S. G. Kim, P. Jund, D. Tomanek, and R. E. Smalley. Phys Rev.

Lett., 79, p. 2065, 1997.

[1.36]   Y. Saito, Asia Display/IDW'01, "Carbon Nanotubes: Preparation and Physical Properties," p. 11, 2001.

[1.37]   X. Xu and G. R. Brandes, "A method for fabricating large-area, patterned, carbon nanotube field emitters," Appl. Phys. Lett., Vol. 74, p. 2549, 1999.

[1.38]   A. M. Rao, D. Jacques, and R. C. Haddon, "In situ-grown carbon nanotube arrays with excellent field emission characteristics," Appl. Phys. Lett., Vol. 76, p. 3813, 2000.

[1.39]   H. Murakami, M. Hirakawa, C. Tanaka, and H. Yamakawa, "Field emission from well-aligned, patterned, carbon nanotube emitters," Appl. Phys. Lett., Vol. 76, p. 1176, 2000.

[1.40]   W. B. Choi, D. S. Chung, J. H. Kang, H. Y. Kim, Y. W. Jin, I. T. Han, Y. H. Lee, J. E. Jung, N. S. Lee, G. S. Park, and J. M. Kim, "Fully sealed, high-brightness carbon-nanotube field-emission display," Appl. Phys. Lett., Vol. 75, p. 3129, 1999.
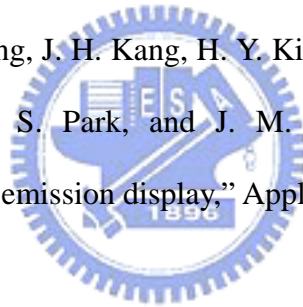
Chapter 2

[2.1] W. Lei, B. P. Wang, H. C. Yin, Y. X. Wu, and C. Z. Chang, "Influence of the fringe field and the field interaction on the emission performance of a diode emitter array," Nuclear Ins. and Methods in Phys. Research A., 451, p. 389, 2000.

[2.2] N. V. Egorov, and A. A. Almazov, "Optimization of multi-tip field emission electron source," Vacuum 52, p. 295, 1999.

[2.3] O. Groning, O. M. Kuttel, C. Emmenegger, P. Groning, and L. Schlapbach, "Field emission properties of carbon nanotubes," J. Vac. Sci. & Technol. B., Vol. 18(2), p. 665, 2000.

[2.4] S. Iijima, "Helical microtubules of graphitic carbon," Nature, Vol. 354, p. 56, 1991.

[2.5] Y. K. Kwon, T. H. Lee, S. G. Kim, P. Jund, D. Tomanek, and R. E. Smalley. Phys Rev. Lett., 79, p. 2065, 1997.

[2.6] Y. Saito, Asia Display/IDW'01, "Carbon Nanotubes: Preparation and Physical Properties," p. 11, 2001.

[2.7] J. M. Lauerhaas, J. Y. Dai, A. A. Setlur, and R. P. H. Chang, "The effect of arc parameters on the growth of carbon nanotubes," J. Mater. Res., Vol. 12, p. 1536, 1997.

[2.8] P. M. Ajayan, Ph. Redlich, and M. Ruhle, "Balance of graphite deposition and multi-shell carbon nanotube growth in the carbon arc-discharge," J. Mater. Res., Vol. 12, p. 244, 1997.

[2.9] A. G. Rinzler , J. Liu , H. Dai , P. Nikolaev , C. B. Huffman , F. J. Rodriguez-Macias , P. J. Boul , A. H. Lu , D. T. Colbert , R. S. Lee , J. E. Fischer , A. M. Rao , P. C. Eklund , and R. E. Smalley, "Large-scale purification of single-wall carbon nanotubes: process, product, and characterization," Appl. Phys. A, Vol. 67, p. 29, 1998.

[2.10] J. Li, W. Lei, X. Zhang, X. Zhou, Q. Wang, Y. Zhang, and B. Wang, "Field emission

characteristic of screen-printed carbon nanotube cathode," Appl. Surf. Sci., 220, p. 96, 2003.

[2.11]   Y. Li, C. Zhu, and X. Liu, "Field emission display with carbon nanotubes cathode: prepared by a screen-printing process," Diamond Relat. Mater., 11, p. 1845, 2002.

[2.12]   Y. S. Shi, C. C. Zhu, Q. Wang, and X. Li, "Large area screen-printing cathode of CNT for FED," Diamond Relat. Mater., 12, p. 1449, 2003.

[2.13]   Y. J. Park, I. T. Han, H. J. Kim, N. S. Lee, Y. W. Jin, J. W. Kim, J. E. Jung, C. Y. Park, and J. M. Kim, Jpn. J. Appl. Phys., 42, p. 1414, 2003.

[2.14]   Y. S. Woo, I. T. Han, Y. J. Park, H. J. Kim, J. E. Jung, N. S. Lee, D. Y. Jeon, and J. M. Kim, Jpn. J. Appl. Phys., 42, p. 1410, 2003.

[2.15]   Y. C. Choi, D. J. Bae, Y. H. Lee, B. S. Lee, G. S. Park, W. B. Choi, N. S. Lee, and J. M. Kim, "Growth of carbon nanotubes by microwave plasma-enhanced chemical vapor deposition at low temperature," J. Vac. Sci. & Technol. A, Vol. 18, No. 4, p. 1864, 2000.

[2.16]   J. M. Mao, L. F. Sun, L. X. Qian, Z. W. Pan, B. H. Chang, W. Y. Zhou, G. Wang, and S. S. Xie, "Growth of carbon nanotubes on cobalt disilicide precipitates by chemical vapor deposition," Appl. Phys. Lett., Vol. 72, p. 3297, 1998.

[2.17]   C. J. Lee, K. H. Son, J. Park, J. E. Yoo, Y. Huh, and J. Y. Lee, "Low temperature growth of vertically aligned carbon nanotubes by thermal chemical deposition," Chem. Phys. Lett., Vol. 338, p. 113, 2001.

[2.18]   J. H. Choi, T. Y. Lee, S. H. Choi, J. H. Han, J. B. Yoo, C. Y. Park, T. Jung, S. G. Yu, W. Yi, I. T. Han, and J. M. Kim, "Control the carbon nanotubes density through Ni nanoparticle formation using thermal and NH_3 plasma treatment," Diamond Relat. Mater., 12, p. 794, 2003.

[2.19]   J. H. Choi, T. Y. Lee, S. H. Choi, J. H. Han, J. B. Yoo, C. Y. Park, T. Jung, S. G. Yu, W. Yi, I. T. Han, and J. M. Kim, "Density control of carbon nanotubes using NH_3 plasma

treatment of Ni catalyst layer," Thin Solid Films, 435, p. 318, 2003.

[2.20]   J. H. Choi, S. H. Choi, J. H. Han, J. B. Yoo, and C. Y. Park, "Enhanced electron emission from carbon nanotubes through density control using in situ plasma treatment of catalyst metal," J. Appl. Phys., 94, p. 487, 2003.

[2.21]   C. P. Juan, C. C. Tsai, K. H. Chen, L. C. Chen, and H. C. Cheng, Jpn. J. Appl. Phys., 44, p. 8231, 2005.

[2.22]   T. G. D. Monsabert, J. Dijon, and P. Gadelle, "Density control of carbon nanotubes and filaments films by wet etching of catalyst particles and effects on field emission properties," Carbon, 43, p. 2441, 2005.

[2.23]   L. Nilsson, O. Groening, C. Emmenegger, O. Kuettel, E. Schaller, L. Schlapbach, H. Kind, J-M, Bonard, and K. Kern, "Scanning field emission from patterned carbon nanotube films," Appl. Phys. Lett., Vol. 76, No. 15, p. 2071, 2000.

[2.24]   J. Li, W. Lei, X. Zhang, X. Zhou, Q. Wang, Y. Zhang, and B. Wang, "Field emission characteristic of screen-printed carbon nanotube cathode," Appl. Surf. Sci. 220, p. 96, 2003.

[2.25]   Z. F. Ren, Z. P. Huang, D. Z. Wang, J. G. Wen, J. W. Xu, J. H. Wang, L. E. Calvet, J. Chen, J. F. Klemic, and M. A. Reed, "Growth of a single freestanding multiwall carbon nanotube on each nanonickel dot," Appl. Phys. Lett., 75, p. 1086, 1999.

[2.26]   Lixin Dong, Subramanian, A. Nelson, B. J., and Yu Sun, Intelligent Robots and systems, p. 3598, 2005.

[2.27]   S. H. Jeong, O. J. Lee, S. H. Oh, and C. G. Park, "Packing Density Control of Aligned Carbon Nanotubes," Chem. Mater., Vol. 14, No. 10, p. 4003, 2002.

[2.28]   P. L. Chen, J. K. Chang, F. M. Pan, and C. T. Kuo, "Tube number density control of carbon nanotubes on anodic aluminum oxide template," Diamond Relat. Mater., 14, p. 804, 2005.

[2.29]   J. Yotani, S. Uemura, T. Nagasako, H. Kurachi, H. Yamada, T. Ezaki, T. Maesoba, T.

Nakao, M. Ito, T. Ishida, and Y. Saito, "Emission Enhancement by Excimer Laser Irradiation over a Weblike Carbon Nanotube Layer," Jpn. J. Appl. Phys., 43, No. 11B, p. L1459, 2004.

[2.30] R. L. Lai, Y. R. Chang, C. P. Juan, T. Y. Chuang, K. C. Lin, J. K. Shiu, H. C. Tai, K. H. Chen, L. C. Cheng, and H. C. Cheng, "Improvement of Breakdown Field of Carbon Nanotubes by a Ti-capping Layer on Catalyst Nanoparticles," SSDM, p. 11-6, 2005.

[2.31] C. C. Lin, P. Y. Lo, C. H. Lin, and C. T. Kuo, "Structure and property features of the catalyst-assisted carbon nanostructures on Si wafer by catalyst ion implantation and ECR-CVD," Diamond Relat. Mater., 14, p. 778, 2005.

Chapter 3

[3.1]   T. Oguchi, E. Yamaguchi, K. Sasaki, K. Suzuki, S. Uzawa, and K. Hatanaka, "A 36-inch Surface-conduction Electron-emitter Display (SED)," SID, p. 71-1, 2005.

[3.2]   K. Yamamoto, I. Nomura, K. Yamazaki, S. Uzawa, and K. Hatanaka, "Fabrication and Characterization of Surface Conduction Electron Emitters," SID, p. 71-2, 2005.

[3.3]   P. G. Collins and A. Zettl, "A simple and robust electron beam source from carbon nanotubes," Appl. Phys. Lett. Vol. 69, p. 1969, 1996.

[3.4]   Q. H. Wang, T. D. Corrigan, J. Y. Dai and R. P. H. Chang, "Field emission from nanotube bundle emitters at low fields," Appl. Phys. Lett. Vol. 70, p. 3308, 1997.

[3.5]   Z. F. Ren, Z. P. Huang, J. W. Xu, J. H. Wang, P. Bush, M. P. Siegal, and P. N. Provencio, "Synthesis of Large Arrays of Well-Aligned Carbon Nanotubes on Glass," Science vol. 282, p. 1105, 1998.

[3.6]   J. M. Bonard, J. P. Salvetat, T. Stockli, W. A. de Heer, L. Forro, and A. Chatelain, "Field emission from single-wall carbon nanotube films," Appl. Phys. Lett. Vol. 73, p. 918, 1998.

[3.7]   F. G. Tantair, L. C. Chen and S. L. Wei, W. K. Hong, K. H. Chen, H. C. Cheng "High current density field emission from arrays of carbon nanotubes and diamond-clad Si tips," J. Vac. Sci. Technol. B 18(3) p. 1207, 2000.

[3.8]   N. S. Lee, W. B. Choi, W. K. Yi, Y. W. Jin, Y. S. Choi, J. E. Jung, S. G. You, J. H. You, C. G. Lee, S. H. Cho, J. M. Ki "The carbon-nanotubes based field-emission displays for future large and full color displays," Microprocesses and Nanotechnology Conference, 2000 International, p. 124, 2000.

[3.9]   Q. H. Wang, M. Yan, and R. P. H. Chang "Flat panel display prototype using gated carbon nanotube field emitters," Appl. Phys. Lett. Vol. 78, p. 1294, 2001.

[3.10] S. C. Tseng, C. H. Li, Y. Y. Lin, C. H. Tsai, Z. P. Wang, K. C. Leou, C. H. Tsai, S. P. Chen, J. Y. Lee, and B. C. Yao, "Field emission characteristics of a single free

standing carbon nanotube with gate electrode," Diamond Relat. Mater., 14, p. 2064, 2005.

[3.11]   Y. M. Wong, W. P. Kang, J. L. Davidson, B. K. Choi, W. Hofmeister, and J. H. Huang, "Field emission triode amplifier utilizing aligned carbon nanotubes," Diamond Relat. Mater., 14, p. 2069, 2005.

[3.12]   H. J. Kim, J. H. Han, W. S. Yang, J. B. Yoo, C. Y. Park, I. T. Han, Y. J. Park, Y. W. Jin, J. E. Jung, N. S. Lee, and J. M. Kim, "Fabrication of field emission triode using carbon nanotubes," Mater. Sci. Engine. C, 16, p. 27, 2001.

[3.13]   J. W. Park, J. J. Kim, J. Kim, K. H. Yoo, "Effects of local gates on the electrical transport of single-walled carbon nanotubes," Physica E, 18, p. 216, 2003.

[3.14]   Y. S. Choi, J.H. Kang, Y. J. Park, W. B. Choi, C. J. Lee, S. H. Jo, C. G. Lee, J. H. You, J. E. Jung, N. S. Lee, and J. M. Kim, "An under-gate triode structure field emission display with carbon nanotube emitters," Diamond Relat. Mater., 10, p. 1705, 2001.

[3.15]   D. Y. Kim, J. B. Yoo, I. T. Han, H. J. Kim, H. J. Kim, J. E. Jung, Y. W. Jin, J. M. Kim, and K. H. Chin, "The density control of carbon nanotubes using spin-coated nanoparticle and its application to the electron emitter with triode structure," Diamond Relat. Mater., 14, p. 2084, 2005.

[3.16]   P. G. Jun, H. S. Uh, B. H. Kwak, H. W. Noh, S. S. Park, S. W. Ko, E. S. Cho, and J. D. Lee, "Numerical Analysis of Carbon Nanotube Field Emitter Arrays with Embedded Electron Beam Focusing Structure," IEEE, p. 88, 2004.

[3.17]   J. H. Choi, A. R. Zoulkarneev, Y. W. Jin, Y. J. Park, D. S. Chung, B. K. Song, I. T. Han, H. W. Lee, S. H. Park, H. S. Kang, H. J. Kim, J.W. Kim, J. E. Jung, J. M. Kim, H. G. Baek, and S. G. Yu, "Carbon nanotube field emitter arrays having an electron beam focusing structure," Appl. Phys. Lett., Vol. 84, No. 6, p. 1022, 2004.

[3.18]   J. H. Choi, A. R. Zoulkarneev, Y. J. Park, D. S. Chung, B. K. Song, H. S. Kang, C. W. Baik, I. T. Han, H. J. Kim, M. J. Shin, H. J. Kim, T. S. Oh, Y. W. Jin, J. M. Kim, and

N. Lee, "Optimization of Electron Beam Focusing for Gated Carbon Nanotube Field

Emitter Arrays," IEEE Trans. Electron Devices, Vol. 52, No. 12, p. 2584, 2005.

簡　歷

姓　名: 許鈞凱

性　別: 男

生　日: 民國七十一年一月三日

籍　貫: 彰化縣

地　址: 台北縣中和市國光街 36 巷 1 之 5 號 3 樓

學　歷: 台北縣立中和高級中學

（86 年 9 月～89 年 6 月）

國立成功大學電機工程學系

(89 年 9 月～93 年 6 月)

國立交通大學電子工程研究所碩士班

(93 年 9 月～95 年 8 月)

論文題目:具有適當密度與元件結構之奈米碳管之場發射特性最佳化

Optimization for the Field Emission Properties of Carbon Nanotubes
with Proper Densities and Device Structures